Technische Universität München
TUM School of Natural Sciences

Model- and halo-independent limits on the dark matter-nucleon interaction

Anja Sabine Brenner

Vollständiger Abdruck der von der TUM School of Natural Sciences der Technischen Universität München zur Erlangung des akademischen Grades einer

Doktorin der Naturwissenschaft

genehmigten Dissertation.

Vorsitz:		Prof. Dr. Elisa Resconi
Prüfer der Dissertation:	1.	Prof. Dr. Alejandro Ibarra
	2.	Priv.-Doz. Dr. Mathias Garny

Die Dissertation wurde am 06.12.2022 bei der Technischen Universität München eingereicht und durch die TUM School of Natural Sciences am 10.02.2023 angenommen.

ABSTRACT

Despite the continuous efforts to search for dark matter particles in various approaches, no significant signal of dark matter-nucleon interactions has been detected so far. When casting the null-search results into constraints on the dark matter properties, it is commonly assumed that dark matter couples to nucleons via the so-called spin-independent and spin-dependent interactions, with equal strength to protons and neutrons. However, these assumptions do not hold in many concrete models. In the non-relativistic effective field theory, dark matter in general interacts with the nucleon via 28 different couplings (for dark matter spin up to 1/2) and several of them may appear at the same time, interfering with one another. It is therefore not straightforward to compare published limits with model predictions. In this work, we present a methodology that allows to determine model-independent upper limits on the dark matter-nucleon coupling strengths, taking into account the interference among interactions. We apply the method to derive upper limits using data provided by XENON1T, PICO-60 and IceCube. For some interactions, the limit can be relaxed by 6 orders of magnitude. We further make use of the complementarity of the different detector compositions to constrain the parameter space of dark matter-nucleon interactions in a strong, but model-independent manner. Combining data from XENON1T, PICO-60 and IceCube, we obtain limits for some interactions that can be up to 4 orders of magnitude stronger than those from the single-experiments. Further, it is commonly assumed that the velocity distribution of dark matter particles in the Solar System follows a Maxwell-Boltzmann distribution. We also investigate the impact of distortions on the Maxwell-Boltzmann distribution on the constraints on the coupling strengths of the non-relativistic effective field theory.

ZUSAMMENFASSUNG

Trotz der kontinuierlichen Bemühungen, mit verschiedenen Ansätzen nach Dunkle-Materie-Teilchen zu suchen, konnte bisher kein signifikantes Signal für Wechselwirkungen zwischen Dunkler Materie und Nukleonen nachgewiesen werden. Wenn man die Ergebnisse der Nullsuche in Beschränkungen für die Eigenschaften der Dunklen Materie umwandelt, wird üblicherweise angenommen, dass Dunkle Materie über die so genannten spin-unabhängigen und spin-abhängigen Wechselwirkungen mit Protonen und Neutronen in gleicher Stärke an Nukleonen koppelt. In vielen konkreten Modellen sind diese Annahmen jedoch nicht zutreffend. In der nicht-relativistischen effektiven Feldtheorie wechselwirkt Dunkle Materie im Allgemeinen mit dem Nukleon über 28 verschiedene Kopplungen (für Dunkle-Materie-Spin bis 1/2), und mehrere davon können gleichzeitig auftreten und sich gegenseitig beeinflussen. Es ist daher nicht einfach, veröffentlichte Grenzwerte mit Modellvorhersagen zu vergleichen. In dieser Arbeit stellen wir eine Methode vor, die es ermöglicht, modellunabhängige Obergrenzen für die Kopplungsstärken zwischen Dunkler Materie und Nukleonen zu bestimmen, wobei die Interferenz zwischen den Wechselwirkungen berücksichtigt wird. Wir wenden die Methode an, um obere Grenzwerte aus den Daten von XENON1T, PICO-60 und IceCube abzuleiten. Für einige Wechselwirkungen kann der Grenzwert um 6 Größenordnungen gelockert werden. Darüber hinaus nutzen wir die Komplementarität der verschiedenen Detektorzusammensetzungen, um den Parameterraum der Wechselwirkungen zwischen Dunkler Materie und Nukleonen auf eine starke, aber modellunabhängige Weise einzuschränken. Durch die Kombination der Daten von XENON1T, PICO-60 und IceCube erhalten wir Grenzwerte für einige Wechselwirkungen, die bis zu 4 Größenordnungen stärker sein können als die der Einzelexperimente. Außerdem wird allgemein angenommen, dass die Geschwindigkeitsverteilung Dunkler-Materie-Teilchen im Sonnensystem einer Maxwell-Boltzmann-Verteilung folgt. Wir untersuchen auch die Auswirkungen von Abweichungen der Maxwell-Boltzmann-Verteilung auf die Grenzwerte der Kopplungsstärken der nicht-relativistischen effektiven Feldtheorie.

PUBLICATIONS IN THE CONTEXT OF THIS DISSERTATION

[1] A. Brenner, A. Ibarra and A. Rappelt, *Conservative constraints on the effective theory of dark matter-nucleon interactions from IceCube: the impact of operator interference*, *JCAP* **2021**(07), 012 (2021), [arXiv:2011.02929]

[2] A. Brenner, G. Herrera, A. Ibarra, S. Kang, A Rappelt, S. Scopel and G. Tomar, *Impact of operator interference in dark matter direct detection experiments*, PoS(EPS-HEP2021)061

[3] A. Brenner, G. Herrera, A. Ibarra, S. Kang, A. Rappelt, S. Scopel and G. Tomar, *The impact of operator interference and target complementarity in dark matter direct detection experiments*, Journal of Physics: Conference Series, vol. 2156 (IOP Publishing 2021), vol. 2156, p. 012069

[4] A. Brenner, G. Herrera, A. Ibarra, S. Kang, S. Scopel and G. Tomar, *Complementarity of experiments in probing the non-relativistic effective theory of dark matter-nucleon interactions*, to be published in *JCAP*, [arXiv:2203.04210]

Contents

1 Introduction 1

2 The dark matter puzzle 5
- 2.1 Observational evidence 5
  - 2.1.1 Galactic scale 5
  - 2.1.2 Galaxy cluster scale 7
  - 2.1.3 Cosmological scales 8
- 2.2 Dark matter properties and the WIMP 12
- 2.3 Dark matter searches 15
  - 2.3.1 Direct searches: Nuclear recoils 15
  - 2.3.2 Indirect searches 16
  - 2.3.3 Dark matter searches in colliders 23

3 The effective theory of dark matter-nucleon interactions 25
- 3.1 The dark matter-nucleon cross-section 25
- 3.2 The effective field theory: From quarks to nucleons 41
  - 3.2.1 Fermionic dark matter 41
  - 3.2.2 Scalar dark matter 44

4 Cross-section limits for a single experiment 47
- 4.1 Developing a method for a single experiment 47
- 4.2 Model-independent upper limits using XENON1T, PICO-60 and IceCube data 52

5 Cross-section limits for combined experiments 59
- 5.1 Developing a method for combined analysis 59
- 5.2 Upper limits on the coupling strengths from the combination of several experiments 62

6 A model- and halo-independent analysis 69

7 Conclusions 77

A Nuclear response functions 79

B Experimental likelihoods and upper limits **95**

C The solar composition and its impact on the dark matter capture **97**
C.1 The solar model AGSS09ph 97
C.2 Interpretation of the allowed parameter space 99

D Propagation of numerical errors **133**

E Experiments **137**
E.1 XENON1T 137
E.2 PICO60 138
E.3 IceCube 139

1

Introduction

Observations in the twentieth century showed that the dynamics of galaxies and galaxy clusters did not match the expectations from the Newtonian gravitational theory (or its relativistic extensions) [5–9]. A promising explanation that could account for this puzzle is the existence of an additional hidden matter component in the universe. In subsequent decades, a lot of effort was put into finding out more about the so-called “dark matter”. By today, there is evidence that the Milky Way (and other galaxies) is embedded in a halo of dark matter particles, which affect gravitationally the motion of its stars. On the other hand, the particle physics characteristics of dark matter, such as the spin, mass or interaction strength with the Standard Model particles, are still largely unconstrained [10]. If the coupling between the visible and non-visible sectors is non-zero, dark matter particles from the galactic halo that traverse a material are expected to interact with Standard Model matter. Based on this fact, a series of experiments (such as XENON1T [11] and PICO-60 [12]) have been developed with the aim of detecting the interaction of dark matter particles with nuclei in a dedicated detector. An alternative probe of the non-zero coupling between dark matter particles and nuclei is to use the Sun as a target for dark matter-nucleon interactions. Dark matter particles from the galactic halo pass through the Sun and, with some probability, interact with the solar interior, transferring energy to the target. If this energy transfer was large enough so that the velocity of the dark matter particle after the scattering is less than the local escape velocity, it becomes gravitationally bound to the Sun. After some time, this process creates a dense accumulation of dark matter in the solar core where dark matter annihilation can take place. Neutrinos produced in this process can leave the Sun almost unhindered and can be detected in a neutrino telescope, such as IceCube [13], thus providing evidence for the capture of dark matter in the Sun. Despite the deployed effort, no significant signal has been seen so far.

In interpreting theoretically the results from experiments, it is typically assumed that dark matter couples equally to protons and neutrons via the standard spin-independent and spin-dependent interactions. In general, however, this assumption does not hold in concrete models (see *e.g.* [14–23]). In the non-relativistic effective field theory (NREFT), dark matter generally interacts via 28 different couplings (for dark matter spin up to 1/2). Several of them may appear at the same time, interfering with one another. A straightforward comparison of model predictions and published limits is therefore not possible. In order to address that problem, we developed an analytical method that allows to determine model-independent upper limits on the dark matter-nucleon coupling strength in the NREFT by allowing interference among operators [1]. We apply this method to determine model-independent upper limits on the couplings using data from XENON1T [24], PICO-60 [25, 26] and IceCube [13].

The interaction between a dark matter particle and a target nucleus depends on both, the nature of dark matter and the characteristics of the target nucleus. In this thesis, we indicate the advantage of taking target nuclei with complementary properties in order to explore the vast parameter space of the NREFT of dark matter-nucleon interactions. We combine the results of several experiments, in particular XENON1T [24], PICO-60 [25, 26] and IceCube [13], and show explicitly how our model-independent upper limits on the coupling strengths become significantly strengthened [4].

Another assumption commonly made when interpreting the results from experiments is that the velocity distribution of dark matter particles in the Solar System follows a Maxwell-Boltzmann distribution. On the other hand, the true form of the dark matter velocity distribution in the solar vicinity is not positively known [27–43], and various theoretical arguments even suggest that this assumption does not hold [44–47].

To investigate the impact of such deviations, we considered distortions from the Maxwell-Boltzmann distribution and re-derived the limits on the dark matter-nucleon coupling strength for IceCube in the NREFT using the developed method.

We start this work by reviewing the current knowledge about dark matter including its observational evidence and the resulting restrictions on the properties of dark matter candidates in chapter 2. We close this part by commenting on different approaches to search for dark matter. In chapter 3, we review the construction of the NREFT of dark matter-nucleon interactions, and the calculation of the interaction rate within this framework. In chapter 4, we present our method to set model-independent limits on the dark matter-nucleon coupling strengths for a single experiment, followed by the limits obtained by using data from XENON1T, PICO-60 and IceCube. In chapter 5, we firstly generalize the method which then allows us to do a combined analysis of data of more than one experiment at a time. Secondly, we present limits resulting in the combined analysis of XENON1T, PICO-60 and IceCube data. In chapter 6, we discuss the effect of distortions from the Maxwell-Boltzmann distribution on the limits. In chapter 7, we draw conclusions. This work is supported by appendices that provide more detailed information about the nuclear response functions relevant for this thesis (A), experimental likelihoods (B), the solar composition and its impact on the dark matter capture rate (C), the propagation of numerical errors in the analysis (D) and the experiments we take into account in this work (E).

2

The dark matter puzzle

Since the 1930s, there has been increasing evidence that baryonic matter cannot make up the total amount of matter in the universe. It has been proposed that an additional matter contribution is present in the universe, contributing with five times more mass to the total mass density of the universe than baryonic matter, the so-called "dark matter". In the first section of this chapter, we address the evidence for its existence at different scales in the universe. Since the dark matter paradigm has to be consistent with observations, requirements on its characteristics can be inferred. In section 2, we comment on these properties and briefly review one of the most promising dark matter candidates. Finally, we list different techniques to search for dark matter in section 3.

2.1 Observational evidence

We briefly review the evidence for the existence of dark matter on the galactic, galaxy cluster and cosmological scale.

2.1.1 Galactic scale

Using Gauss' theorem and assuming spherical symmetry of the galaxy, it turns out that the velocity v of the stars at distance r to the galactic center reads

$$v\left(r\right) = \sqrt{\frac{GM\left(r\right)}{r}}, \tag{2.1}$$

where G is Newton's gravitational constant and $M\left(r\right)$ is the enclosed mass in a sphere with radius r. Since in the outer regions of the galaxy, the enclosed mass of visible matter remains roughly constant, it follows that the corresponding velocity is expected to decrease as

$$v(r) \propto r^{-1/2}. \tag{2.2}$$

This relation between velocity and radial distance would predict a behavior of the galactic rotation curve such as the dashed line in Fig. 2.1, which depicts the circular velocity of luminous matter, *i.e.* stars and dust, in NGC 6503 [48]. However, numerous observations especially between the 1930s and the 1980s raised doubts about that prediction.

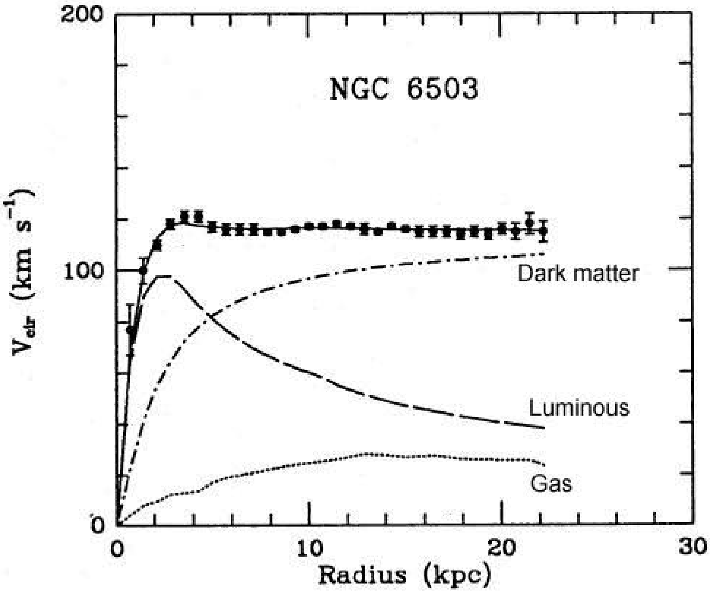

Figure 2.1: Observed rotation curve of NGC 6503 (solid) with error bars [48]. The contributions of the individual components, which are gas (dotted), luminous matter (dashed) and the required amount of dark matter to fit the observations (dash-dotted), are shown as well.

Although it turned out later that the measured numbers were too large, it was firstly reported in 1932 by Jan Hendrik Oort that stars in the solar neighborhood have speeds faster than expected assuming a mass distribution corresponding to the one of visible matter [49].

A few years later, in 1939, Horace Babcock measured that the mass-to-luminosity ratio in the Andromeda Galaxy increases with the radius [7]. Trying to find an explanation for that unexpected outcome, he ascribed it to either the absorption of light or to modified dynamics in the outer regions of the galaxy, however, he did not comment on the possibility of having a sort of missing matter. Similar to Oort's measurements, Babcock's findings emerged to be in disagreement with later observations.

In 1957, the measurements of the galactic rotation curve of the Andromeda Galaxy carried by Henk van de Hulst et al. were the first in good agreement with modern data [8]. In a related paper [9], Maarten Schmidt demonstrated that the determined rotation curve could be explained by a flattened mass distribution, which would be in disagreement with the one of the luminosity. In the following years, similar observations for rotation curves of other galaxies were made, *e.g.* by Louise Volders who found a disagreement in the rotation behavior of the Triangulum Galaxy to the one predicted by theory [50].

In subsequent decades, Vera Rubin and collaborators studied the rotation curves of 60 galaxies [51–53]. Their results indicated that the rotation curves in the outer regions of the galaxy are "flat", *i.e.* the ionized hydrogen regions move with the same speed at different radii rather than following the relation in Eq. (2.2). The constant velocity of those stars require that $M(r) \sim r$, *i.e.* the enclosed mass in the outer region needs to increase linearly with the radius. Although the visible disk is fading while moving away from the galactic center, the enclosed mass still seems to increase, also far beyond the visible part of the galaxy. A promising solution for this puzzle is to have a huge amount of non-visible matter. To give an example, for the galaxy NGC 6503, the required dark matter component is shown as dash-dotted line in Fig. 2.1. For the Milky Way this means for example that $\sim$ 95% of the matter content needs to consist of dark matter [54, 55].

2.1.2 Galaxy cluster scale

Another observation supporting the existence of dark matter is the structure of the galaxy cluster *1E 0657-56* [56, 57], better known as *Bullet Cluster*, which consists of two clusters that collided at a speed of roughly 16 million km/h, now moving apart. To render the distribution of different matter contributions, different techniques were applied. In order to map the distribution of the interstellar baryonic gas, X-ray observations were carried out, whereas weak gravitational lensing revealed the total mass distribution of the two colliding galaxy clusters. While the gas is concentrated in the center of the collision, most of the mass contribution is located outside the center and the gas contribution.

This can be explained by the fact that the luminous parts of the clusters interacted during their encounter and were slowed down. A promising interpretation why the location of the major mass contribution does apparently not coincide with the location of the luminous matter is that galaxy clusters, in particular the Bullet Cluster, are mostly consisting of (almost) collisionless dark matter [57]. In contrast to baryonic matter, dark matter does neither interact significantly with Standard Model matter nor with itself except for the gravitational attraction. This allowed the dark matter contribution to pass on the collision nearly unaffected. This is illustrated in Fig. 2.2, where the gas is colored in pink and the dark matter contribution in blue.

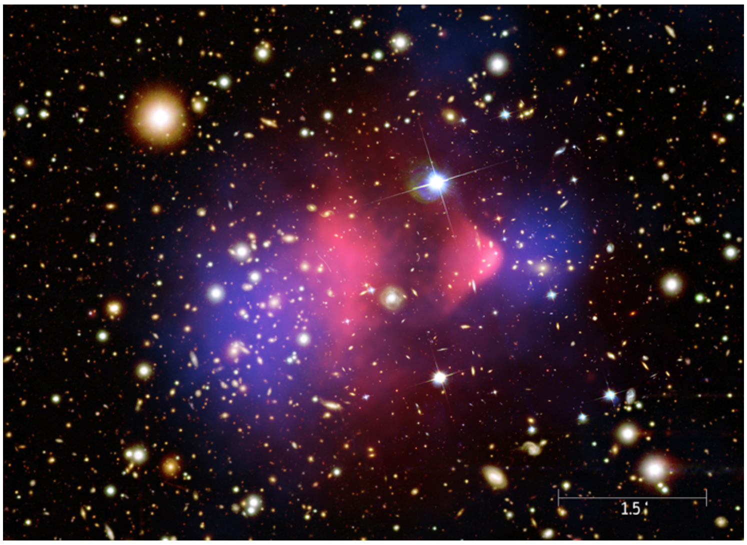

Figure 2.2: Bullet Cluster with the interstellar gas highlighted in pink and dark matter highlighted in blue [58]

2.1.3 Cosmological scales

Evidence for dark matter on cosmological scales are for example the anisotropies measured in the Cosmic Microwave Background (CMB) [59, 60]. The CMB was discovered by Penzias and Wilson in 1964 [61, 62] as an excess background temperature of ∼ 2.73 K. Its origin lies in the early universe. At the time of recombination, 380,000 years after the Big Bang, the plasma made of photons and charged particles, which the universe was composed of at that time, has been cooled down sufficiently due to the expansion of the universe such that atoms could have been formed and the universe became transparent for photons. The photons that scattered with a charged particle in the end of the opaque universe are nowadays seen as CMB.

The Cosmic Background Explorer (COBE) [63], that has been launched about two decades after the discovery of the CMB confirmed, firstly that the CMB is quite uniform and secondly that it is an almost perfect blackbody. This property can be transferred to the early universe. Despite the remarkable smoothness of the CMB, COBE later discovered small fluctuations within the CMB. The large scale fluctuations can be explained by the so-called "Sachs-Wolfe effect" [64]: Photons with low energies are nowadays observed to come from areas with high densities at the time of decoupling, in which they lost lots of energy while escaping the deep potential wells. COBE determined the difference in the photon temperature ΔT to be $\Delta T = \mathcal{O}\left(10^{-5}\right) \cdot T$ on large angular scales [65], which simultaneously is a scale for the size of the anisotropies. A possible explanation for the the origin of the small scale fluctuations are the "baryonic acoustic oscillations" (BAOs): During the epoch of photon decoupling, the universe was mostly composed of a photon-baryon fluid which was not perfectly uniformly distributed. The overdensities of the baryon-photon fluid went through cycles with the following phases: (1) The density accumulations got compressed due to their gravitational potential. (2) At some point, the induced pressure of the fluid forces its expansion. (3) While expanding, the pressure decreases, gravity takes over and causes the fluid again to compress itself. This process repeats until the photons decouple. We show an illustration of this cycle in Fig. 2.3.

Depending on what point in the cycle the photons decoupled, the photons have different temperatures. Therefore, the observed temperature fluctuations in the CMB are indicators for the density perturbations of the baryon-photon fluid and their behavior before the recombination. After the launch of the Wilkinson Microwave Anisotropy Probe (WMAP) [67] and the Planck satellite [68, 69] in subsequent decades, more data of the CMB has been collected and the resolution of the temperature fluctuations could be significantly increased. An image provided by Planck is shown in Fig. 2.4. These temperature fluctuations for different angular scales are shown in Fig. 2.5. The anisotropy on

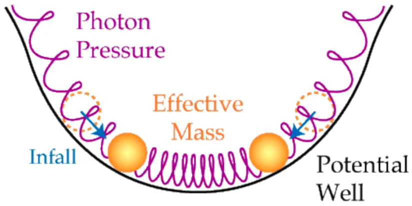

Figure 2.3: Baryonic acoustic oscillations [66]. Effective mass (yellow) of the density accumulations affected by the photon/radiation pressure (purple), causing an expansion, and the gravitational infall (blue) due to the potential well (black).

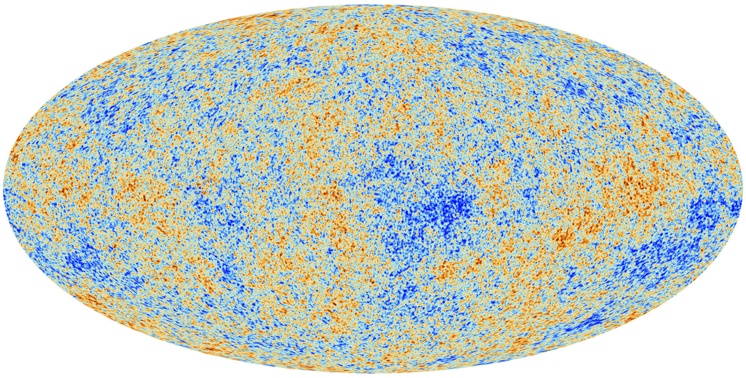

Figure 2.4: All-sky Mollweide map showing the anisotropies of the CMB as observed by Planck [70]

a certain observed angular scale today can be related to the density perturbations of the early universe [71]. Further, these oscillations are a powerful probe of the baryonic and dark matter fraction of the universe. It turns out that the heights of the second and third peaks, which appear at an angular scale of roughly 0.36°and 0.24°, respectively, fit to a universe made of roughly 25% dark matter and 5% baryonic matter. This can be explained by the different properties of baryonic and dark matter. The former interacts significantly with radiation, whereas the latter does not.

Recent measurements of Planck [73] constrain the matter density of the universe to be

$$\Omega_m h^2 = 0.1430 \pm 0.0011, \tag{2.3}$$

where dark matter makes up the majority of the matter density, namely

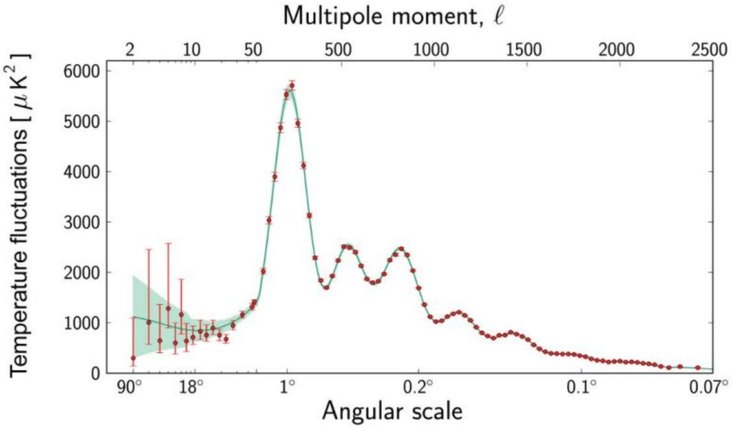

Figure 2.5: Power spectrum of the temperature fluctuations of the CMB provided by Planck (red dots including error bars) confronted with the Standard Model of cosmology, ΛCDM (green curve) [72]. The height of the second and third peak suggests that the energy content in the universe is made of 25% dark matter.

$$\Omega_d h^2 = 0.1200 \pm 0.0012, \tag{2.4}$$

whereas the density of baryonic matter is

$$\Omega_b h^2 = 0.02237 \pm 0.00015. \tag{2.5}$$

2.2 Dark matter properties and the WIMP

Despite the considerable evidence of the existence of dark matter, we do not yet know what it is exactly. However, there are several constraints on its nature coming from astronomical observations:

- Stability

  The lifetime of dark matter needs to be long compared to cosmological timescales.

- Electric charge

  If the dark matter particles had a small electric charge q_χ, or electric or magnetic dipole, they would have coupled to the baryon-photon fluid in the early universe, leaving an imprint in the power spectrum of the CMB that does not coincide with today's observations. Therefore, there are strong constraints on the electromagnetic properties of dark matter [74]. Note that these constraints do not require a completely neutral dark matter particle. There are models of the so-called "millicharged dark matter" which are still valid (see for example [75–77]). It turns out that the most stringent constraint comes from the requirement that dark matter was completely decoupled from the baryon-photon fluid during recombination. This leads to a limit of $q_\chi = 3.5 \times 10^{-7}\,(m_\chi/1\,\mathrm{GeV})^{0.58}$ for $m_\chi > 1$ GeV and $q_\chi = 4.0 \times 10^{-7}\,(m_\chi/1\,\mathrm{GeV})^{0.35}$ for $m_\chi < 1$ GeV in units of electron charge [78], where m_χ is the dark matter mass.

- Self-interactions

  There could be self-interactions among the dark matter particles themselves. Even if the dark matter particles do not couple to ordinary matter apart from gravitational interactions, the dark matter self-interactions could for example affect the merge of galaxy clusters [79]. A current constraint on the ratio of the dark matter-dark matter cross-section and the dark matter mass at 95% C.L. coming from the observations of 72 cluster collisions is $\sigma_{\chi\chi}/m_\chi < 0.47\,\mathrm{cm}^2/\mathrm{g}$ [78].

- Cold or warm dark matter

  While in the cold dark matter hypothesis, dark matter consists of weakly interacting particles moving at very small velocities compared to the speed of light, hot dark matter travels at ultra-relativistic velocities. As the name suggests, the properties of warm dark matter are transitional. Simulations of our universe assuming to be consistent of cold - or at most warm - dark matter produce structures that coincide quite well with what we observe [80–84]. In this scenario, the structure grows hierarchically, *i.e.* small objects contract under their self-interaction first and then form larger and heavier objects. Hot dark matter instead would smear out the large-scale structure of galaxies and can thus not account for all of the dark matter in the universe.

- Non-baryonic dark matter

  Firstly, we would expect for example the power spectrum of the temperature fluctuations in Fig. 2.3 to look significantly different if dark matter was of baryonic nature, *i.e.* if dark matter had the same interactions than baryons. Secondly, the strong dependence of the abundance of light elements created during the big-bang nucleosynthesis on the baryon-to-photon ratio allows to constrain the dark matter nature. Measuring the abundance of light elements such as deuterium or helium is also resulting in the exclusion of the possibility that dark matter could be of baryonic nature [85].

One of the most popular candidates fulfilling the requirements are Weakly Interacting Massive Particles (WIMPs) [86, 87]. WIMPs interact at most (sub-)weakly with Standard Model matter and their mass is expected to be in the range GeV - 10 TeV. WIMPs are proper candidates being relic dark matter particles from the early universe, originating from a time when all particles were in the state of thermal equilibrium. If temperatures had been sufficiently high, as expected in the early universe, WIMPs could have been produced by lighter Standard Model particles and vice versa, where the production of particles of the dark and Standard Model sector was balanced out. Due to the expansion of the universe, the temperatures decreased and dark matter production might have become strongly suppressed: The WIMPs were "freezing out" of equilibrium with the Standard Model matter bath (see *e.g.* [88]).

The thermally averaged annihilation cross-section that matches the observed dark matter relic density of the universe, given in Eq. (2.4), is

$$\langle \sigma_{\mathrm{ann}} v \rangle \approx 3 \times 10^{-26}\,\mathrm{cm}^3/\mathrm{s}. \tag{2.6}$$

It turned out that for typical weak-scale pair annihilation cross-sections, such as $\sigma \sim G_F^2 T^2$, where G_F is the Fermi constant and $T \sim m_\chi/20$ the typical freeze-out temperature, and for dark matter masses on the electroweak scale ($m_\chi \sim 200$ GeV) the thermal relic density coincides well with the cosmological density determined by observations [89]. This coincidence was denoted as the "WIMP miracle". Another reason to regard WIMPs as promising dark matter candidate is that they exist in models which are supposed to solve other remaining issues in theoretical particle physics, such as the hierarchy problem. One WIMP candidate is the so-called lightest neutralino in the minimal supersymmetric (SUSY) standard model that appears in SUSY models [90, 91]. In models with universal extra dimensions, the appearing lightest Kaluza-Klein particle serves as another WIMP candidate [92]. A last reason for the WIMPs' popularity which we would like to highlight is their detectability, on which we will comment in more detail in section 2.3.

2.3 Dark matter searches

2.3.1 Direct searches: Nuclear recoils

Detecting dark matter directly relies on the assumption that it does not only interact gravitationally with Standard Model matter, since in direct dark matter searches, the aim is to observe collisions of dark matter particles from the galactic halo traversing the detector and the target material in Earth-based experiments and to measure the generated nuclear recoils.

The differential number of dark matter particles interacting with a target nucleus N per recoil E_R reads

$$\frac{dN}{dE_R} = t n_\chi N_T \int_{v_{\min}} d\mathbf{w}\, f(\mathbf{w})\, w \frac{d\sigma}{dE_R}. \tag{2.7}$$

It depends on the differential dark matter-target cross-section $d\sigma/dE_R$, the dark matter velocity distribution $f(\mathbf{w})$, the number of target particles N_T and the exposure time t. In case of elastic scattering, the minimum velocity required for the incoming dark matter particle to produce a recoil with energy E_R is

$$v_{\min} = \sqrt{\frac{m_{\mathscr{N}} E_R}{2\mu_{\mathscr{N}}}}, \tag{2.8}$$

with the nucleus mass $m_{\mathscr{N}}$ and dark matter-nucleus reduced mass $\mu_{\mathscr{N}} = m_\chi m_{\mathscr{N}} / (m_\chi + m_{\mathscr{N}})$. Eq. (2.7) can be recast as

$$\frac{dN}{dE_R} = \epsilon \frac{\rho_{\text{loc}}}{m_\chi m_{\mathscr{N}}} \int_{v_{\min}} d\mathbf{w}\, f(\mathbf{w})\, w \frac{d\sigma}{dE_R}, \tag{2.9}$$

with the exposure $\epsilon = t M_T$, where M_T is the total target mass and the local dark matter halo density ρ_{loc}. The differential event rate, which is the number of observable events per unit target mass per unit time, *i.e.* $R_{\chi\mathscr{N}} = N/\epsilon$, finally reads (*e.g.* [93])

$$\frac{dR_{\chi\mathscr{N}}}{dE_R} = \frac{\rho_{\text{loc}}}{m_\chi m_{\mathscr{N}}} \int_{w_{\min}} d\mathbf{w}\, f(\mathbf{w})\, w \frac{d\sigma_{\chi\mathscr{N}}}{dE_R}. \tag{2.10}$$

A common assumption is that the Solar System is surrounded by a stationary and homogeneous dark matter halo, with the local density ρ_{loc} and the velocity distribution in the galactic frame $f(\mathbf{w})$ being normalized as

$$\int_{w \leq v_{\mathrm{max}}} dw^3 \, f(\mathbf{w}) \, = \, 1, \tag{2.11}$$

where $w \, \equiv \, |\mathbf{w}|$ and $v_{\mathrm{max}} \, = \, v_{\mathrm{esc}} \, + \, v_{\odot}$, *i.e.* the maximum possible velocity of a dark matter particle that is bound to the Milky Way in the solar rest frame, v_{max}, is determined by the sum of the galactic escape velocity v_{esc}, whose value lies in the range 499-608 km/s [94, 95], and the local speed of the Sun with respect to the halo, $v_{\odot} \, \simeq \, 244$ km/s [96–98]. While the above assumptions are rather weak, commonly a much stronger assumption is made in order to interpret dark matter searches, namely that the dark matter particles in the galactic halo follow a Maxwell-Boltzmann (MB) distribution which has the form

$$f_{\mathrm{MB}}(\mathbf{w}) \, = \, \frac{1}{\left(2\pi\sigma_w^2\right)^{3/2} N_{\mathrm{esc}}} \exp\left(-\frac{\left(\mathbf{w} \, + \, \mathbf{w}_{\odot}\right)^2}{2\sigma_w^2}\right) \quad \text{for } w \, \leq \, v_{\mathrm{max}}, \tag{2.12}$$

with the velocity dispersion $\sigma_w \, \approx \, 156$ km/s [99, 100] and the normalization constant

$$N_{\mathrm{esc}} \, = \, \mathrm{erf}\left(\frac{v_{\mathrm{esc}}}{\sqrt{2}\sigma_w}\right) \, - \, \sqrt{\frac{2}{\pi}} \frac{v_{\mathrm{esc}}}{\sigma_w} \exp\left(-\frac{v_{\mathrm{esc}}^2}{2\sigma_w^2}\right). \tag{2.13}$$

2.3.2 Indirect searches

Indirect detection techniques have the aim to detect products of dark matter annihilation or decay. The differential flux of particles on the Earth created by a point source is given by [101]

$$\frac{d\Phi}{dE} \, = \, \frac{1}{4\pi d^2} \int d^3r \, Q, \tag{2.14}$$

where the source term reads

$$Q \, = \, \frac{\rho(r)^2}{m_\chi^2} \langle\sigma v\rangle \frac{dN}{dE}. \tag{2.15}$$

Here, d denotes the distance between the Earth and a point source with the dark matter density $\rho(r)$, $\langle\sigma v\rangle$ is the thermal annihilation cross-section and

dN/dE is the differential particle number. Since the measured particle flux is composed of dark matter annihilation or decay products and (astrophysical) background, it is advantageous to search for these processes in regions in the sky in which the flux in Eq. (2.14) is largest. Promising regions are *e.g.* the cores of the Earth and the Sun, the galactic center or dwarf galaxies. They are close to telescopes located on the Earth and expected to provide a high concentration of dark matter. A hint for the annihilation of dark matter could be a *γ-ray* excess [102, 103] or *anti-nuclei* [104–107] coming from these objects. Experiments with the aim to detect such a γ-ray excess and anti-nuclei are for example Fermi-LAT [108] and AMS-02 [109], respectively.

While the dark matter density in the Milky Way can be well described by an NFW profile [110–112], and the Burkert profile [113–115] is valid for dwarf galaxies, the density distribution inside the Sun and the Earth is determined by the so-called "capture rate": In analogy to direct detection experiments where dark matter particles from the galactic halo traverse the detector material and a few of them may scatter off the contained nuclei, the dark matter particles also traverse celestial objects, such as the Sun and the Earth, and scatter off its nuclear content. If the energy transfer was large enough such that the dark matter speed after the scattering is smaller than the local escape velocity, the dark matter particle becomes gravitationally bound to the object. After some time, it might have captured a high amount of dark matter particles and becomes surrounded by its own dark matter halo. When the dark matter particles are in thermal equilibrium with the Sun's or the Earth's interior, they are expected to be strongly concentrated around the core and Standard Model particles can be produced in dark matter annihilation processes more efficiently. In the case of dark matter capture, especially *neutrinos* that are produced in the dark matter annihilation process are of specific interest, since they leave the astrophysical object nearly unhindered [13]. One experiment with the aim to detect such neutrinos is IceCube [116] (see also appendix E.3).

In this work, we will consider the search for dark matter from the Sun, which is tightly related to the scattering cross-section. In order to figure out how the expected particle flux on the Earth is related to the capture rate, we first look at the evolution of dark matter particles inside the Sun.

Evolution of the dark matter amount in the Sun

The change of the number of dark matter particles in the Sun, dN/dt, is described by the differential equation

$$\frac{dN}{dt} = C - C_E N - C_A N^2, \tag{2.16}$$

with the evaporation rate C_E of dark matter particles bound to the Sun. The evaporation process in the Sun describes the loss of captured dark matter particles that arises from the interaction between gravitationally bound dark matter and solar content, where the former gains enough energy to exceed $v_{\text{esc}}(r)$ and is capable to escape the Sun. For this to be possible, the energy transfer onto the dark matter particles needs to be significant. Since this is most efficient for $m_\chi \simeq m_{\mathcal{N}}$, evaporation from the Sun is relevant for light dark matter with masses $m_\chi \lesssim 4$ GeV according to previous studies [117–121]. Since we consider dark matter masses above 20 GeV, it is valid to drop that term and rewrite Eq. (2.16) as

$$\frac{dN}{dt} = C - C_A N^2. \tag{2.17}$$

C_A denotes the annihilation constant and reads [122]

$$C_A = \frac{V_2}{V_1^2} \langle \sigma v \rangle, \tag{2.18}$$

with effective volume

$$V_j = \int dr^3 \left(\frac{n\,(\vec{r})}{n_0} \right)^j. \tag{2.19}$$

An approximated expression for the annihilation constant in case of the Sun is given by [123]

$$C_A \simeq 1.63 \times 10^{-52} s^{-1} \left(\frac{(\sigma v)}{3 \times 10^{-26}\,\text{cm}^3\,\text{s}^{-1}} \right) \left(\frac{m_\chi}{\text{TeV}} \right)^{3/2}. \tag{2.20}$$

Solving Eq. (2.17) analytically, we obtain the number of dark matter particles captured in the Sun

$$N(t) \,=\, \sqrt{\frac{C}{C_A}}\tanh\left(\frac{t}{\tau}\right), \tag{2.21}$$

where the equilibrium time $\tau \,=\, 1/\sqrt{C\,C_A}$ denotes the time after which the capture and annihilation processes are in equilibrium.

The annihilation rate of dark matter particles is given by

$$\mathit{\Gamma}_A \,=\, \frac{1}{2}\int dr^3 n(r)^2 \langle\sigma v\rangle \tag{2.22}$$

and related to the source term via

$$\mathit{\Gamma}_A \,=\, \frac{1}{2}\int d^3r\, Q\left(\frac{dN}{dE}\right)^{-1}. \tag{2.23}$$

With the goal to relate annihilation and capture rate, we first replace the integral over the squared number density in Eq. (2.22) by V_2, which gives

$$\mathit{\Gamma}_A \,=\, \frac{1}{2}\, V_2\, n_0^2\, \langle\sigma v.\rangle \tag{2.24}$$

After using Eq. (2.18), we get

$$\mathit{\Gamma}_A \,=\, \frac{1}{2}\, C_A\, V_1^2\, n_0^2. \tag{2.25}$$

Considering the fact that $V_1^2\, n_0^2 \,=\, N(t) \,=\, C\tanh^2(t/\tau)/C_A$, we finally obtain

$$\mathit{\Gamma}_A \,=\, \frac{1}{2}\, C\, \tanh^2\left(\frac{t_\odot}{\tau}\right), \tag{2.26}$$

where the age of the Sun is denoted as $t_\odot \,=\, 4.6\times 10^9$ yr. Assuming a dark matter-nucleon interaction cross-section of $\mathcal{O}\,(10^{-47}\,\mathrm{cm}^2)$, which is currently the strongest limit[1], the equilibration time $\tau \,=\, 1/\sqrt{CC_A} \,\ll\, t_\odot$. This allows us to simplify Eq. (2.26) to

$$\mathit{\Gamma}_A \,=\, \frac{1}{2}\, C. \tag{2.27}$$

In Eq. (2.27), we see that the annihilation rate is determined by the capture rate. In the next part, we review the derivation of an expression for capture rate along the lines of [125].

---

[1] Published by XENON1T for the standard spin-independent interaction [124].

Derivation of the dark matter capture rate

Aiming to solve the dark matter and solar neutrino problem, Press and Spergel estimated the capture rate of dark matter particles in the Sun first in 1985 [126] and provided an order-of-magnitude analysis. In the following years, the formula for the capture rate of Press and Spergel was also used by other groups, such as Silk *et al.* [127], Gaisser *et al.* [128], Srednicki *et al.* [129], and Griest and Seckel [122]. Applying the derived formula to the Sun gives quite accurate results, however, it does not for other celestial bodies, *e.g.* the Earth [125]. Gould points out in [125] that the formula of Seckel and Griest suffers firstly by dropping a factor of two in their derivation and secondly by neglecting the non-zero relative motion of the Sun with respect to the frame in which the dark matter distribution is isotropic. The latter reduces the result for the capture rate by 25 %. In some cases, it is enough to multiply by the overall correction factor 1.5 to get correct results. However, it is important to note that in other cases, *e.g.* for heavy WIMPs, this factor is not enough to account for the error and so the derivation of the formula needs to be revised, as done by Gould in [125].

For the sake of general applicability, we use the accurate formalism provided by Gould. In the following, we derive the expression for the capture rate along the lines of [125]. We consider a dark matter particle getting captured due to sufficient energy loss in a scattering process inside a thin spherical shell of the celestial body. Note that this shell is in a spherically symmetric gravitational field, it has radius r and thickness dr and the escape velocity at distance r is $v_{\text{esc}}(r)$. Asymptotically far away from the gravitational source, the dark matter particles have the velocity distribution $f(v)$. Assuming the velocity distribution to be isotropic, we can write $f(v)\,dv = \frac{1}{2}f(v)\,dv\,d\cos\theta$, where θ is the angle relative to the radial direction. With this, the flux of dark matter particles going inward across a spherical surface of radius R, where R is so large that the gravitational potential can be neglected on the surface, reads

$$\mathcal{F} = \frac{1}{2}\,f(v)\,v\,\cos\theta\,dv\,d\cos\theta \tag{2.28}$$

or alternatively

$$\mathcal{F} \;=\; \frac{1}{4}\, f(v)\, v\, dv\, d\cos^2\theta, \tag{2.29}$$

where we changed the integrand from $d\cos\theta$ to $d\cos^2\theta$. Note that θ is constrained as $0 \;\leq\; \theta \;<\; \frac{\pi}{2}$. We do not consider the complementary interval $\frac{\pi}{2} \;\leq\; \theta \;\leq\; \pi$, since this accounts for dark matter particles moving outward.

As next step, we relate the angle θ with the angular momentum J via

$$J \;=\; R\, v\, \sin\theta \quad \text{and} \quad d\cos^2\theta \;=\; \frac{dJ^2}{R^2\, v^2}. \tag{2.30}$$

After summing over all area elements, the rate of incoming dark matter particles R_χ within a dJ^2-interval is

$$R_\chi \;=\; 4\pi R^2\, \frac{1}{4}\, f(v) v\, dv\, \frac{dJ^2}{R^2\, v^2}. \tag{2.31}$$

The relation between the asymptotic velocity v and the (accelerated) velocity $w(r)$ at distance r is

$$w(r) \;=\; \sqrt{v^2 \;+\; v_{\text{esc}}(r)^2}. \tag{2.32}$$

To capture a dark matter particle, its initial speed $w(r)$ needs to be decreased to speed $w'(r)$ that is less then escape velocity $v_{\text{esc}}(r)$. The rate for those scatterings is

$$\Omega^-_{v_{\text{esc}}}(w) \;=\; \sum_a n_a(r) w\, \Theta\left(\frac{\mu_a}{\mu^2_{+,a}} \;-\; \frac{v^2}{w^2}\right) \int_{E_l\, v^2/w^2}^{E_l\, \mu_i/\mu^2_{+,a}} dE_R \frac{d\sigma_a}{dE_R}\left(w^2, q^2\right), \tag{2.33}$$

with the number density $n_a(r)$ of nucleus type a, $\mu_a \;=\; m_\chi/m_{\mathcal{N}_a}$, $\mu^2_{+,a} \;=\; \left(\mu_a \pm 1\right)/2$ and $E_l \;=\; m_\chi w^2/2$. The according probability p is

$$p\left(w \to w' \;<\; v_{\text{esc}}\right) \;=\; \Omega^-_{v_{\text{esc}}}(w)\frac{dl}{w}, \tag{2.34}$$

where dl/w is the differential time required for the dark matter particles to traverse the shell. The differential distance dl that the dark matter particle travels in the shell is

$$dl \;=\; \frac{dr}{\cos\theta}. \tag{2.35}$$

With $J = rw\sin\theta$ we can write instead

$$dl = \frac{dr}{\sqrt{1 - \frac{J^2}{r^2 w^2}}}. \tag{2.36}$$

Using $dr = \frac{dJ}{w\sin\theta}$, we finally obtain the differential time

$$dt = 2 \times \frac{1}{w}\left(1 - \frac{J^2}{r^2 w^2}\right)^{-\frac{1}{2}} dJ\, \Theta(rw - J). \tag{2.37}$$

Note that we added a factor of two and the Heaviside function by hand. The former arises, since a dark matter particle that moves through the shell will always pass the distance dl twice. The latter must be added, since we need to ensure that only dark matter particles with an angular momentum that is small enough, *i.e.* $rw < J$, traverses the shell. Multiplying Eqs. (2.31) and (2.34), we obtain

$$4\pi r^2 dr\, \frac{f(v)dv}{v}\, w\, \Omega^-_{u_{\mathrm{esc}}}(w). \tag{2.38}$$

Integrating over all velocities, the differential dark matter capture rate writes

$$\frac{dC}{dV} = \int dv \frac{f(v)}{v} w\, \Omega^-_{u_{\mathrm{esc}}}(w). \tag{2.39}$$

Since we assume that the Sun is spherically symmetric, the integrals over the spatial angles can be calculated analytically. After applying the Heaviside function, the total dark matter capture rate reads [125, 130]

$$\begin{aligned} C = &\sum_a \int_0^{R_\odot} dr\, 4\pi\, r^2\, n_a(r)\, \frac{\rho_{\mathrm{loc}}}{m_\chi} \int_{v \leq v^{(\mathrm{Sun})}_{\mathrm{max},a}(r)} d^3v\, \frac{f(\vec{v})}{v}\, w^2(r) \\ &\times \int_{m_\chi v^2/2}^{2\mu_a^2 w^2(r)/m_a} dE_R\, \frac{d\sigma_a}{dE_R}(w(r), E_R)\ . \end{aligned} \tag{2.40}$$

The lower limit of the energy integral is the minimum energy the dark matter particle has to lose in the scattering process to be captured. The upper limit is the maximum possible energy transfer, obtained from energy and momentum conservation, with the target mass m_a. The upper limit for the velocity integral

$$v^{(\mathrm{Sun})}_{\mathrm{max,a}}(r) = 2\, u_{\mathrm{esc}}(r) \frac{\sqrt{m_\chi m_{T_a}}}{|m_\chi - m_{T_a}|} \tag{2.41}$$

accounts for the cases in which the minimum needed energy transfer is larger than the maximum kinematic limit. In this case, we would mathematically obtain a negative capture rate, although the capture rate would actually be zero.

2.3.3 Dark matter searches in colliders

Another possibility to search for dark matter is its production in a high-energy collider. Here, dark matter particles that might have been produced in the high temperature epoch of the early universe, such as WIMPs, could also be produced in high-energy colliders, such as the Large Hadron Collider (LHC), provided that the dark matter particles are not extraordinarily heavy and have a non-zero coupling to the Standard Model sector. The LHC is a proton-proton collider. Each proton beam runs at an energy of 7 TeV resulting in a maximum center-of-mass energy of 13.6 TeV [131, 132]. Collider experiments with focus on the detection of dark matter are *e.g.* the ATLAS [133], CMS [134] and LHCb [135] experiments which include up to 36 fb^{-1} of proton-proton collision data collected in 2017 during the 2015-2018 LHC run at 13 TeV center-of-mass energy (Run 2). Since the (produced) dark matter particles interact at most weakly with particles from the visible sector, they will pass through and leave the detector nearly unhindered, similar to neutrinos. Therefore, one makes use of the energy and momentum conservation requirement. The so-called "missing energy" caused by the non-detection of produced particles might be a hint for the production of dark matter particles. Since in hadron colliders the detectors are blind in the longitudinal direction, only the transverse component of the momentum can be used to investigate a possible dark matter production. This is the so-called "transverse missing energy", $E_{\mathrm{T}}^{\mathrm{miss}}$.

Concrete targets in collider searches for dark matter are for example dark matter models considering effective field theories with heavy mediators (*e.g.* [136]), models in which dark matter interacts with ordinary matter via exchange of a Higgs or Z boson (*e.g.* [137, 138]) or supersymmetry (*e.g.* [139]), to name a few. In particular, the following possible dark matter signals are in the focus of interest [140]:

(1) Missing transverse energy caused by a dark matter particle that leaves

the detector unhindered which was produced together with a detected Standard Model particle.

(2) Anomaly in the invariant mass distribution of the di-jet or di-lepton in the form of a bump.

(3) Anomaly in the angular distribution of the di-jet in the form of an excess of events originated by a dark matter mediator.

For the former possibility, the dark matter particle interacts directly with the Standard Model sector, whereas the two latter are associated with the interaction between a dark matter mediator and ordinary matter. Similar to other kinds of dark matter searches, a signal hinting towards the existence of dark matter has not yet been observed. However, limits can be set on the dark matter mass, couplings and cross-sections. No matter if there is a hint for dark matter in collider searches or not, the results need to be confronted with the ones from direct and/or indirect dark matter searches, since a potential dark matter signal in colliders cannot be positively identified as such.

3

The effective theory of dark matter-nucleon interactions

In this chapter, we review the construction of the non-relativistic effective field theory along the lines of [141–144].

3.1 The dark matter-nucleon cross-section

We are interested in the dark matter-nucleon effective interactions in the non-relativistic limit for elastic scattering processes, such as

$$\chi(\mathbf{p}) + N(\mathbf{k}) \to \chi(\mathbf{p}') + N(\mathbf{k}'), \tag{3.1}$$

where $\mathbf{p}$ $(\mathbf{p}')$ and $\mathbf{k}$ $\left(\mathbf{k}'\right)$ are the three-momenta of the incoming (outgoing) dark matter particle χ and nucleon N, respectively. The interaction Lagrangian of interest has the contact form

$$\mathcal{L}_{\text{int}} = \bar{\chi}\hat{\mathcal{O}}_\chi \chi \bar{N} \hat{\mathcal{O}}_N N = \hat{\mathcal{O}} \bar{\chi}\chi \bar{N} N, \tag{3.2}$$

with the dark matter and nucleon operators $\hat{\mathcal{O}}_\chi$ and $\hat{\mathcal{O}}_N$, respectively. The effective operator $\hat{\mathcal{O}}$ is created by $\hat{\mathcal{O}}_\chi$ and $\hat{\mathcal{O}}_N$. Considering scatterings up to second order in momentum, we will obtain a set of effective operators $\hat{\mathcal{O}}_i$, whose properties are determined by imposing relevant requirements: In order to build the effective theory, we have to ensure that the operators

- conserve momentum and energy,
- are Galilean invariant,
- are Hermitian.

Momentum conservation implies that between $\mathbf{p}$, $\mathbf{p}'$, $\mathbf{k}$ and $\mathbf{k}'$, there are only three independent momenta which we choose to be $\mathbf{p}$, $\mathbf{k}$ and the momentum transfer from the nucleon to the dark matter particle

$$\mathbf{q} \equiv \mathbf{p}' - \mathbf{p} = \mathbf{k} - \mathbf{k}'. \tag{3.3}$$

Since *Galilean invariance* demands quantities to be invariant under a constant shift of velocities, we find that $\mathbf{q}$ satisfies the requirement, as the momentum transfer describes a difference of momenta. The single momenta $\mathbf{p}$ and $\mathbf{k}$ instead are affected by a constant velocity shift. Therefore we rather use the (Galilean invariant) relative incoming velocity

$$\mathbf{v} \equiv \frac{\mathbf{p}}{m_\chi} - \frac{\mathbf{k}}{m_N} \equiv \mathbf{v}_{\chi,\text{in}} - \mathbf{v}_{N,\text{in}} \tag{3.4}$$

of the dark matter particle and the nucleon, where m_χ and $\mathbf{v}_{\chi,\text{in}}$ (m_N and $\mathbf{v}_{N,\text{in}}$) denote the dark matter mass and incoming velocity (nucleon mass and incoming velocity), respectively.

Energy conservation implies that the initial state energy equals the final state energy, *i.e.*

$$E_\text{in} = E_\text{out}. \tag{3.5}$$

Here, it is convenient to work in the center-of-mass frame. Then, $E_\text{in} = \frac{1}{2}\mu_N v^2$ and $E_\text{out} = \frac{1}{2}\mu_N \left(\mathbf{v} + \frac{\mathbf{q}}{\mu_N}\right)^2$, with the nucleon reduced mass $\mu_N = \frac{m_\chi m_N}{m_\chi + m_N}$. Together with Eq. (3.5), we obtain

$$\mathbf{v} \cdot \mathbf{q} = -\frac{q^2}{2\mu_N}. \tag{3.6}$$

After applying the kinematic constraints, we need to guarantee the *Hermiticity* of the interaction. Considering the fact that Hermitian conjugation exchanges incoming for outgoing particles, the momentum transfer $\mathbf{q}$ is clearly anti-Hermitian. Therefore we work with the Hermitian quantity $i\mathbf{q}$ instead. Similarly as for the momentum transfer, we have to construct a new quantity containing the relative incoming velocity, since $\mathbf{v} \xrightarrow{\dagger} \mathbf{v} + \frac{\mathbf{q}}{\mu_N}$ is not Hermitian. We introduce the perpendicular velocity $\mathbf{v}^\perp$ that fulfills $\mathbf{v}^\perp \cdot \mathbf{q} = 0$. Together with Eq. (3.6), we obtain the Hermitian quantity

$$\mathbf{v}^{\perp} \equiv \mathbf{v} + \frac{\mathbf{q}}{2\mu_N}. \tag{3.7}$$

Apart from the momentum transfer and relative incoming velocity, the interaction can also depend on the dark matter and nuclear spins $\mathbf{S}_\chi$ and $\mathbf{S}_N$, respectively, where

$$\mathbf{S}_{\chi/N} = \begin{cases} 0 & \text{for spin-0} \\ \frac{1}{2}\sigma & \text{for spin-}\frac{1}{2}, \end{cases}$$

with the Pauli matrices σ. $\mathbf{S}_\chi$ and $\mathbf{S}_N$ fulfill the constraints formulated above. Finally, our set of Galilean invariant and Hermitian operators is

$$i\hat{q}, \quad \hat{v}^{\perp}, \quad \hat{S}_\chi, \quad \hat{S}_N. \tag{3.8}$$

Before we construct the operators, we think about a possible categorization. The operators can be classified as transforming evenly or oddly under parity (P) and time reversal (T). The specific properties of an operator after the transformation under P- and T-symmetry are determined by the corresponding transformation behavior of its constituents, $i\hat{q}$, $\hat{v}^{\perp}$ and $\hat{S}$. Whereas $\hat{v}^{\perp}$ and $\hat{S}$ ($i\hat{q}$ and $\hat{v}^{\perp}$) transform oddly under time reversal (parity), $i\hat{q}$ ($\hat{S}$) transforms evenly. In the following table we provide a summary:

	T	P
$i\mathbf{q}$	$+1$	-1
$\mathbf{v}^{\perp}$	-1	-1
$\mathbf{S}_\chi$, $\mathbf{S}_N$	-1	$+1$

Furthermore, the operators can be classified into dark matter spin-independent (SI) and dark matter spin-dependent (SD).

In order to construct the effective operators, we consider combinations of the operators in expression (3.8) at most linear in $\hat{S}_\chi$, $\hat{S}_N$ and $\hat{v}^{\perp}$ and at most quadratic in $\hat{q}$, except for $\hat{\mathcal{O}}_{15}$, which is cubic in $\hat{q}$. The resulting effective operators are given in the following table:

		T-even
1	P-even, SI	$\hat{\mathcal{O}}_1 = \mathbb{1}$, $\hat{\mathcal{O}}_2 = \left(\hat{v}^{\perp}\right)^2$, $\hat{\mathcal{O}}_3 = i\hat{S}_N \cdot \left(\hat{q} \times \hat{v}^{\perp}\right)$
2	P-even, SD	$\hat{\mathcal{O}}_4 = \hat{S}_\chi \cdot \hat{S}_N$, $\hat{\mathcal{O}}_5 = i\hat{S}_\chi \cdot \left(\hat{q} \times \hat{v}^{\perp}\right)$, $\hat{\mathcal{O}}_6 = \left(\hat{S}_\chi \cdot \hat{q}\right)\left(\hat{S}_N \cdot \hat{q}\right)$
3	P-odd, SI	$\hat{\mathcal{O}}_7 = \hat{S}_N \cdot \hat{v}^{\perp}$
4	P-odd, SD	$\hat{\mathcal{O}}_8 = \hat{S}_\chi \cdot \hat{v}^{\perp}$, $\hat{\mathcal{O}}_9 = i\hat{S}_\chi \cdot \left(\hat{S}_N \times \hat{q}\right)$
		T-odd
5	P-odd, SI	$\hat{\mathcal{O}}_{10} = i\hat{S}_N \cdot \hat{q}$
6	P-odd, SD	$\hat{\mathcal{O}}_{11} = i\hat{S}_\chi \cdot \hat{q}$,

The two operators $\hat{\mathcal{O}}_1$ and $\hat{\mathcal{O}}_4$ highlighted in blue correspond to the standard spin-independent and spin-dependent interactions, respectively. Any interaction of the non-relativistic effective field theory is of the form $\prod_{i=1}^{11} \hat{\mathcal{O}}_i^{n_i}$ with $\hat{\mathcal{O}}_1$ - $\hat{\mathcal{O}}_{11}$ as building blocks. We keep operators up to order $\mathcal{O}\left(q^2, \mathbf{q} \cdot \mathbf{v}\right)$. Therefore, we additionally consider the operators

$$\begin{aligned}
\hat{\mathcal{O}}_{12} &= \hat{\mathcal{O}}_{10}\hat{\mathcal{O}}_5 = \hat{S}_\chi \cdot \left(\hat{S}_N \times \hat{v}^{\perp}\right) \\
\hat{\mathcal{O}}_{13} &= \hat{\mathcal{O}}_{10}\hat{\mathcal{O}}_8 = i\left(\hat{S}_\chi \cdot \hat{v}^{\perp}\right)\left(\hat{S}_N \cdot \hat{q}\right) \\
\hat{\mathcal{O}}_{14} &= \hat{\mathcal{O}}_{11}\hat{\mathcal{O}}_7 = i\left(\hat{S}_\chi \cdot \hat{q}\right)\left(\hat{S}_N \cdot \hat{v}^{\perp}\right) \\
\hat{\mathcal{O}}_{15} &= \hat{\mathcal{O}}_{11}\hat{\mathcal{O}}_3 = -\left(\hat{S}_\chi \cdot \hat{q}\right)\left[\left(\hat{S}_N \times \hat{v}^{\perp}\right) \cdot \hat{q}\right].
\end{aligned}$$

Note that interference is possible among

- $\hat{\mathcal{O}}_1$ and $\hat{\mathcal{O}}_3$
- $\hat{\mathcal{O}}_4$, $\hat{\mathcal{O}}_5$ and $\hat{\mathcal{O}}_6$
- $\hat{\mathcal{O}}_8$ and $\hat{\mathcal{O}}_9$
- $\hat{\mathcal{O}}_{11}$, $\hat{\mathcal{O}}_{12}$ and $\hat{\mathcal{O}}_{15}$.

The final list of operators in the non-relativistic effective field theory up to $\mathcal{O}\left(q^2, \mathbf{q}\cdot\mathbf{v}\right)$ describing dark matter-nucleon interactions with an exchange of a particle with spin-0 or spin-1 is shown in Tab. 3.1. Further, note that we show $\hat{\mathcal{O}}_2$, shaded in gray, for the sake of completeness. However, it is typically neglected in the listing of effective operators, since this cannot be a leading-order operator in effective theories. An advantage of the categorization into these 6 groups is that we can directly see which operators could interfere with one another: Interference is not possible for operators in different groups[1]. To this order, the non-relativistic dark matter-nucleon (χN) interactions are most generically described by the Hamiltonian

$\hat{\mathcal{O}}_1 = 1_\chi 1_N$

$\hat{\mathcal{O}}_3 = i\hat{S}_N \cdot (\frac{\hat{q}}{m_N} \times \hat{v}^\perp)$

$\hat{\mathcal{O}}_4 = \hat{S}_\chi \cdot \hat{S}_N$

$\hat{\mathcal{O}}_5 = i\hat{S}_\chi \cdot (\frac{\hat{q}}{m_N} \times \hat{v}^\perp)$

$\hat{\mathcal{O}}_6 = (\hat{S}_\chi \cdot \frac{\hat{q}}{m_N})(\hat{S}_N \cdot \frac{\hat{q}}{m_N})$

$\hat{\mathcal{O}}_7 = \hat{S}_N \cdot \hat{v}^\perp$

$\hat{\mathcal{O}}_8 = \hat{S}_\chi \cdot \hat{v}^\perp$

$\hat{\mathcal{O}}_9 = i\hat{S}_\chi \cdot (\hat{S}_N \times \frac{\hat{q}}{m_N})$

$\hat{\mathcal{O}}_{10} = i\hat{S}_N \cdot \frac{\hat{q}}{m_N}$

$\hat{\mathcal{O}}_{11} = i\hat{S}_\chi \cdot \frac{\hat{q}}{m_N}$

$\hat{\mathcal{O}}_{12} = \hat{S}_\chi \cdot (\hat{S}_N \times \hat{v}^\perp)$

$\hat{\mathcal{O}}_{13} = i(\hat{S}_\chi \cdot \hat{v}^\perp)(\hat{S}_N \cdot \frac{\hat{q}}{m_N})$

$\hat{\mathcal{O}}_{14} = i(\hat{S}_\chi \cdot \frac{\hat{q}}{m_N})(\hat{S}_N \cdot \hat{v}^\perp)$

$\hat{\mathcal{O}}_{15} = -(\hat{S}_\chi \cdot \frac{\hat{q}}{m_N})\Big[(\hat{S}_N \times \hat{v}^\perp) \cdot \frac{\hat{q}}{m_N}\Big]$

Table 3.1: Non-relativistic Galilean invariant operators for dark matter with spin-$\frac{1}{2}$.

$$\hat{\mathcal{H}}_{\chi N}\left(\mathbf{r}\right) = \sum_{\tau=0}^{1}\sum_{i=1}^{15} c_i^\tau \hat{\mathcal{O}}_i\left(\mathbf{r}\right) t^\tau, \tag{3.9}$$

---

[1] Notice that operators within one group do not necessarily interfere with one another.

where i labels the non-relativistic interaction types. Remember that index $i = 2$ is skipped in the summation. Further, c_i^τ is the Wilson coefficient for operator $\hat{\mathcal{O}}_i$ and t^τ is the isospin matrix with $t^0 = \mathbb{1}$ and $t^1 = \sigma_3$, the third Pauli matrix. For the couplings, there exist two bases which are commonly used, namely the proton-neutron basis ($\tau = p\,(n)$ for proton (neutron) component) and the isospin basis ($\tau = 0\,(1)$ for isoscalar (isovector) component). The couplings in both bases can be calculated from the Hamiltonian. The result is

$$\begin{aligned} c_i^p &= \frac{1}{2}\left(c_i^0 + c_i^1\right) \\ c_i^n &= \frac{1}{2}\left(c_i^0 - c_i^1\right). \end{aligned} \tag{3.10}$$

Additionally summing over all nucleons a in the nucleus with mass number A, the most general Hamilton operator describing the dark matter-nucleon interaction reads

$$\hat{\mathcal{H}}_{\chi\mathcal{N}}\left(\mathbf{r}\right) = \sum_{a=1}^{A}\sum_{\tau=0}^{1}\sum_{i=1}^{15} c_i^\tau \hat{\mathcal{O}}_i^a\left(\mathbf{r}\right) t^{\tau,a}. \tag{3.11}$$

In order to determine the dark matter-nucleus cross-section, we calculate the matrix elements on nucleon level, *i.e.* for nucleons inside the nucleus that are involved in the interaction. It is advantageous to distinguish between the motion of the nucleus center of mass and the intrinsic motion of the nucleon, which points relative to the nucleus center of mass. This yields the coordinate space representations

$$\hat{\mathbf{q}} = -i\overleftarrow{\nabla}_{\mathbf{x}}\,\delta\left(\mathbf{x} - \mathbf{y} + \tilde{\mathbf{r}}\right) - i\delta\left(\mathbf{x} - \mathbf{y} + \tilde{\mathbf{r}}\right)\overrightarrow{\nabla}_{\mathbf{x}} \tag{3.12}$$

$$\hat{\mathbf{v}}^\perp = \hat{\mathbf{v}}^\perp_{\mathcal{N}} + \hat{\mathbf{v}}^\perp_{N}, \tag{3.13}$$

where

$$\hat{\mathbf{v}}^{\perp}_{\mathcal{N}} = \delta\left(\mathbf{x} - \mathbf{y} + \tilde{\mathbf{r}}\right)\left(i\frac{\overrightarrow{\nabla}_{\mathbf{x}}}{m_{\mathcal{N}}} - i\frac{\overrightarrow{\nabla}_{\mathbf{y}}}{m_{\chi}}\right) + \frac{1}{2\mu_{\mathcal{N}}}\hat{\mathbf{q}} \tag{3.14}$$

$$\hat{\mathbf{v}}^{\perp}_{N} = \frac{1}{2m_N}\left[i\overleftarrow{\nabla}_{\tilde{\mathbf{r}}}\,\delta\left(\tilde{\mathbf{r}} - \tilde{\mathbf{r}}_a\right) - i\delta\left(\tilde{\mathbf{r}} - \tilde{\mathbf{r}}_a\right)\overrightarrow{\nabla}_{\tilde{\mathbf{r}}}\right]. \tag{3.15}$$

Here, $\mu_{\mathcal{N}} = \frac{m_\chi m_{\mathcal{N}}}{m_\chi + m_{\mathcal{N}}}$ is the dark matter-nucleus reduced mass. Further, $\nabla_{\mathbf{x}}$ ($\nabla_{\mathbf{y}}$) and $\nabla_{\tilde{\mathbf{r}}}$ act on the center-of-mass wave function of the nucleus (dark matter particle) at position $\mathbf{x}$ ($\mathbf{y}$) and constituent nucleon wave function at position $\tilde{\mathbf{r}}$, respectively. In a frame where the origin is in the nucleus center of mass, $\tilde{\mathbf{r}}$ ($\tilde{\mathbf{r}}_a$) denotes the radial coordinate of the dark matter particle (nucleon a). Looking at the operators in Tab. 3.1 and Eqs. (A.2) and (3.13), it becomes clear that the $\tilde{\mathbf{r}}_a$-dependence can occur in five different forms. In order to categorize those dependencies, we form the Hamiltonian in Eq. (3.11) to

$$\mathcal{H}_{\chi\mathcal{N}}\left(\hat{\tilde{r}}\right) = \sum_{\tau=0}^{1}\left(\hat{l}_0^{\tau}\hat{\rho}_0^{\tau}\left(\tilde{\mathbf{r}}\right) + \hat{l}_{0A}^{\tau}\hat{\rho}_{0A}^{\tau}\left(\tilde{\mathbf{r}}\right) + \hat{\mathbf{l}}_5^{\tau}\hat{\rho}_5^{\tau}\left(\tilde{\mathbf{r}}\right) + \hat{\mathbf{l}}_M^{\tau}\hat{\rho}_M^{\tau}\left(\tilde{\mathbf{r}}\right) + \hat{\mathbf{l}}_E^{\tau}\hat{\rho}_E^{\tau}\left(\tilde{\mathbf{r}}\right)\right). \tag{3.16}$$

Here, $\hat{\rho}_0^{\tau}$ and $\hat{\rho}_{0A}^{\tau}$ denote the nuclear vector and axial charges, and $\hat{\rho}_5^{\tau}$, $\hat{\rho}_M^{\tau}$ and $\hat{\rho}_E^{\tau}$ the nuclear spin, convection and nuclear spin-velocity currents, respectively. The concrete expressions for those charges and currents read

$$\begin{aligned}
\hat{\rho}_0^{\tau}\left(\tilde{\mathbf{r}}\right) &\coloneqq \sum_{a=1}^{A}\delta\left(\tilde{\mathbf{r}} - \tilde{\mathbf{r}}_a\right)t^{\tau,a} = \sum_{a=1}^{A}\mathbb{1}_a\,t^{\tau,a}\\
\hat{\rho}_{0A}^{\tau}\left(\tilde{\mathbf{r}}\right) &\coloneqq \sum_{a=1}^{A}\sigma(a)\,\hat{\mathbf{v}}^{\perp}_{N}\,t^{\tau,a}\\
\hat{\rho}_5^{\tau}\left(\tilde{\mathbf{r}}\right) &\coloneqq \sum_{a=1}^{A}\sigma(a)\,\delta\left(\tilde{\mathbf{r}} - \tilde{\mathbf{r}}_a\right)t^{\tau,a} = \sum_{a=1}^{A}\sigma(a)\,\mathbb{1}_a t^{\tau,a}\\
\hat{\rho}_M^{\tau}\left(\tilde{\mathbf{r}}\right) &\coloneqq \sum_{a=1}^{A}\hat{\mathbf{v}}^{\perp}_{N}\\
\hat{\rho}_E^{\tau}\left(\tilde{\mathbf{r}}\right) &\coloneqq \sum_{a=1}^{A}\sigma(a)\times\hat{\mathbf{v}}^{\perp}_{N},
\end{aligned} \tag{3.17}$$

with the Pauli matrices σ_a acting on the ath nucleon and $\mathbb{1}_a$ being equivalent to $\delta\left(\tilde{\mathbf{r}} - \tilde{\mathbf{r}}_a\right)$ in coordinate space [144]. Further, the operators $\hat{l}_k^{\tau}$ are given by

[143, 144]

$$
\begin{aligned}
\hat{l}_0^\tau &= c_1^\tau + i\left(\frac{\hat{\mathbf{q}}}{m_N}\times\hat{\mathbf{v}}^\perp_{\mathcal{N}}\right)\hat{\mathbf{S}}_\chi\, c_5^\tau + \hat{\mathbf{v}}^\perp_{\mathcal{N}}\,\hat{\mathbf{S}}_\chi\, c_8^\tau + i\frac{\hat{\mathbf{q}}}{m_N}\hat{\mathbf{S}}_\chi\, c_{11}^\tau \\
\hat{l}_{0A}^\tau &= -\frac{1}{2}\left(c_7^\tau + i\frac{\hat{\mathbf{q}}}{m_N}\hat{\mathbf{S}}_\chi\, c_{14}^\tau\right) \\
\hat{\mathbf{l}}_5^\tau &= \frac{1}{2}\Bigg(i\frac{\hat{\mathbf{q}}}{m_N}\times\hat{\mathbf{v}}^\perp_{\mathcal{N}}\, c_3^\tau + \hat{\mathbf{S}}_\chi\, c_4^\tau + \frac{\hat{\mathbf{q}}}{m_N}\frac{\hat{\mathbf{q}}}{m_N}\hat{\mathbf{S}}_\chi\, c_6^\tau + \hat{\mathbf{v}}^\perp_{\mathcal{N}}\, c_7^\tau i\frac{\hat{\mathbf{q}}}{m_N}\times\hat{\mathbf{S}}_\chi\, c_9^\tau + i\frac{\hat{\mathbf{q}}}{m_N}\, c_{10}^\tau \\
&\qquad + \hat{\mathbf{v}}^\perp_{\mathcal{N}}\times\hat{\mathbf{S}}_\chi\, c_{12}^\tau + i\frac{\hat{\mathbf{q}}}{m_N}\hat{\mathbf{v}}^\perp_{\mathcal{N}}\hat{\mathbf{S}}_\chi\, c_{13}^\tau + i\hat{\mathbf{v}}^\perp_{\mathcal{N}}\frac{\hat{\mathbf{q}}}{m_N}\hat{\mathbf{S}}_\chi\, c_{14}^\tau + \frac{\hat{\mathbf{q}}}{m_N}\times\hat{\mathbf{v}}^\perp_{\mathcal{N}}\frac{\hat{\mathbf{q}}}{m_N}\hat{\mathbf{S}}_\chi\, c_{15}^\tau\Bigg) \\
\hat{\mathbf{l}}_M^\tau &= i\frac{\hat{\mathbf{q}}}{m_N}\times\hat{\mathbf{S}}_\chi\, c_5^\tau - \hat{\mathbf{S}}_\chi\, c_8^\tau \\
\hat{\mathbf{l}}_E^\tau &= \frac{1}{2}\left(\frac{\hat{\mathbf{q}}}{m_N}c_3^\tau + i\hat{\mathbf{S}}_\chi\, c_{12}^\tau - \frac{\hat{\mathbf{q}}}{m_N}\times\hat{\mathbf{S}}_\chi\, c_{13}^\tau - i\frac{\hat{\mathbf{q}}}{m_N}\frac{\hat{\mathbf{q}}}{m_N}\hat{\mathbf{S}}_\chi\, c_{15}^\tau\right).
\end{aligned}
\tag{3.18}
$$

In order to get the scattering cross-section, we first calculate the transition amplitude

$$\langle f|\, H_{\chi\mathcal{N}}\, |i\rangle = (2\pi)^3\, \delta\left(\mathbf{k}'_{\mathcal{N}} + \mathbf{p}' - \mathbf{k}_{\mathcal{N}} - \mathbf{p}\right) i\mathcal{M}_{NR} \tag{3.19}$$

between the initial state $|i\rangle$ and final state $\langle f|$. We obtain $H_{\chi\mathcal{N}}$ by integrating the Hamiltonian in Eq. (3.16) over the spatial coordinates. In the initial state, there is the nucleus with nucleus initial state $|\mathbf{k}_{\mathcal{N}}, J, M_J, T, M_T\rangle$ with the nuclear spin J, nuclear isospin T, and the associated magnetic quantum numbers M_J and M_T, and the dark matter particle with initial state $|\mathbf{p}, j_\chi, M_\chi\rangle$ with the dark matter spin magnetic quantum number M_χ. The total initial state is then given by $|i\rangle = |\mathbf{k}_{\mathcal{N}}, J, M_J, T, M_T\rangle \otimes |\mathbf{p}, j_\chi, M_\chi\rangle$. Analogously, we obtain the expression that describes the final state: $\langle f| = \langle \mathbf{p}', j_\chi, M_\chi| \otimes \langle \mathbf{k}'_{\mathcal{N}}, J, M_J, T, M_T|$.

Next we perform a multipole expansion along the lines of [144]. We define

$$\langle \hat{\mathbf{l}}\,\rangle := \langle j_\chi, M_\chi|\, \hat{\mathbf{l}}\left[\mathbf{q}, \mathbf{v}^\perp_{\mathcal{N}}, \hat{\mathbf{S}}_\chi\right] |j_\chi, M_\chi\rangle\,, \tag{3.20}$$

where $\hat{\mathbf{l}}$ stands for one of the operators $\hat{l}_0^\tau$, $\hat{\mathbf{l}}_5^\tau$, $\hat{\mathbf{l}}_M^\tau$ and $\hat{\mathbf{l}}_E^\tau$. With this, we can already evaluate the momentum-dependent part in the initial and final states of the amplitude. We obtain

$$\langle \mathbf{k}^{'}_{\mathscr{N}}; \mathbf{p}', j_\chi, M_\chi | \, \hat{\mathbf{l}} \left[\mathbf{q}, \mathbf{v}^{\perp}_{\mathscr{N}}, \hat{\mathbf{S}}_\chi \right] | \mathbf{k}_{\mathscr{N}}; \mathbf{p}, j_\chi, M_\chi \rangle \; = \; e^{-i\mathbf{q}\cdot\mathbf{r}} (2\pi)^3 \delta \left(\mathbf{k}'_{\mathscr{N}} + \mathbf{p}' - \mathbf{k}_{\mathscr{N}} - \mathbf{p} \right) \langle \hat{\mathbf{l}} \rangle . \tag{3.21}$$

Then, the matrix element writes

$$\begin{aligned} i\mathcal{M}_{NR} \; = \; & \langle J, M_J, T, M_T | \sum_{\tau=0}^{1} \Bigg[\langle \hat{l}_0^\tau \rangle \sum_{a=1}^{A} e^{-i\mathbf{q}\cdot\tilde{\mathbf{r}}_a} \\ & + \langle \hat{l}_{0A}^\tau \rangle \sum_{a=1}^{A} \frac{1}{2m_N} \left(i \overleftarrow{\nabla}_{\tilde{\mathbf{r}}_a} \cdot \sigma(a) \, e^{-i\mathbf{q}\cdot\tilde{\mathbf{r}}_a} \; - \; i e^{-i\mathbf{q}\cdot\tilde{\mathbf{r}}_a} \, \sigma(a) \cdot \overrightarrow{\nabla}_{\tilde{\mathbf{r}}_a} \right) \\ & + \langle \hat{\mathbf{l}}_5^\tau \rangle \cdot \sum_{a=1}^{A} \sigma(a) \, e^{-i\mathbf{q}\cdot\tilde{\mathbf{r}}_a} \\ & + \langle \hat{\mathbf{l}}_M^\tau \rangle \cdot \sum_{a=1}^{A} \frac{1}{2m_N} \left(i \overleftarrow{\nabla}_{\tilde{\mathbf{r}}_a} \, e^{-i\mathbf{q}\cdot\tilde{\mathbf{r}}_a} \; - \; i e^{-i\mathbf{q}\cdot\tilde{\mathbf{r}}_a} \, \overrightarrow{\nabla}_{\tilde{\mathbf{r}}_a} \right) \\ & + \langle \hat{\mathbf{l}}_E^\tau \rangle \cdot \sum_{a=1}^{A} \frac{1}{2m_N} \left(\overleftarrow{\nabla}_{\tilde{\mathbf{r}}_a} \times \sigma(a) \, e^{-i\mathbf{q}\cdot\tilde{\mathbf{r}}_a} \; + \; e^{-i\mathbf{q}\cdot\tilde{\mathbf{r}}_a} \, \sigma(a) \times \overrightarrow{\nabla}_{\tilde{\mathbf{r}}_a} \right) \Bigg] \\ & \cdot t^{\tau,a} \, | J, M_J, T, M_T \rangle \, . \end{aligned} \tag{3.22}$$

Apart from a term providing information about the scattering kinematics and on the dark matter-nucleon coupling strength, each term in Eq. (3.22) contains a factor given by the nuclear matrix element. In order to evaluate this contribution, we perform a multipole expansion of the nuclear charges and currents using the identities

$$
\begin{aligned}
e^{i\mathbf{q}\cdot\mathbf{r}} &= \sum_{L=0}^{\infty} \sqrt{4\pi(2L+1)}\, i^L j_L(qr_i)\, Y_{L0}(\Omega_{\mathbf{r}_i}) \\
e^{i\mathbf{q}\cdot\mathbf{r}}\,\mathbf{e}_0 &= \sum_{L=0}^{\infty} \sqrt{4\pi(2L+1)}\, i^{L-1} \frac{\vec{\nabla}}{q}\, j_L(qr_i)\, Y_{L0}(\Omega_{\mathbf{r}_i}) \\
e^{i\mathbf{q}\cdot\mathbf{r}}\,\mathbf{e}_\lambda &= \sum_{L=0}^{\infty} \sqrt{4\pi(2L+1)}\, i^{L-2} \left[\lambda j_L(qr_i)\, \mathbf{Y}^{\lambda}_{LL1}(\Omega_{\mathbf{r}_i}) + \frac{\vec{\nabla}_{\mathbf{r}_i}}{q} \times j_L(qr_i)\, \mathbf{Y}^{\lambda}_{LL1}(\Omega_{\mathbf{r}_i}) \right], \\
&\qquad \lambda = \pm 1
\end{aligned}
\tag{3.23}
$$

and

$$
\mathbf{A} = \sum_{\lambda=0,\pm1} (\mathbf{A}\cdot\mathbf{e}_\lambda)\, \mathbf{e}^{\dagger}_{\lambda}. \tag{3.24}
$$

with the spherical unit vector basis $\mathbf{e}_\lambda$ with z-axis along $\mathbf{q}$. Using Clebsch-Gordon coefficients and scalar spherical harmonics, we write the vector spherical harmonics in Eq. (3.23) as

$$
\mathbf{Y}^{M}_{LL\prime1}(\Omega_{\mathbf{r}_a}) = \sum_{m\lambda} \langle L\prime m 1 \lambda | L\prime 1 L M \rangle Y_{L\prime m}(\Omega_{\mathbf{r}_a})\, \mathbf{e}_\lambda, \tag{3.25}
$$

fulfilling $\mathbf{Y}^{\lambda\dagger}_{LL\prime1} = -(-1)^{\lambda}\mathbf{Y}^{-\lambda}_{LL\prime1}$.

Further, we assume that nuclear ground states are eigenstates of P and CP and therefore, only multipoles that transform evenly-evenly und P and CP contribute to $|\langle f|\, H\, |i\rangle|^2$. There are six nuclear response operators obeying this condition, which read

$$
\begin{aligned}
M_{LM;\tau}(q) &= \sum_{a=1}^{A} M_{LM}\left(q\tilde{\mathbf{r}}_a\right) t^{\tau}_{(a)} \\
\Sigma'_{LM;\tau}(q) &= -i\sum_{a=1}^{A}\left[\frac{1}{q}\overrightarrow{\nabla}_{\tilde{\mathbf{r}}_a} \times \vec{M}^{M}_{LL}\left(q\tilde{\mathbf{r}}_a\right)\right]\cdot \sigma(a) t^{\tau}_{(a)} \\
\Sigma''_{LM;\tau}(q) &= \sum_{a=1}^{A}\left[\frac{1}{q}\overrightarrow{\nabla}_{\tilde{\mathbf{r}}_a} M_{LM}\left(q\tilde{\mathbf{r}}_a\right)\right]\cdot \sigma(a) t^{\tau}_{(a)} \\
\Delta_{LM;\tau}(q) &= \sum_{a=1}^{A}\mathbf{M}^{M}_{LL}\left(q\tilde{\mathbf{r}}_a\right)\cdot\frac{1}{q}\overrightarrow{\nabla}_{\tilde{\mathbf{r}}_a} t^{\tau}_{(a)} \\
\tilde{\Phi}'_{LM;\tau}(q) &= \sum_{a=1}^{A}\left[\left(\frac{1}{q}\overrightarrow{\nabla}_{\tilde{\mathbf{r}}_a}\times\mathbf{M}^{M}_{LL}\left(q\tilde{\mathbf{r}}_a\right)\right)\cdot\left(\sigma(a)\times\frac{1}{q}\overrightarrow{\nabla}_{\tilde{\mathbf{r}}_a}\right)+\frac{1}{2}\mathbf{M}^{M}_{LL}\left(q\tilde{\mathbf{r}}_a\right)\cdot\sigma(i)\right] t^{\tau}_{(a)} \\
\Phi''_{LM;\tau}(q) &= i\sum_{a=1}^{A}\left(\frac{1}{q}\overrightarrow{\nabla}_{\tilde{\mathbf{r}}_a} M_{LM}\left(q\tilde{\mathbf{r}}_a\right)\right)\cdot\left(\sigma(a)\times\frac{1}{q}\overrightarrow{\nabla}_{\tilde{\mathbf{r}}_a}\right) t^{\tau}_{(a)}.
\end{aligned}
\tag{3.26}
$$

It further turns out that all terms related to $\hat{\mathbf{l}}^{\tau}_{0A}$ do not contribute [142]. Apart from this, the remaining charge and currents induce the following responses:

charge/current	response
$\hat{l}^{\tau}_{0}$	M
$\hat{\mathbf{l}}^{\tau}_{5}$	Σ', Σ''
$\hat{\mathbf{l}}^{\tau}_{M}$	Δ
$\hat{\mathbf{l}}^{\tau}_{E}$	$\tilde{\Phi}'$, Φ''

It is important to mention that also the interference terms $\Phi'' M$ and $\Delta\Sigma'$ arise.

In order to obtain the transition probability, we square the transition amplitude, sum over final spins and average over initial spins. This finally yields

$$
\begin{aligned}
P_{\rm tot}\left(w(r)^2, q^2\right) &= \frac{1}{2j\chi + 1}\frac{1}{2J+1}\sum_{\rm spins}|\mathcal{M}_{NR}|^2 \\
&= \frac{4\pi}{2J+1}\sum_{\tau=0}^{1}\sum_{\tau'=0}^{1}\Bigg\{\Bigg[R_M^{\tau\tau'}\left(v_T^{\perp 2}, \frac{q^2}{m_N^2}\right)W_M^{\tau\tau'}(y) \\
&\quad + R_{\Sigma''}^{\tau\tau'}\left(v_T^{\perp 2}, \frac{q^2}{m_N^2}\right)W_{\Sigma''}^{\tau\tau'}(y) + R_{\Sigma'}^{\tau\tau'}\left(v_T^{\perp 2}, \frac{q^2}{m_N^2}\right)W_{\Sigma'}^{\tau\tau'}(y)\Bigg] \\
&\quad + \frac{q^2}{m_N^2}\Bigg[R_{\Phi''}^{\tau\tau'}\left(v_T^{\perp 2}, \frac{q^2}{m_N^2}\right)W_{\Phi''}^{\tau\tau'}(y) + R_{\Phi''M}^{\tau\tau'}\left(v_T^{\perp 2}, \frac{q^2}{m_N^2}\right)W_{\Phi''M}^{\tau\tau'}(y) \\
&\quad + R_{\tilde{\Phi}'}^{\tau\tau'}\left(v_T^{\perp 2}, \frac{q^2}{m_N^2}\right)W_{\tilde{\Phi}'}^{\tau\tau'}(y) + R_{\Delta}^{\tau\tau'}\left(v_T^{\perp 2}, \frac{q^2}{m_N^2}\right)W_{\Delta}^{\tau\tau'}(y) \\
&\quad + R_{\Delta\Sigma'}^{\tau\tau'}\left(v_T^{\perp 2}, \frac{q^2}{m_N^2}\right)W_{\Delta\Sigma'}^{\tau\tau'}(y)\Bigg]\Bigg\},
\end{aligned}
\tag{3.27}
$$

where $R_k^{\tau\tau'}$ ($W_k^{\tau\tau'}$) are the dark matter (nuclear) response functions. The dark matter response functions read [144]

$$
\begin{aligned}
R_M^{\tau\tau'}\left(v_T^{\perp 2}, \frac{q^2}{m_N^2}\right) &= c_1^\tau c_1^{\tau'} + \frac{j_\chi(j_\chi+1)}{3}\left[\frac{q^2}{m_N^2}\mathbf{v}_T^{\perp 2}c_5^\tau c_5^{\tau'} + \mathbf{v}_T^{\perp 2}c_8^\tau c_8^{\tau'}\frac{q^2}{m_N^2}c_{11}^\tau c_{11}^{\tau'}\right], \\
R_{\Phi''}^{\tau\tau'}\left(v_T^{\perp 2}, \frac{q^2}{m_N^2}\right) &= \frac{q^2}{4m_N^2}c_3^\tau c_3^{\tau'} + \frac{j_\chi(j_\chi+1)}{12}\left(c_{12}^\tau - \frac{q^2}{m_N^2}c_{15}^\tau\right)\left(c_{12}^\tau - \frac{q^2}{m_N^2}c_{15}^{\tau'}\right), \\
R_{\Phi''M}^{\tau\tau'}\left(v_T^{\perp 2}, \frac{q^2}{m_N^2}\right) &= c_3^\tau c_1^{\tau'} + \frac{j_\chi(j_\chi+1)}{3}\left(c_{12}^\tau - \frac{q^2}{m_N^2}c_{15}^\tau\right)c_{11}^{\tau'}, \\
R_{\tilde{\Phi}'}^{\tau\tau'}\left(v_T^{\perp 2}, \frac{q^2}{m_N^2}\right) &= \frac{j_\chi(j_\chi+1)}{12}\left[c_{12}^\tau c_{12}^{\tau'} + \frac{q^2}{m_N^2}c_{13}^\tau c_{13}^{\tau'}\right], \\
R_{\Sigma''}^{\tau\tau'}\left(v_T^{\perp 2}, \frac{q^2}{m_N^2}\right) &= \frac{q^2}{4m_N^2}c_{10}^\tau c_{10}^{\tau'} + \frac{j_\chi(j_\chi+1)}{12}\cdot \\
&\quad \left[c_4^\tau c_4^{\tau'} + \frac{q^2}{m_N^2}\left(c_4^\tau c_6^{\tau'} + c_6^\tau c_4^{\tau'}\right) + \frac{q^4}{m_N^4}c_6^\tau c_6^{\tau'} + \mathbf{v}_T^{\perp 2}c_{12}^\tau c_{12}^{\tau'} + \frac{q^2}{m_N^2}\mathbf{v}_T^{\perp 2}c_{13}^\tau c_{13}^{\tau'}\right], \\
R_{\Delta}^{\tau\tau'}\left(v_T^{\perp 2}, \frac{q^2}{m_N^2}\right) &= \frac{j_\chi(j_\chi+1)}{3}\left[\frac{q^2}{m_N^2}c_5^\tau c_5^{\tau'} + c_8^\tau c_8^{\tau'}\right], \\
R_{\Delta\Sigma'}^{\tau\tau'}\left(v_T^{\perp 2}, \frac{q^2}{m_N^2}\right) &= \frac{j_\chi(j_\chi+1)}{3}\left[c_5^\tau c_4^{\tau'} - c_8^\tau c_9^{\tau'}\right].
\end{aligned}
\tag{3.28}
$$

The nuclear response functions, on the other hand, have to be calculated numerically for each isotope within a nuclear model. In Appendix A, we reproduce for completeness the nuclear form factors calculated in [142, 144] for the nuclei relevant for this thesis. Finally, the differential scattering cross-section of a dark matter particle off a nucleus $\mathscr{N}$ can be calculated from the Hamiltonian. The result is

$$\frac{\mathrm{d}\sigma_{\mathscr{N}}}{\mathrm{d}E}\left(w(r)^2, q^2\right) = \frac{m_{\mathscr{N}}}{2\pi w(r)^2} P_{\mathrm{tot}}\left(w(r)^2, q^2\right). \tag{3.29}$$

Since the interaction rate of dark matter particles with nucleons depends linearly on the differential cross-section, and therefore quadratically on the coupling constants $\mathbf{c}$, we can express the number of expected signal events for experiment ε as [4, 145, 146]

$$N_{\varepsilon}^{\mathrm{sig}}(\mathbf{c}) = \mathbf{c}^T \mathbb{N}_{\varepsilon} \mathbf{c}, \tag{3.30}$$

where $\mathbb{N}$” is a 28×28 real symmetric matrix corresponding to experiment ε. For a direct detection experiment, such as XENON1T and PICO-60, $\mathbb{N}_{\varepsilon}$ depends on the detector composition, exposure and dark matter local density, velocity distribution and mass. For a neutrino telescope, such as IceCube, it depends on the solar model, and the dark matter local density, velocity distribution, mass, annihilation channel and rate, and the neutrino propagation and flavor conversion inside the Sun.

From the dark matter response functions we can figure out which nuclear responses the couplings c_i are sensitive to and what is the corresponding momentum and velocity dependence. In Tab. 3.2, we summarize this information. Firstly, note that while in interactions induced by the M, Σ', Σ'', Δ or Φ'' CP is conserved, it is violated for $\tilde{\Phi}'$. Secondly, note that responses depending on $\mathbf{v}_T^\perp$ are strongly suppressed due to the small dark matter velocities. Therefore they do not significantly affect the results, while responses depending on the momentum transfer or being independent on momentum transfer and velocity do.

c_i	$R^{\tau\tau'}$	c_i	$R^{\tau\tau'}$
c_1	$M\left(q^0\right)$	c_9	$\Sigma'\left(q^2\right)$
c_3	$\Phi''\left(q^4\right)$, $\Sigma'\left(q^2\right)$, $\Sigma'\left(q^2, \left(\mathbf{v}_T^\perp\right)^2\right)$	c_{10}	$\Sigma''\left(q^2\right)$
c_4	$\Sigma''\left(q^0\right)$, $\Sigma'\left(q^0\right)$	c_{11}	$M\left(q^2\right)$
c_5	$\Delta\left(q^4\right)$, $M\left(q^2, \left(\mathbf{v}_T^\perp\right)^5\right)$	c_{12}	$\Phi''\left(q^2\right)$, $\tilde{\Phi}'\left(q^2\right)$, $\Sigma''\left(q^0, \left(\mathbf{v}_T^\perp\right)^2\right)$, $\Sigma'\left(q^0, \left(\mathbf{v}_T^\perp\right)^2\right)$
c_6	$\Sigma''\left(q^4\right)$	c_{13}	$\tilde{\Phi}\left(q^4\right)$, $\Sigma''\left(q^2, \left(\mathbf{v}_T^\perp\right)^2\right)$
c_7	$\Sigma'\left(q^0, \left(\mathbf{v}_T^\perp\right)^2\right)$	c_{14}	$\Sigma'\left(q^2, \left(\mathbf{v}_T^\perp\right)^2\right)$
c_8	$\Delta\left(q^2\right)$, $M\left(q^0, \left(\mathbf{v}_T^\perp\right)^2\right)$	c_{15}	$\Phi''\left(q^6\right)$, $\Sigma'\left(q^4, \left(\mathbf{v}_T^\perp\right)^2\right)$

Table 3.2: The coupling constants c_i for $i = 1, 3, 4, ..., 15$, the related response functions and the dependence on the momentum transfer q and transverse velocity $\mathbf{v}_T^\perp$.

In the following, we briefly explain the characteristics of the responses and *highlight* the required property of the nucleus to be favored in a corresponding interaction. This allows a rough forecast whether a certain element is appropriate to constrain the parameter space strongly or not. Further, we comment on the expected shape of the allowed parameter space in two dimensions, *i.e.* in the case of interference among the proton and neutron component. In most cases, it is a closed region whose eccentricity depends on the nucleus species. There are two special cases in which we expect something different:

- **Isoscalar strip**: For isoscalar elements, *i.e.* elements with the same number of protons and neutrons, we do not expect to get a closed region, but a strip with infinite elongation in the isovector direction.

- **Proton strip**: This very special case applies to elements consisting only of protons, *i.e.* the only element that is affected is ^{1}H. Since it does not contain neutrons, the neutron component cannot be constrained by ^{1}H. Therefore, we also expect here to have an infinite strip, perfectly aligned with the c_i^n-axis.

M - response

For small momentum transfers, the M-response measures the mass number A. Therefore, dark matter interactions with *heavier elements are favored.*

The orientation of the allowed parameter space

For the M-response, the orientation of the allowed parameter space can be determined easily. We start with the dependence of R, the corresponding rate, on the couplings to protons and neutrons, c_i^p and c_i^n, respectively, and the number of nucleons A and protons Z:

$$R \propto \left[c_i^p Z + (A-Z)\, c_i^n\right]. \tag{3.31}$$

To determine the orientation of the allowed parameter spaces, we first solve Eq. (3.31) for c_i^p, which gives us

$$c_i^p \propto \frac{R}{Z + (A-Z)\,\frac{c_i^n}{c_i^p}}. \tag{3.32}$$

Since we aim to obtain the maximum for c_i^p, the denominator on the RHS needs to be small, *i.e.* we equate it with zero. Solving

$$Z + (A-Z)\frac{c_i^n}{c_i^p} = 0 \tag{3.33}$$

for c_i^n/c_i^p, which is the slope, we get

$$\frac{c_i^n}{c_i^p} = \frac{Z}{Z - A}. \tag{3.34}$$

Σ' - and Σ'' - responses

Σ' (Σ'') measure the transverse (longitudinal) component of the nucleon spin. Therefore, elements with *unpaired protons or neutrons are favored.*

Δ - response

Elements with *unpaired protons or neutrons in a non-s-shell orbit are favored.*

Φ'' - response

At zero-momentum transfer it can be related to $(\mathbf{L} \cdot \mathbf{S})_{n,p}$. Due to that, *heavy elements are favored with orbits of large angular momentum which are not fully occupied.*

$\tilde{\Phi}'$ - response

This response is *only relevant for elements with nuclear spin J larger than 1/2.* Regarding Tab. C.1 , in our case it is only relevant for ^{14}N ($J = 1$), ^{23}Na ($J = 3/2$) and ^{27}Al ($J = 5/2$).

3.2 The effective field theory: From quarks to nucleons

In dark matter scatterings with ordinary matter, the involved energies are usually very low. For this reason it is common to consider dark matter to interact with the nucleons or nuclei - the degrees of freedom in the non-relativistic theory - instead of the quarks and gluons, which are the degrees of freedom in the high-energy theory. In order to describe the interactions of dark matter particles with detector material and to determine limits on the coupling strength between dark matter and ordinary matter, we choose the non-relativistic approach. However, dark matter models are formulated in terms of operators that involve quarks and gluons.

In this section, we review how to convert interaction operators resulting from the high-energy theory into the operators appearing in the non-relativistic theory along the lines of [147]. In our calculations we consider dark matter particles with spin up to 1/2, *i.e.* dark matter could either be fermionic or scalar. Therefore we distinguish between the operators arising for fermionic and scalar dark matter in the following two sections.

3.2.1 Fermionic dark matter

In the theory in which fermionic dark matter χ interacts with a quark q, the interaction operators are of dimension six and read

$$\begin{aligned}
\hat{\mathcal{O}}_1^q &= \bar{\chi}\chi\,\bar{q}q, & \hat{\mathcal{O}}_2^q &= \bar{\chi}\,i\gamma^5\,\chi\,\bar{q}q,\\
\hat{\mathcal{O}}_3^q &= \bar{\chi}\chi\,\bar{q}\,i\gamma^5\,q, & \hat{\mathcal{O}}_4^q &= \bar{\chi}\,i\gamma^5\,\chi\,\bar{q}\,i\gamma^5\,q,\\
\hat{\mathcal{O}}_5^q &= \bar{\chi}\gamma^\mu\chi\,\bar{q}\,\gamma_\mu\,q, & \hat{\mathcal{O}}_6^q &= \bar{\chi}\,\gamma^\mu\gamma^5\,\chi\,\bar{q}\,\gamma_\mu\,q,\\
\hat{\mathcal{O}}_7^q &= \bar{\chi}\gamma^\mu\chi\,\bar{q}\,\gamma_\mu\gamma^5\,q, & \hat{\mathcal{O}}_8^q &= \bar{\chi}\,\gamma^\mu\gamma^5\,\chi\,\bar{q}\,\gamma_\mu\gamma^5\,q,\\
\hat{\mathcal{O}}_9^q &= \bar{\chi}\,\sigma^{\mu\nu}\,\chi\,\bar{q}\,\sigma_{\mu\nu}\,q, & \hat{\mathcal{O}}_{10}^q &= \bar{\chi}\,i\sigma^{\mu\nu}\gamma^5\chi\,\bar{q}\,\sigma_{\mu\nu}\,q,
\end{aligned}$$

with $\sigma^{\mu\nu} = -\frac{i}{4}\left[\gamma^\mu\gamma^\nu - \gamma^\nu\gamma^\mu\right]$. For Majorana dark matter, the operators $\hat{\mathcal{O}}_5^q$, $\hat{\mathcal{O}}_7^q$, $\hat{\mathcal{O}}_9^q$ and $\hat{\mathcal{O}}_{10}^q$ identically vanish. Note that the operators

$$\bar{\chi}\,\sigma^{\mu\nu}\chi\,\bar{q}\,i\sigma_{\mu\nu}\gamma^5\,q \qquad \text{and} \qquad \bar{\chi}\,i\sigma^{\mu\nu}\gamma^5\chi\,\bar{q}\,i\sigma_{\mu\nu}\gamma^5\,q$$

are omitted in the list as they can be formed into $\hat{\mathcal{O}}_{10}^q$ and $-\hat{\mathcal{O}}_9^q$, respectively, using the identity $i\sigma^{\mu\nu}\gamma^5 = -\frac{1}{2}\varepsilon^{\mu\nu\rho\tau}\sigma_{\rho\tau}$.

Regarding high energies, a dark matter particle could also interact with a gluon field $G^a_{\mu\nu}$. The corresponding interaction operators are of dimension seven and read

$$\begin{aligned} \hat{\mathcal{O}}_1^g &= \tfrac{\alpha_s}{12\pi}\,\bar{\chi}\chi\,G^a_{\mu\nu}G^a_{\mu\nu} & \hat{\mathcal{O}}_2^g &= \tfrac{\alpha_s}{12\pi}\,\bar{\chi}\,i\gamma^5\,\chi\,G^a_{\mu\nu}G^a_{\mu\nu}, \\ \hat{\mathcal{O}}_1^g &= \tfrac{\alpha_s}{12\pi}\,\bar{\chi}\chi\,G^a_{\mu\nu}\tilde{G}^a_{\mu\nu}, & \hat{\mathcal{O}}_1^g &= \tfrac{\alpha_s}{12\pi}\,\bar{\chi}\,i\gamma^5\,\chi\,G^a_{\mu\nu}\tilde{G}^a_{\mu\nu}, \end{aligned}$$

where $\tilde{G}^a_{\mu\nu} \equiv \varepsilon^{\mu\nu\rho\sigma}G^a_{\mu\nu}$.

On the quark-gluon level, the effective Lagrangian reads

$$\mathcal{L}_{\text{eff}} = \sum_{i=1}^{10}\sum_q c_i^q\mathcal{O}_i^q + \sum_{i=1}^{4} c_i^g\mathcal{O}_i^g, \tag{3.35}$$

where c_i^q (c_i^g) is the coupling constant between dark matter and a quark (gluon) of dimension $[\text{mass}]^{-2}$ ($[\text{mass}]^{-3}$). The induced effective Lagrangian on nucleon level is

$$\mathcal{L}_{\text{eff}} = \sum_{i=1}^{10}\sum_{N=p,n} c_i^N\mathcal{O}_i^N. \tag{3.36}$$

Here, $\hat{\mathcal{O}}_i^N$ are

$$\begin{aligned} \hat{\mathcal{O}}_1^N &= \bar{\chi}\chi\,\bar{N}N, & \hat{\mathcal{O}}_2^N &= \bar{\chi}\,i\gamma^5\,\chi\,\bar{N}N, \\ \hat{\mathcal{O}}_3^N &= \bar{\chi}\chi\,\bar{N}\,i\gamma^5\,N, & \hat{\mathcal{O}}_4^N &= \bar{\chi}\,i\gamma^5\,\chi\,\bar{N}\,i\gamma^5\,N, \\ \hat{\mathcal{O}}_5^N &= \bar{\chi}\gamma^\mu\chi\,\bar{N}\,\gamma_\mu\,N, & \hat{\mathcal{O}}_6^N &= \bar{\chi}\,\gamma^\mu\gamma^5\,\chi\,\bar{N}\,\gamma_\mu\,N, \\ \hat{\mathcal{O}}_7^N &= \bar{\chi}\gamma^\mu\chi\,\bar{N}\,\gamma_\mu\gamma^5\,N, & \hat{\mathcal{O}}_8^N &= \bar{\chi}\,\gamma^\mu\gamma^5\,\chi\,\bar{N}\,\gamma_\mu\gamma^5\,N, \\ \hat{\mathcal{O}}_9^N &= \bar{\chi}\,\sigma^{\mu\nu}\,\chi\,\bar{N}\,\sigma_{\mu\nu}\,N, & \hat{\mathcal{O}}_{10}^N &= \bar{\chi}\,i\sigma^{\mu\nu}\gamma^5\chi\,\bar{N}\,\sigma_{\mu\nu}\,N. \end{aligned}$$

While the quark related operators contribute to all of the nucleon operators listed above, the gluon related operators only contribute to operators $\hat{\mathcal{O}}_1^N$, $\hat{\mathcal{O}}_2^N$, $\hat{\mathcal{O}}_3^N$ and $\hat{\mathcal{O}}_4^N$.

In order to relate the quark-gluon level with the nucleon-nucleus level, we evaluate the matrix elements $\langle \chi, N| \hat{\mathcal{O}}_i^N |\chi, N\rangle$ and write them in terms of $\hat{\mathcal{O}}_i^{\mathrm{NR}}$, the non-relativistic operators[2]. As a first step, we expand the solution of the Dirac equation in the non-relativistic limit,

$$u^s(p) = \begin{pmatrix} \sqrt{p^\mu \sigma_\mu}\, \xi^s \\ \sqrt{p^\mu \bar{\sigma}_\mu}\, \xi^s \end{pmatrix} = \frac{1}{\sqrt{4m}} \begin{pmatrix} (2m - \mathbf{p}\cdot\sigma)\, \xi^s \\ (2m + \mathbf{p}\cdot\sigma)\, \xi^s \end{pmatrix} + \mathcal{O}\left(\mathbf{p}^2\right), \tag{3.37}$$

with $\sigma^\mu = (\mathbb{1}, \sigma)$ and $\bar{\sigma} = (\mathbb{1}, -\sigma)$. This ingredient allows us to relate fermion bilinears and spin, momentum and velocity. We obtain

$$\bar{u}(p')u(p) \simeq 2m \tag{3.38}$$

$$\bar{u}(p')\, i\gamma^5\, u(p) \simeq 2i\mathbf{q}\cdot\mathbf{s} \tag{3.39}$$

$$\bar{u}(p')\, \gamma^\mu\, u(p) \simeq \begin{pmatrix} 2m \\ \mathbf{P} + 2i\mathbf{q}\times\mathbf{s} \end{pmatrix} \tag{3.40}$$

$$\bar{u}(p')\, \gamma^\mu\gamma^5\, u(p) \simeq \begin{pmatrix} 2\mathbf{P}\cdot\mathbf{s} \\ 4m\mathbf{s} \end{pmatrix} \tag{3.41}$$

$$\bar{u}(p')\, \sigma^{\mu\nu}\, u(p) \simeq \begin{pmatrix} 0 & i\mathbf{q} - 2\mathbf{P}\times\mathbf{s} \\ -i\mathbf{q} + 2\mathbf{P}\times\mathbf{s} & 4m\varepsilon_{ijk}s^k \end{pmatrix} \tag{3.42}$$

$$\bar{u}(p')\, i\sigma^{\mu\nu}\gamma^5\, u(p) \simeq \begin{pmatrix} 0 & -4m\mathbf{s} \\ 4m\mathbf{s} & i\varepsilon_{ijk}q_k - 2P_i s^j + 2P_J s^i \end{pmatrix}, \tag{3.43}$$

with $\mathbf{q} = \mathbf{p} - \mathbf{p}'$, $\mathbf{P} = \mathbf{p} + \mathbf{p}'$ and $\mathbf{s} \equiv \xi'^\dagger \frac{\sigma}{2} \xi$. Contracting the dark matter and nucleon bilinears and using $\frac{\mathbf{P}_\chi}{m_\chi} - \frac{\mathbf{P}_N}{m_N} = 2\mathbf{v}^\perp$, we obtain expressions that relate the operators of the relativistic and non-relativistic approach:

---

[2] In previous sections, we denote $\hat{\mathcal{O}}_i^{\mathrm{NR}}$ as $\hat{\mathcal{O}}_i$. Here, we explicitly keep the index NR in order to distinguish the corresponding operators from the several operators appearing in the relativistic approach.

$$\langle \mathcal{O}_1^N \rangle = \langle \mathcal{O}_5^N \rangle = 4m_\chi m_N \mathcal{O}_1^{\rm NR} \tag{3.44}$$

$$\langle \mathcal{O}_2^N \rangle = -4m_N \mathcal{O}_{11}^{\rm NR} \tag{3.45}$$

$$\langle \mathcal{O}_3^N \rangle = 4m_\chi \mathcal{O}_{10}^{\rm NR} \tag{3.46}$$

$$\langle \mathcal{O}_4^N \rangle = 4\mathcal{O}_6^{\rm NR} \tag{3.47}$$

$$\langle \mathcal{O}_6^N \rangle = 8m_\chi \left(m_N \mathcal{O}_8^{\rm NR} + \mathcal{O}_9^{\rm NR} \right) \tag{3.48}$$

$$\langle \mathcal{O}_7^N \rangle = 8m_N \left(-m_\chi \mathcal{O}_7^{\rm NR} + \mathcal{O}_9^{\rm NR} \right) \tag{3.49}$$

$$\langle \mathcal{O}_8^N \rangle = \frac{1}{2} \langle \mathcal{O}_9^N \rangle = -16 m_\chi m_N \mathcal{O}_4^{\rm NR} \tag{3.50}$$

$$\langle \mathcal{O}_{10}^N \rangle = 8 \left(m_\chi \mathcal{O}_{11}^{\rm NR} - m_N \mathcal{O}_{10}^{\rm NR} - 4 m_\chi m_N \mathcal{O}_{12}^{\rm NR} \right) \tag{3.51}$$

As one can see in Eqs. (3.44) and (3.50), the relativistic operators $\mathcal{O}_1^N$ and $\mathcal{O}_5^N$ coincide, and $\mathcal{O}_8^N$ can be expressed in terms of $\mathcal{O}_9^N$. In the context of direct detection this means that these interactions are indistinguishable, and so are the related bounds on the couplings.

3.2.2 Scalar dark matter

The interactions of scalar dark matter with a quark are described by the dimension-five operators

$$\hat{\mathcal{O}}_1^q = \phi^* \phi \, \bar{q} q, \qquad \hat{\mathcal{O}}_2^q = \phi^* \phi \, \bar{q} \, i\gamma^5 \, q$$

and the dimension-six operators

$$\hat{\mathcal{O}}_3^q = i\partial_\mu (\phi^* \phi) \, \bar{q} \, \gamma^\mu \, q, \qquad \hat{\mathcal{O}}_4^q = i\partial_\mu (\phi^* \phi) \, \bar{q} \, \gamma^\mu \gamma^5 \, q,$$

where the operators $\hat{\mathcal{O}}_3^q$ and $\hat{\mathcal{O}}_4^q$ are zero for a real scalar field ϕ. Apparently, the operators $\partial_\mu \left(\phi^* \phi\right) \, \bar{q} \, \gamma^\mu \, q$ and $\partial_\mu \left(\phi^* \phi\right) \, \bar{q} \, \gamma^\mu \gamma^5 \, q$ are missing above. The former does not contribute to the scattering process in which quarks are external. This becomes apparent after integration by parts where this is proportional to the divergence of the conserved current $\bar{q} \, \gamma^\mu \, q$ which vanishes after applying the equations of motion. The latter reduces to $2m_q \phi^* \phi \, i\gamma^5 q$ after integration by parts and applying the equations of motion, and is identical to $\hat{\mathcal{O}}_2^q$.

We do not take into account the dimension-six operators

$$\phi^*\phi\,\bar{q}\,i\overleftrightarrow{D}\,q, \qquad\qquad \phi^*\phi\,\bar{q}\,i\overleftrightarrow{D}\gamma^5\,q,$$

with the 'hermitianized' quark covariant derivative $\overleftrightarrow{D}_\mu = \frac{1}{2}\overleftrightarrow{\partial}_\mu - ieQ_qA_\mu - ig_sT_q^a g_\mu^a$.

For interactions of dark matter particles with gluons, the most relevant gauge-invariant operators are

$$\hat{\mathcal{O}}_1^g = \tfrac{\alpha}{12\pi}\phi^*\phi\,G^a_{\mu\nu}G^a_{\mu\nu}, \qquad\qquad \hat{\mathcal{O}}_2^g = \tfrac{\alpha}{8\pi}\phi^*\phi\,G^a_{\mu\nu}\tilde{G}^a_{\mu\nu},$$

which have dimension six. The numerical factors were chosen for convenience.

For scalar dark matter, the effective Lagrangian at the quark-gluon level reads

$$\mathcal{L}_{\text{eff}} = \sum_{i=1}^{4}\sum_{q} c_i^q\mathcal{O}_i^q + \sum_{i=1}^{4} c_i^g\mathcal{O}_i^g, \tag{3.52}$$

where c_i^q (c_i^g) is the coupling constant between dark matter and a quark (gluon) of dimension $[\text{mass}]^{-1}$ ($[\text{mass}]^{-3}$) for $k = 1, 2$ and $[\text{mass}]^{-2}$ ($[\text{mass}]^{-3}$) for $k = 3, 4$. The induced effective Lagrangian at nucleon level is

$$\mathcal{L}_{\text{eff}} = \sum_{i=1}^{4}\sum_{N=p,n} c_i^N\mathcal{O}_i^N, \tag{3.53}$$

where $\mathcal{O}_k^N$ are

$$\begin{aligned} \hat{\mathcal{O}}_1^N &= \phi^*\phi\,\bar{N}N, & \hat{\mathcal{O}}_2^N &= \phi^*\phi\,\bar{N}\,i\gamma^5\,N, \\ \hat{\mathcal{O}}_3^N &= i\partial_\mu\left(\phi^*\phi\right)\,\bar{N}\,\gamma^\mu N, & \hat{\mathcal{O}}_4^N &= i\partial_\mu\left(\phi^*\phi\right)\,\bar{N}\,\gamma^\mu\gamma^5 N. \end{aligned}$$

The relations between the relativistic and non-relativistic operators read

$$\langle \mathcal{O}_1^N \rangle = 2m_N \mathcal{O}_1^{\rm NR}, \tag{3.54}$$

$$\langle \mathcal{O}_2^N \rangle = 2\mathcal{O}_{10}^{\rm NR}, \tag{3.55}$$

$$\langle \mathcal{O}_3^N \rangle = 4m_\chi m_N \mathcal{O}_1^{\rm NR}, \tag{3.56}$$

$$\langle \mathcal{O}_4^N \rangle = -8m_\chi m_N \mathcal{O}_7^{\rm NR}. \tag{3.57}$$

4

Cross-section limits for a single experiment

In order to reduce the number of free parameters in the analysis of the dark matter-nucleon interactions when casting experimental data into limits on the dark matter-nucleon coupling strength (see *e.g.* [13, 24, 25]), it is common practice to consider a purely isoscalar interaction between dark matter particles and nucleons, and only one single interaction at a time. Since this assumption does not necessarily coincide with theoretical models, experimental results and model predictions cannot be straightforwardly compared. For the latter in general it is expected a non-zero coupling of dark matter to both the isoscalar and isovector component, as well as more than one operator, possibly interfering with one another (see *e.g.* the models predicting isospin violation [14–18, 20–23]).

In this chapter, we develop a methodology to determine model-independent limits on the dark matter-nucleon coupling strengths for a single experiment. We show the limits using data provided by XENON1T [24], PICO-60 [25, 26] and IceCube [13].

4.1 Developing a method for a single experiment

We consider experiment ε with the number of expected background events $N_\varepsilon^{\text{back}}$, number of observed events $N_\varepsilon^{\text{obs}}$ and number of expected signal events $N_\varepsilon^{\text{sig}}(\mathbf{c}\,)$. The χ^2 distribution in terms of the experimental likelihood reads [148, 149]

$$\chi^2_\varepsilon(\mathbf{c}) \; = \; -2\log\mathcal{L}\left(N^{\mathrm{sig}}_\varepsilon(\mathbf{c})\right). \tag{4.1}$$

Since the experiments we consider here are counting experiments, we choose a poissonian likelihood such that the general expression for $\mathcal{L}\left(N^{\mathrm{sig}}_\varepsilon(\mathbf{c})\right)$ has the form

$$\mathcal{L}\left(N^{\mathrm{sig}}_\varepsilon(\mathbf{c})\right) \; = \; \frac{\left(N^{\mathrm{sig}}_\varepsilon(\mathbf{c}) \, + \, N^{\mathrm{back}}_\varepsilon\right)^{N^{\mathrm{obs}}_\varepsilon}}{N^{\mathrm{obs}}_\varepsilon!} \, e^{-\left(N^{\mathrm{sig}}_\varepsilon(\mathbf{c}) + N^{\mathrm{back}}_\varepsilon\right)}. \tag{4.2}$$

For the choice of experiments in this work, a valid approximation of Eq. (4.1) using Eq. (4.2) is given by the quadratic function

$$\chi^2_\varepsilon(\mathbf{c}) \; \simeq \; a_\varepsilon\left(N^{\mathrm{sig}}_\varepsilon(\mathbf{c})\right)^2 \, + \, b_\varepsilon N^{\mathrm{sig}}_\varepsilon(\mathbf{c}) \, + \, c_\varepsilon. \tag{4.3}$$

The coefficients a_ε, b_ε and c_ε are listed in Tab. 4.1.

experiment	a_ε	b_ε	c_ε
XENON1T	0.06713	−1.072	8.707
PICO-60 (1st bin)	0.29010	−1.728	5.440
PICO-60 (2nd bin)	0	2	0
IceCube	0.001046	0.01092	8.696
DeepCore	0.002376	−0.06191	8.298

Table 4.1: Coefficients a_ε, b_ε and c_ε of the quadratic approximation in Eq. (4.3) for XENON1T, first and second bin of PICO-60, IceCube and DeepCore.

The proper choice of the quantity $\Delta\chi^2_\varepsilon \; = \; \chi^2_\varepsilon \, - \, \chi^2_{\varepsilon,\mathrm{min}} \; \leq \; n_0$ is crucial to determine the allowed region of parameter space, for which we obtain $\chi^2_{\varepsilon,\mathrm{min}}$ by minimizing χ^2_ε with respect to the number of signal events. This yields

$$\chi^2_{\varepsilon,\mathrm{min}} \; = \; c_\varepsilon \, - \, \frac{b^2_\varepsilon}{4a_\varepsilon}. \tag{4.4}$$

For 90% C.L. and if the experiment has observed a non-zero number of events, such as XENON1T, PICO-60 (1st bin), IceCube and DeepCore, the difference in dimensionality between χ^2_ε and $\chi^2_{\varepsilon,\mathrm{min}}$ is equal to one. In this case, $n_0 \; = \; 2.71$ according to the χ^2-distribution table. For 90% C.L. and if the number of observed events for an experiment is zero, such as for PICO-60 (2nd bin), the difference in dimensionality between χ^2_ε and $\chi^2_{\varepsilon,\mathrm{min}}$ is equal to two. In this case, we find $n_0 = 4.6$.

The χ^2-formalism is typically used in the literature under the assumption that one has only one single operator at a time and equal coupling to protons and neutrons (see *e.g.* [13, 24, 25]). This assumption reduces the number of free parameters in the analysis, however, this prohibits a straightforward confrontation of experimental limits and theoretical predictions of specific dark matter models, since the latter typically predict more than a single effective field theory operator. Having more than one interaction at a time may cause interference among each other, resulting for example in dark matter models in which the dark matter particle interacts with protons and neutrons (or equivalently with the isoscalar and isovector component) with different strengths. In Fig. 4.1, we schematically show the allowed parameter space for experiment ε when considering two interactions, c_α and c_β, at a time[1]. Under the common assumption that only one coupling, *e.g.* c_α is non-zero, we obtain the model-dependent limit $\max\{c_\alpha\}|_{c_\beta=0}$. Here, a wrong conclusion can be drawn if we consider for example a model that predicts certain values for the coupling strengths c_α and c_β, indicated by the red cross. Using the limit $\max\{c_\alpha\}|_{c_\beta=0}$ leads to the conclusion that the value for c_α predicted by the theoretical model is ruled out. However, this point is actually allowed by the experiment as it is contained in the allowed region (blue). This makes clear that using the limit $\max\{c_\alpha\}|_{c_\beta=0}$, the coupling strengths indicated by the red cross would be ruled out erroneously. In order to rule out couplings in a model independent way, we consider instead the model-independent limit $c^{\max} = \max\{c_\alpha\}$; if a model predicts a coupling strength beyond this limit, it cannot lie inside the blue region, which leads to the conclusion that it is for sure ruled out.

In order to determine $c_\alpha^{\max}$, we construct the Lagrangian

$$L = c_\alpha - \lambda \left[\chi^2_\varepsilon(\mathbf{c}) - \chi^2_{\varepsilon,\mathrm{min}} - n_0\right], \tag{4.5}$$

with the Lagrange multiplier λ enforcing the constraint that the coupling strengths saturate the limits at 90% C.L. Extremizing the Lagrangian with

---

[1] The coupling constant c_α (c_β) could for example represent the standard spin-independent interaction strength between a dark matter particle and a proton (neutron).

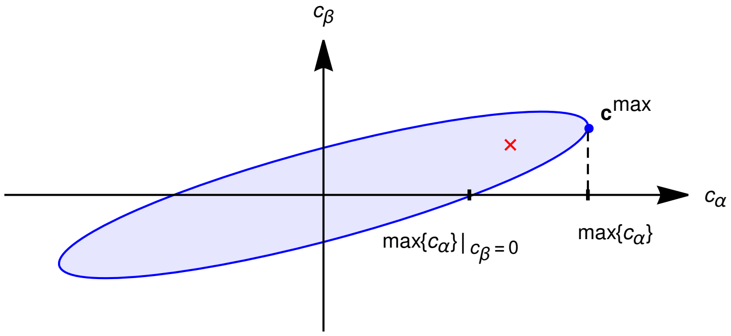

Figure 4.1: Allowed parameter space spanned by the couplings c_α and c_β. Assuming that the coupling $c_\beta = 0$, the resulting limit is $\max\{c_\alpha\}|_{c_\beta=0}$. However, this excludes for example the point marked by a red cross, although it is allowed by data. With the model-independent limit $\max\{c_\alpha\}$ we can safely exclude the parameter space beyond at a certain C.L.

respect to c_β and λ gives

$$\left.\frac{\partial L}{\partial c_\beta}\right|_{\mathbf{c}=\mathbf{c}^{\max}} = \delta_{\beta\alpha} - 2\lambda\left[2a_\varepsilon N_\varepsilon^{\text{sig}}\left(\mathbf{c}^{\max}\right) + b_\varepsilon\right]\left(\mathbb{N}_\varepsilon\right)_{\beta\gamma} c_\gamma^{\max} = 0, \tag{4.6}$$

$$\left.\frac{\partial L}{d\lambda}\right|_{\mathbf{c}=\mathbf{c}^{\max}} = -\left[a_\varepsilon\left(N_\varepsilon^{\text{sig}}\left(\mathbf{c}^{\max}\right)\right)^2 + b_\varepsilon N_\varepsilon^{\text{sig}}\left(\mathbf{c}^{\max}\right) + c_\varepsilon - \chi^2_{\varepsilon,\min} - 2.71\right] = 0. \tag{4.7}$$

Note that we used the approximate function for χ^2_ε, Eq. (4.3). Using Eq. (4.6), we obtain

$$c_\beta^{\max} = \frac{1}{2\lambda\left[2a_\varepsilon N_\varepsilon^{\text{sig}}\left(\mathbf{c}^{\max}\right) + b_\varepsilon\right]}\left(\mathbb{N}_\varepsilon^{-1}\right)_{\beta\alpha}. \tag{4.8}$$

Inserting this relation in Eq. (3.30), we obtain

$$N_\varepsilon^{\text{sig}}\left(\mathbf{c}^{\max}\right) = \frac{1}{4\lambda^2\left[2a_\varepsilon N_\varepsilon^{\text{sig}}\left(\mathbf{c}^{\max}\right) + b_\varepsilon\right]^2}\left(\mathbb{N}_\varepsilon^{-1}\right)_{\alpha\alpha}. \tag{4.9}$$

Finally, we use Eqs. (4.7) and (4.9) to determine λ and $N_\varepsilon^{\text{sig}}\left(\mathbf{c}^{\max}\right)$ which we substitute in Eq. (4.8) to obtain the expression for the model-independent upper limit

$$c_\alpha^{\max} = \sqrt{N_\varepsilon^{\text{sig}}\left(\mathbf{c}^{\max}\right)\left(\mathbb{N}_\varepsilon^{-1}\right)_{\alpha\alpha}}. \tag{4.10}$$

The transformation of the limits to another basis (such as from the proton-neutron basis to the isoscalar-isovector basis) can be done very easily. In the following, we denote quantities in the other basis with a tilde. Then, it follows that

$$\tilde{c}_{\alpha}^{\max} = \sqrt{N_{\varepsilon}^{\text{sig}}\left(\tilde{\mathbf{c}}^{\max}\right)\left(\tilde{\mathbb{N}}_{\varepsilon}^{-1}\right)_{\alpha\alpha}}. \tag{4.11}$$

For a quick determination of $\tilde{\mathbb{N}}_{\varepsilon}$, we use the transformation of the couplings

$$\tilde{\mathbf{c}} = \mathbb{T}\mathbf{c} \tag{4.12}$$

and the condition that the signal does not depend on the basis:

$$N_{\varepsilon}^{\text{sig}}(\mathbf{c}) = \mathbf{c}^{T}\mathbb{N}_{\varepsilon}\mathbf{c} = \tilde{\mathbf{c}}^{T}\tilde{\mathbb{N}}_{\varepsilon}\tilde{\mathbf{c}}. \tag{4.13}$$

It follows that

$$\tilde{\mathbb{N}}_{\varepsilon} = \left(\mathbb{T}^{\text{T}}\right)^{-1}\mathbb{N}_{\varepsilon}\mathbb{T}^{-1}. \tag{4.14}$$

If one considers only one operator, the transformation from the proton-neutron basis to the isoscalar-isovector basis can be carried out by the transformation matrix

$$\mathbb{T} = \begin{pmatrix} 1 & 1 \\ 1 & -1 \end{pmatrix}. \tag{4.15}$$

The corresponding transformation matrix for a set of i interaction operators would be a block-diagonal $2i \times 2i$-matrix with Eq. (4.15) on the diagonal.

4.2 Model-independent upper limits using XENON1T, PICO-60 and IceCube data

We apply the method presented above to derive model-independent upper limits on the coupling strengths of the 14 operators of the effective field theory at 90% C.L. assuming the Standard Halo Model. In Figs. 4.2, 4.3 and 4.4, we show the limits in the proton-neutron basis for XENON1T [124] (left panels), PICO-60 [25] (middle panels) and IceCube [13] (right panels). For the latter, we show the corresponding results assuming the W^+W^-- channel ($\tau^+\tau^-$-channel) for $m_\chi > 100\,\mathrm{GeV}$ ($m_\chi < 100\,\mathrm{GeV}$). Fig. 4.5 can be used to convert the presented results for IceCube of Figs. 4.2, 4.3 and 4.4 into the results for $\tau^+\tau^-$ in the mass range 100 GeV to 10 TeV and $b\bar{b}$. It does not require any information about the interaction operator being responsible for the capture of the dark matter particles.

For the dashed lines we assumed only one operator at a time, but allowed the interference among the proton and neutron component. We obtained the solid lines by allowing interference among the proton and neutron component *and* all possible operators. To compare our results with the published limits, we added the dotted line for which we made the assumptions of having an isoscalar interaction and only one operator at a time.

From Figs. 4.2, 4.3 and 4.4 it becomes clear that the limit is strongest making specific assumptions, such as assuming isoscalar interaction, whereas it gets relaxed taking interference into account. While the parameter space above the solid lines is excluded at 90% C.L. and assuming a Maxwell-Boltzmann velocity distribution, the parameter space below is not necessarily excluded as the published limits (dotted lines) suggest. In some cases the impact of interference on the limits can be significant: The limits for XENON1T can be weakened by up to 4 orders of magnitude (like *e.g.* c_{11}^p), for PICO-60 up to 6 orders of magnitude (like *e.g.* c_4^n) and for IceCube up to 2 orders of magnitude, (like *e.g.* c_{11}^τ).

To get more insight, we make use of the geometrical property of Eq. (3.30) of leading to an allowed parameter space in the c_i^p-c_i^n parameter space taking only one interaction operator into account. In Figs. 5.3 and 5.4, we show the resulting single experiment allowed parameter spaces at 90% C.L. for $m_\chi = 1$

TeV for XENON1T (blue), PICO-60 (green) and IceCube (yellow). These plots illustrate the impact of proton-neutron interference on the limits of the dark matter-nucleon coupling strengths for each of the 14 interaction operators. Note that our analysis for the XENON1T experiment excludes the point $c_i^p = c_i^n = 0$, due to the large number of observed events compared to the background expectation. A more refined analysis by the XENON collaboration, however, includes this point.

Figs. 5.3 and 5.4 show that the relaxation of the limits depend on the orientation and the size of the allowed parameter spaces. In general one can say that the relaxation is stronger, the less the allowed parameter space is aligned to the c_i^p- or c_i^n-axes and the more it is elongated. A relaxation due to the allowed parameter space's orientation can *e.g.* be seen in the plot for $\hat{\mathcal{O}}_1$ for the 3 experiments. In the exclusion plot for $\hat{\mathcal{O}}_4$ in Fig. 4.2 *e.g.* we see that the relaxation is significant as well. Regarding the corresponding allowed parameter spaces, they are closely aligned to the c_i^p- and c_i^n-axes. At the same time, however, they are strongly elongated which is caused by strong cancellations of the interfering contributions[2].

Due to its composition of many different elements with their unique properties, the Sun can be seen as multiple target experiment. While every single element in the Sun actually results in a unique allowed parameter space, we show in Figs. 5.3 and 5.4 only the resulting allowed parameter space containing all elements, since we are interested in the model-independent limits on the couplings using the dark matter capture process in the Sun in which the combination of all elements contributes. For a deeper investigation of how the eccentricity and size of the final allowed parameter spaces are determined by the unique allowed parameter spaces of the single elements, we refer to Appendix C. There, we also comment on how the elements' properties together with the interaction operators affect the limits.

---

[2] Strong cancellations occur if there is a large hierarchy between the eigenvalues of the $\mathbb{N}$-matrix. At the same time, this can be the origin of numerical instabilities. In Appendix D, we estimate its impact on the calculation of the limits

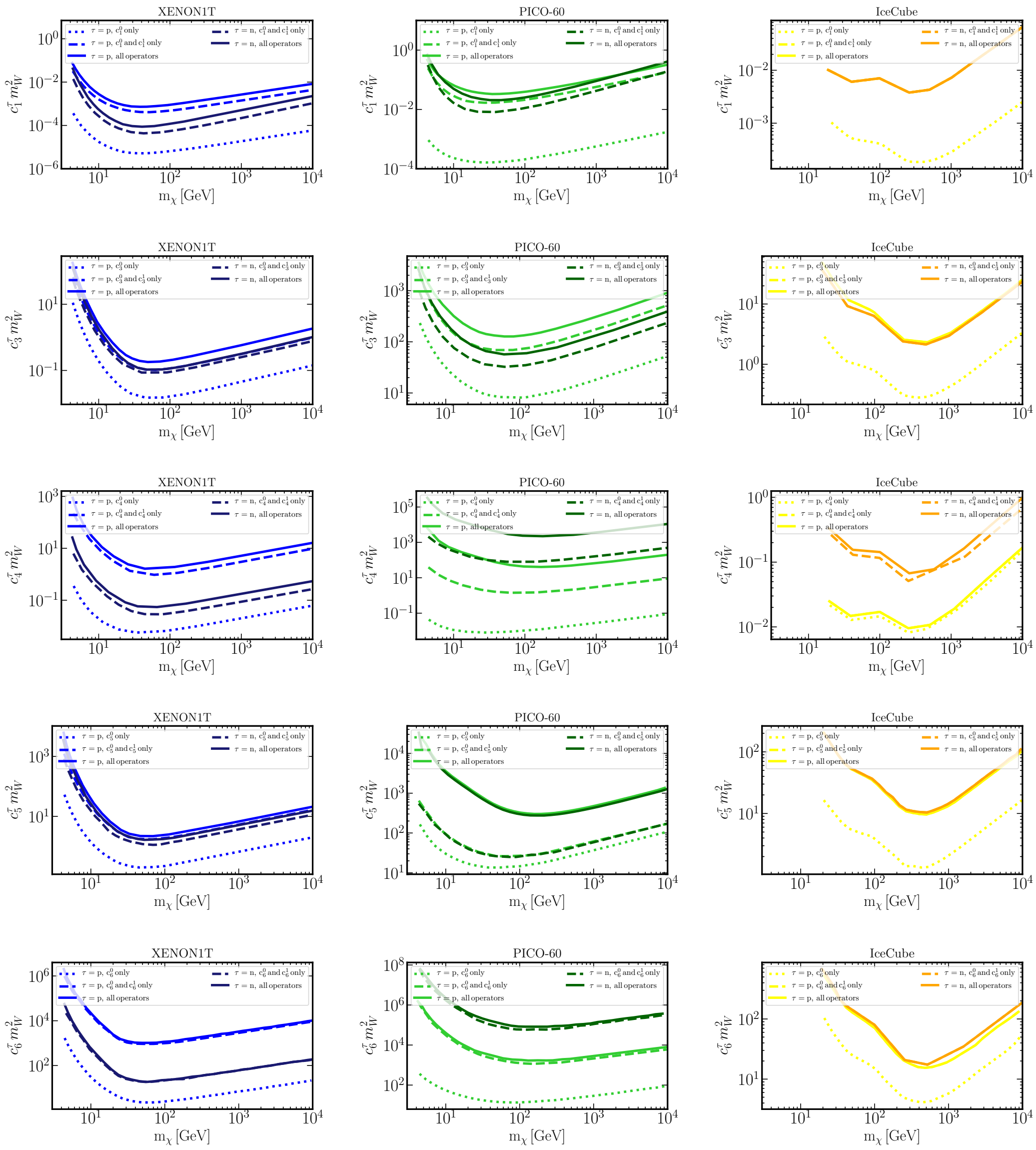

Figure 4.2: 90% C.L. upper limits on the coupling strengths c_i^p and c_i^n for $i = 1, 3, ..., 6$ for XENON1T (left), PICO-60 (middle) and IceCube (right). For the dotted lines, we assumed neither interference among the proton and neutron component, nor among the interaction operators. For the dashed line, we allow the interference among the proton and neutron component for one operator. For the solid line, we allow interference among the proton and neutron component, and among all interaction operators. For IceCube, we assumed the annihilation final state W^+W^- ($\tau^+\tau^-$) for $m_\chi > 100$ GeV ($m_\chi < 100$ GeV).

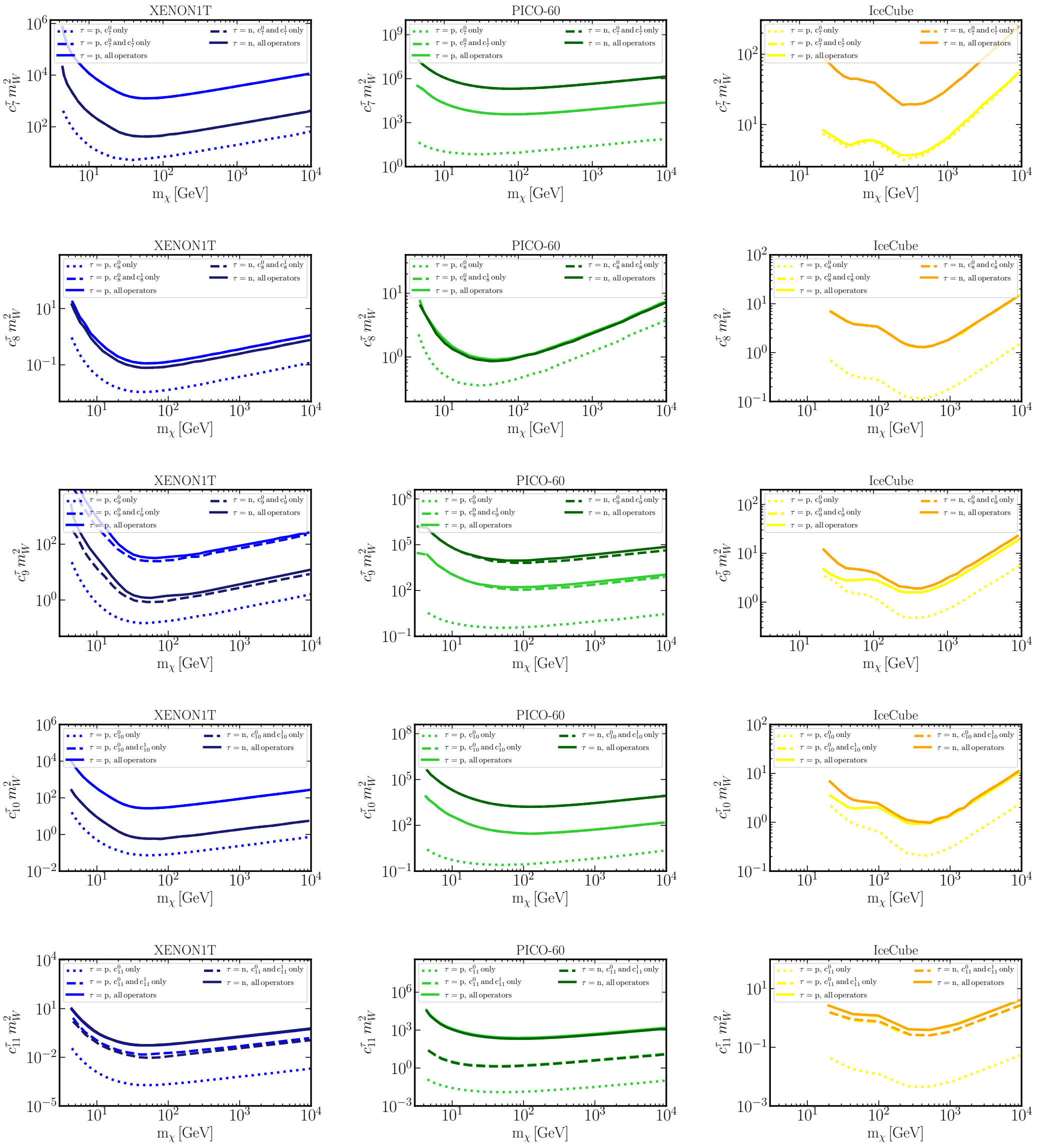

Figure 4.3: 90% C.L. upper limits on the coupling strengths c_i^p and c_i^n for $i = 7, ..., 11$ for XENON1T (left), PICO-60 (middle) and IceCube (right). For the dotted lines, we assumed neither interference among the proton and neutron component, nor among the interaction operators. For the dashed line, we allow the interference among the proton and neutron component for one operator. For the solid line, we allow interference among the proton and neutron component, and among all interaction operators. For IceCube, we assumed the annihilation final state W^+W^- ($\tau^+\tau^-$) for $m_\chi > 100$ GeV ($m_\chi < 100$ GeV).

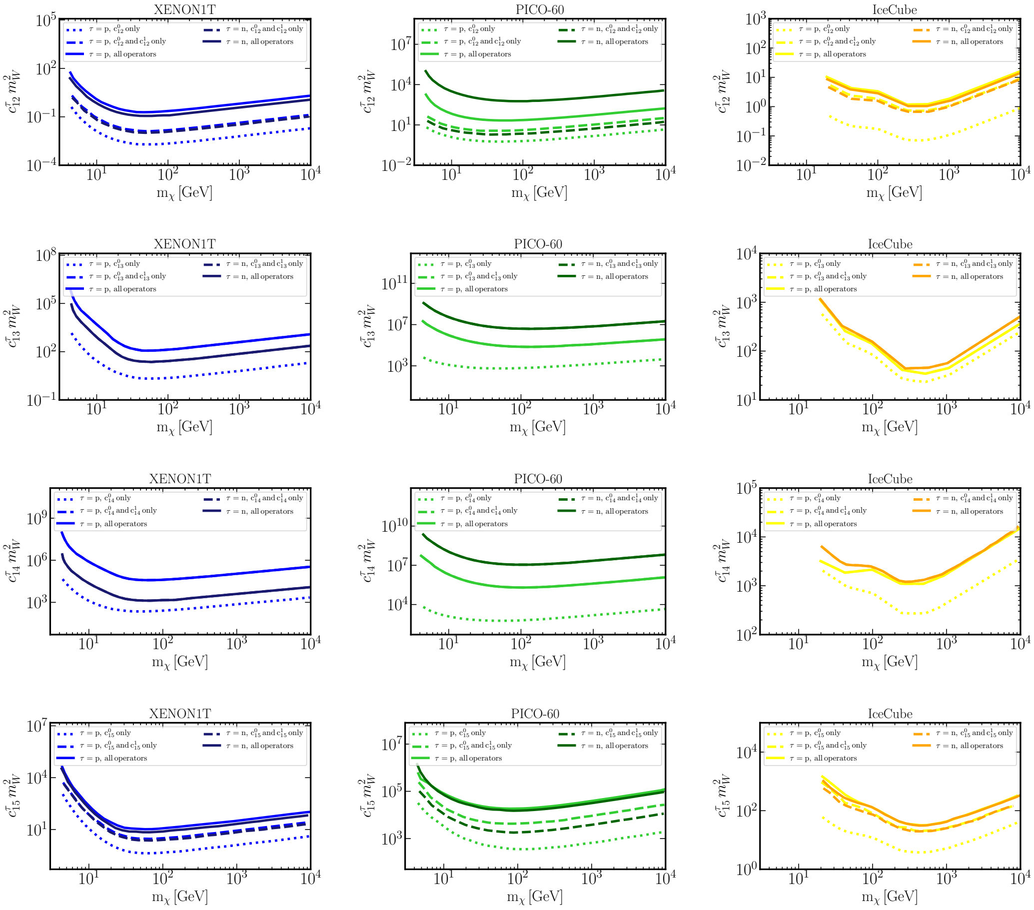

Figure 4.4: 90% C.L. upper limits on the coupling strengths c_i^p and c_i^n for $i = 12, ..., 15$ for XENON1T (left), PICO-60 (middle) and IceCube (right). For the dotted lines, we assumed neither interference among the proton and neutron component, nor among the interaction operators. For the dashed line, we allow the interference among the proton and neutron component for one operator. For the solid line, we allow interference among the proton and neutron component, and among all interaction operators. For IceCube, we assumed the annihilation final state W^+W^- $(\tau^+\tau^-)$ for $m_\chi > 100$ GeV $(m_\chi < 100$ GeV).

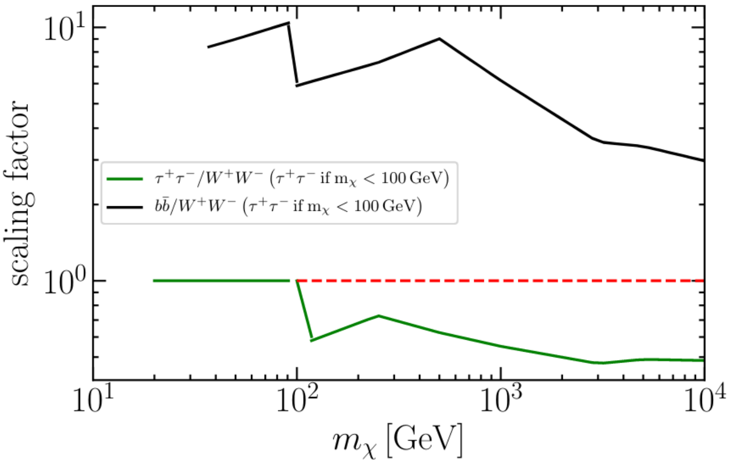

Figure 4.5: Scaling factor to convert the limits of the right panel in Figs. 4.2, 4.3 and 4.4 into the the limits for the annihilation channels $\tau^+\tau^-$ for $m_\chi > 100$ GeV and $b\bar{b}$.

5

Cross-section limits for combined experiments

Since targets with complementary properties, as the elements inside the Sun, can constrain all directions in the vast parameter space, we adapted the formalism we developed in subsection 4.1 such that it allows a combined analysis of multiple dark matter detection experiments. The aim is to find the parameter space that is allowed by all experiments taken into account, such as in Fig. 5.1. There, we schematically show the two-dimensional parameter space spanned by the couplings c_α and c_β. Using data provided by experiment ε_1, we obtain the allowed parameter space that is illustrated in blue, whereas the parameter space marked in green is allowed by experiment ε_2, both at 90% C.L. The region in parameter space that is allowed by both experiments at 90% C.L. is illustrated in red. While the red cross is ruled out by assuming that $c_\beta = 0$, it is still allowed by the model-independent single experiment limit of ε_1. By combining ε_1 and ε_2 we can now exclude it by the strong, but still model-independent limit $\max\{c_\alpha\}|_{\varepsilon_1+\varepsilon_2}$.

In the first section, we develop the method that allows a combined analysis of several experiments and leads to the model-independent upper limit on the dark matter-nucleon couplings of the combined parameter space, which we present in the second section.

5.1 Developing a method for combined analysis

To determine a 90% C.L. limit on the coupling strengths by combining n experiments, we again start with the Lagrangian. In this case it reads

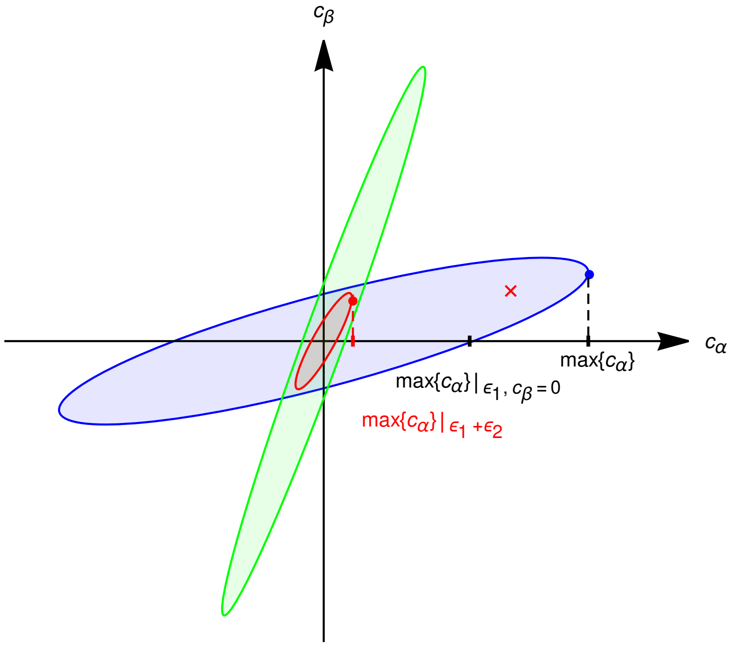

Figure 5.1: Allowed parameter space at 90% C.L. of experiments ε_1 (blue) and ε_2 (green). While the red point is excluded by the limit $\max\{c_\alpha\}|_{\varepsilon_1, c_\beta=0}$, it is still allowed by data and therefore not excluded by the model-independent limit $\max\{c_\alpha\}$. The combination of experiment ε_1 with experiment ε_2 allows to set a strong but conservative limit $\max\{c_\alpha\}|_{\varepsilon_1+\varepsilon_2}$ using the parameter space that is allowed by both experiments at 90% C.L. (red).

$$L = c_\alpha - \lambda \left[\chi^2_{\text{tot}}(\mathbf{c}) - \chi^2_{\text{tot,min}} - n_0 \right], \tag{5.1}$$

with

$$\chi^2_{\text{tot}}(\mathbf{c}) = \sum_\varepsilon \chi^2_\varepsilon(\mathbf{c}). \tag{5.2}$$

Proceeding analogously to section 4.1, we obtain

$$c_\beta^{\max} = \frac{1}{2\lambda} \left(\mathbb{X}^{-1}_{\beta\alpha} \right), \tag{5.3}$$

where

$$\mathbb{X} = \sum_\varepsilon \left[2 a_\varepsilon N_\varepsilon^{\text{sig}}(\mathbf{c}^{\max}) + b_\varepsilon \right] \mathbb{N}_\varepsilon. \tag{5.4}$$

Inserting this into Eq. (3.30), for each experiment we obtain n implicit equations for the number of events at the n experiments, $N_{\varepsilon}^{\mathrm{sig}}\left(\mathbf{c}^{\max}\right)$, given as

$$N_{\varepsilon}^{\mathrm{sig}}\left(\mathbf{c}^{\max}\right) = \frac{1}{4\lambda^2}\left(\mathbb{X}^{-1}\mathbb{N}_{\varepsilon}\mathbb{X}^{-1}\right)_{\alpha\alpha} . \tag{5.5}$$

Using Eq. (5.5) together with

$$\chi^2_{\mathrm{tot}}(\mathbf{c}) - \chi^2_{\mathrm{tot,min}} = n_0 \tag{5.6}$$

we can find solutions for $N_{\varepsilon}^{\mathrm{sig}}\left(\mathbf{c}^{\max}\right)$ and λ. Finally, the maximum value for the coupling c_{α} is determined by

$$c_{\alpha}^{\max} = \frac{1}{2\lambda}\left(\mathbb{X}^{-1}\right)_{\alpha\alpha} . \tag{5.7}$$

5.2 Upper limits on the coupling strengths from the combination of several experiments

In Fig. 5.5, we show the 90% C.L. upper limits on the dark matter-nucleon coupling strength assuming one operator and isoscalar interaction only. The red line is the result of the combined analysis of XENON1T, PICO-60 and IceCube. In order to see the impact of combining the experiments, we also show the limits of the individual experiments. It turns out that for purely isoscalar interactions, the limits for higher masses are mostly dominated by the single experiment limit of XENON1T, whereas for low masses PICO-60 dominates for some operators. Note that for some operators, *e.g.* $\hat{\mathcal{O}}_{14}$, and dark matter masses the combined isoscalar limit does not exist. The reason is the large number of observed events in XENON1T; the parameter space related to isoscalar interactions is ruled out by the combination of XENON1T, PICO-60 and/or IceCube data. Such a case is schematically shown in Fig. 5.2.

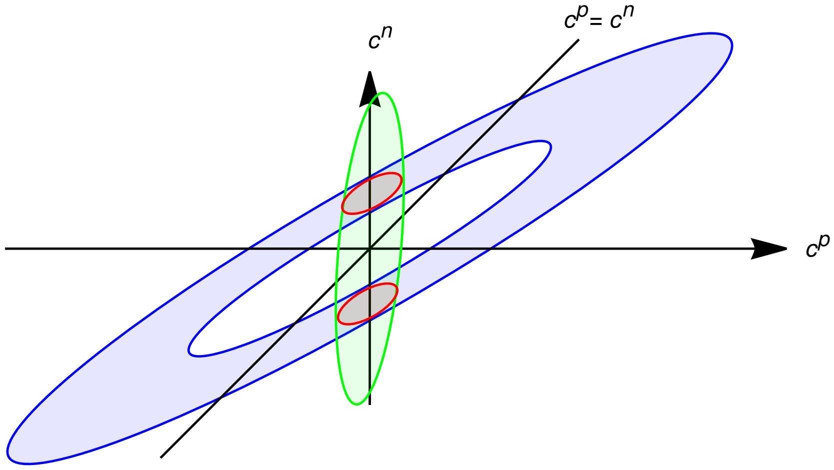

Figure 5.2: Allowed parameter space at 90% C.L. of experiment ε_1 (blue) and ε_2 (green). The black line illustrates the specific case in which $c^p = c^n$, which is excluded by the combination of both experiments (red).

We want to emphasize that we neither want to confirm the exclusion of isoscalar interactions nor the detection of dark matter. Our aim was to apply the developed methodology and to point out that (1) the interference among operators can relax the limits significantly and (2) a combination of experi-

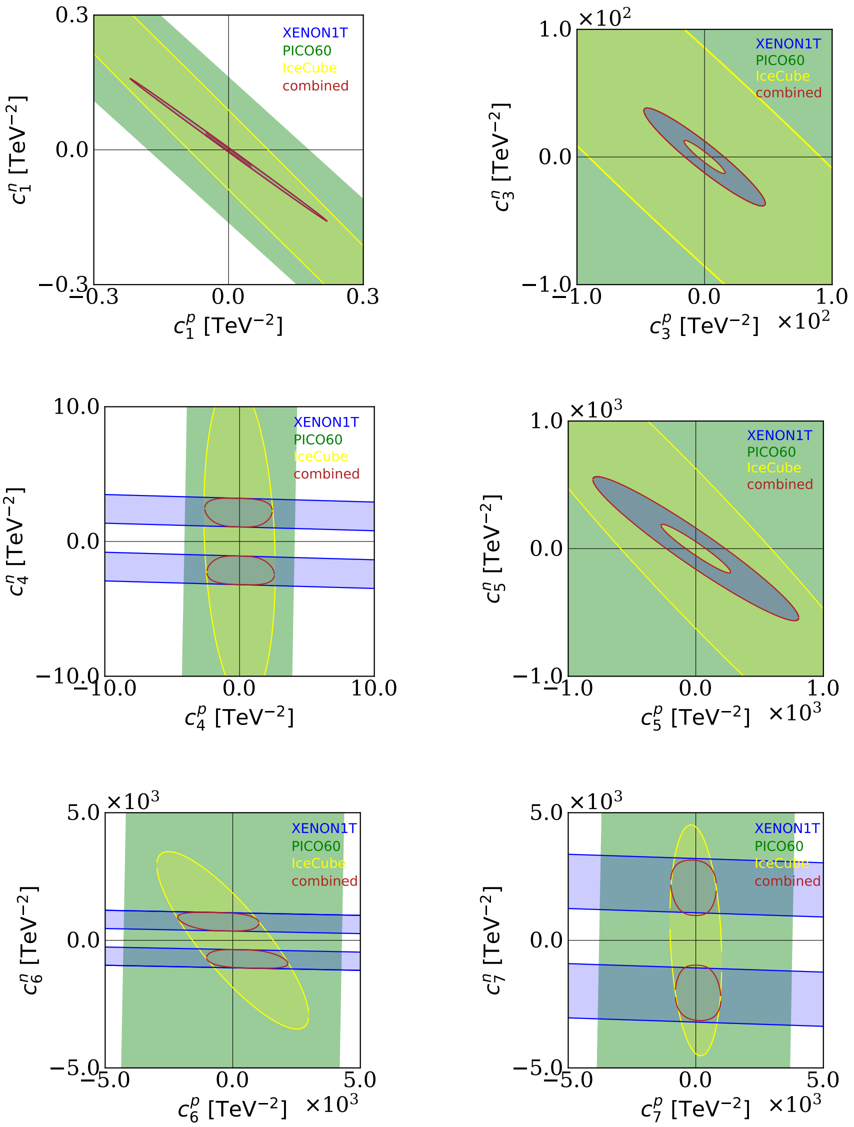

Figure 5.3: Allowed parameter space at 90% C.L. for operators 1 to 7 from XENON1T (blue), PICO-60 (green), IceCube (yellow) and the combination of these (red) for $m_\chi = 1$ TeV.

ments can lead to strong model-independent limits.

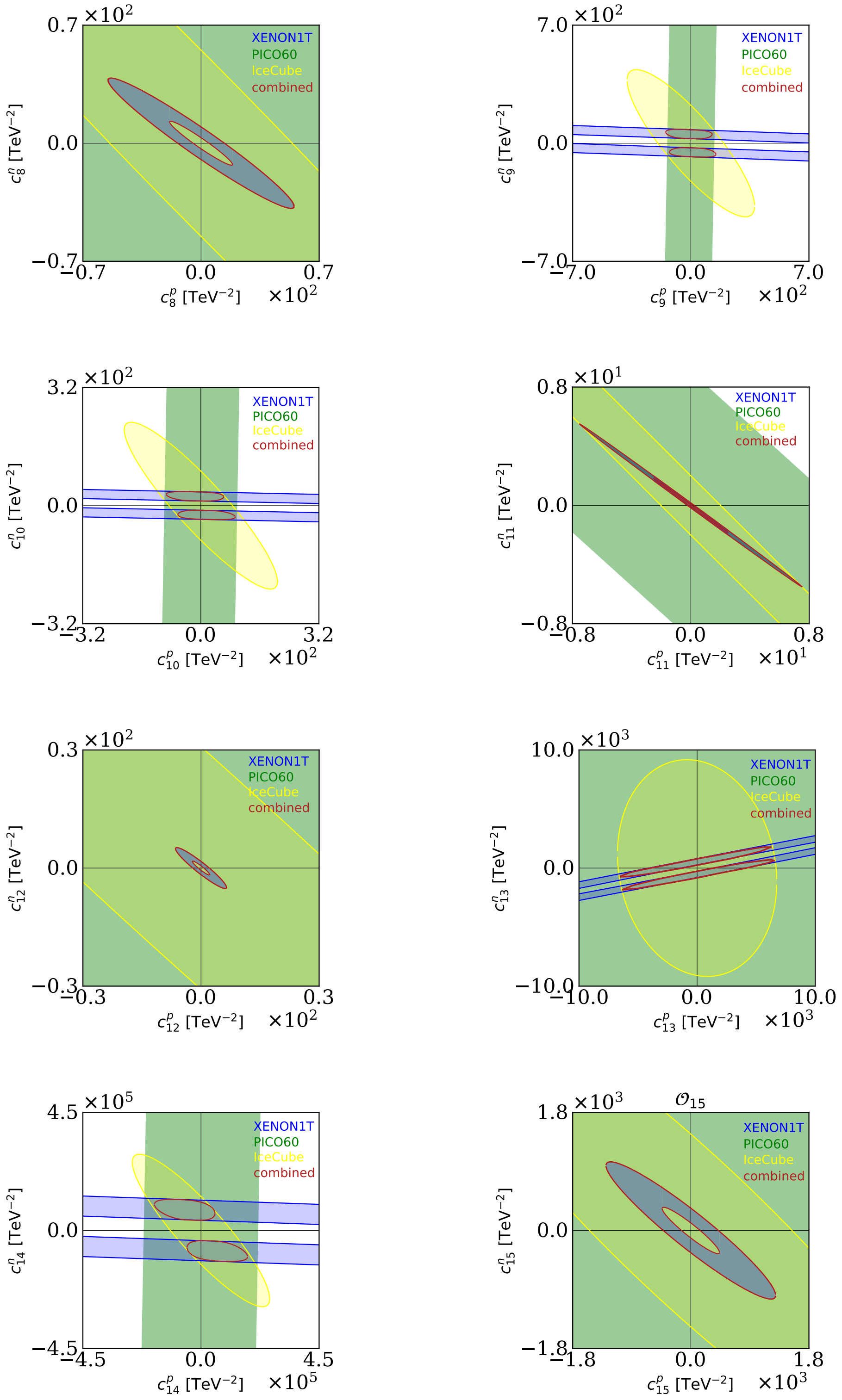

Figure 5.4: Same as Fig. 5.3 but for operators 8 to 15.

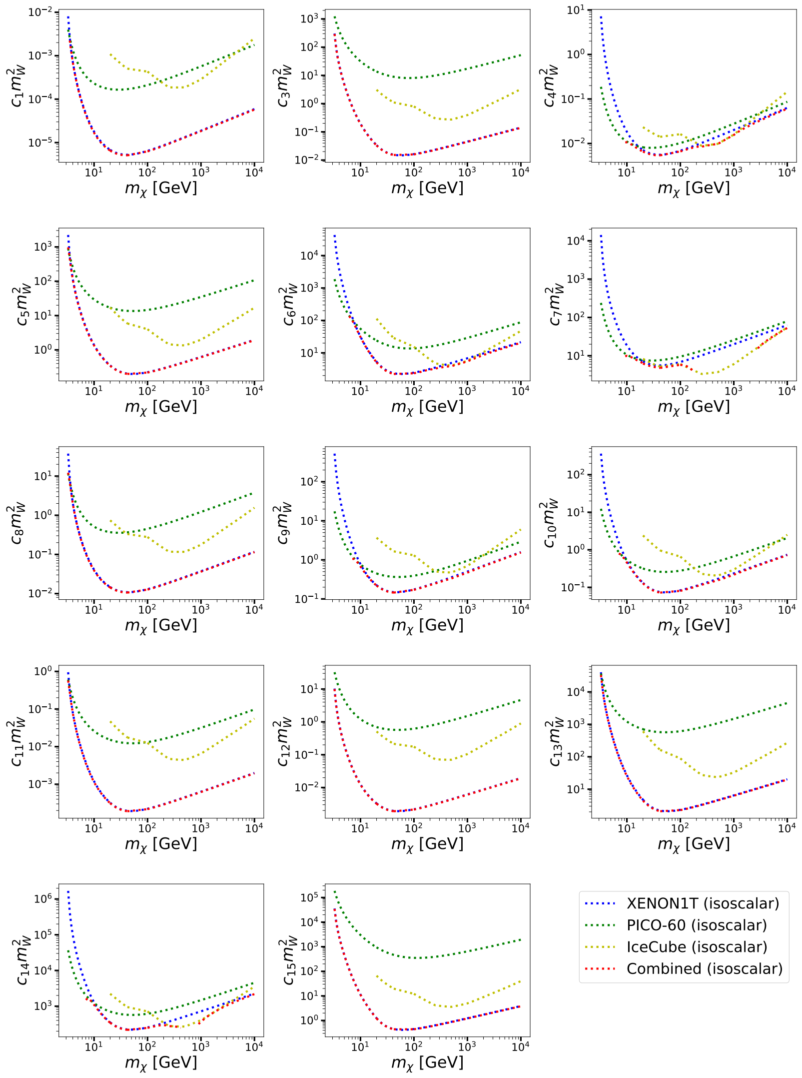

Figure 5.5: 90% C.L. limit on the dark matter-neutron couplings for the interaction operators $\hat{\mathcal{O}}_i$ ($i = 1, 3, ..., 15$) using data from XENON1T (blue), PICO-60 (green), IceCube (yellow) and the combination of data provided by the three experiments, under the assumption of isoscalar interaction.

Fig. 5.6 shows limits for one interaction operator at a time, but allowing interference among isoscalar and isovector interaction. The red dashed line corresponds to the limits we obtain by combining XENON1T, PICO-60 and IceCube. We additionally show the combined limit assuming only isoscalar interaction as red dotted line. We see that especially for the operators $\hat{\mathcal{O}}_4$, $\hat{\mathcal{O}}_6$, $\hat{\mathcal{O}}_7$, $\hat{\mathcal{O}}_9$, $\hat{\mathcal{O}}_{10}$, $\hat{\mathcal{O}}_{13}$ and $\hat{\mathcal{O}}_{14}$, the combination of the experiments has a significant impact on the limits. This can also be concluded when looking at Figs. 5.3 and 5.4; for the mentioned operators the allowed parameter space of c_i^p and c_i^n are nearly orthogonal. For the other operators and $m_\chi = 1$ TeV, we see in Figs. 5.3 and 5.4 that the allowed parameter space of XENON1T lies completely within the allowed parameter spaces of PICO-60 and IceCube, which leads to the conclusion that the combined limit is equivalent to the limit of XENON1T. This is also reflected by the limit plots in Fig. 5.6 for $m_\chi = 1$ TeV; the combined limit coincides with the limit of XENON1T. Same conclusions hold for other dark matter masses. For a detailed discussion on how properties of different elements affect the orientation of allowed parameter spaces for a given interaction operator, we again refer to Appendix C.

In Fig. 5.7, we show as red solid line the limit resulting in combining the three experiments and allowing not only interference among the isoscalar and isovector component, but also among the 14 interaction operators. Firstly, comparing this limit to the red dotted and red dashed line (combined limit assuming only isoscalar interactions and allowing isospin interference, respectively) a small relaxation occurs for some operators. Secondly, comparing the red solid line to the individual limits of the experiments, we again see that there must be a complementarity between the allowed parameter spaces of XENON1T, PICO-60 and/or IceCube.

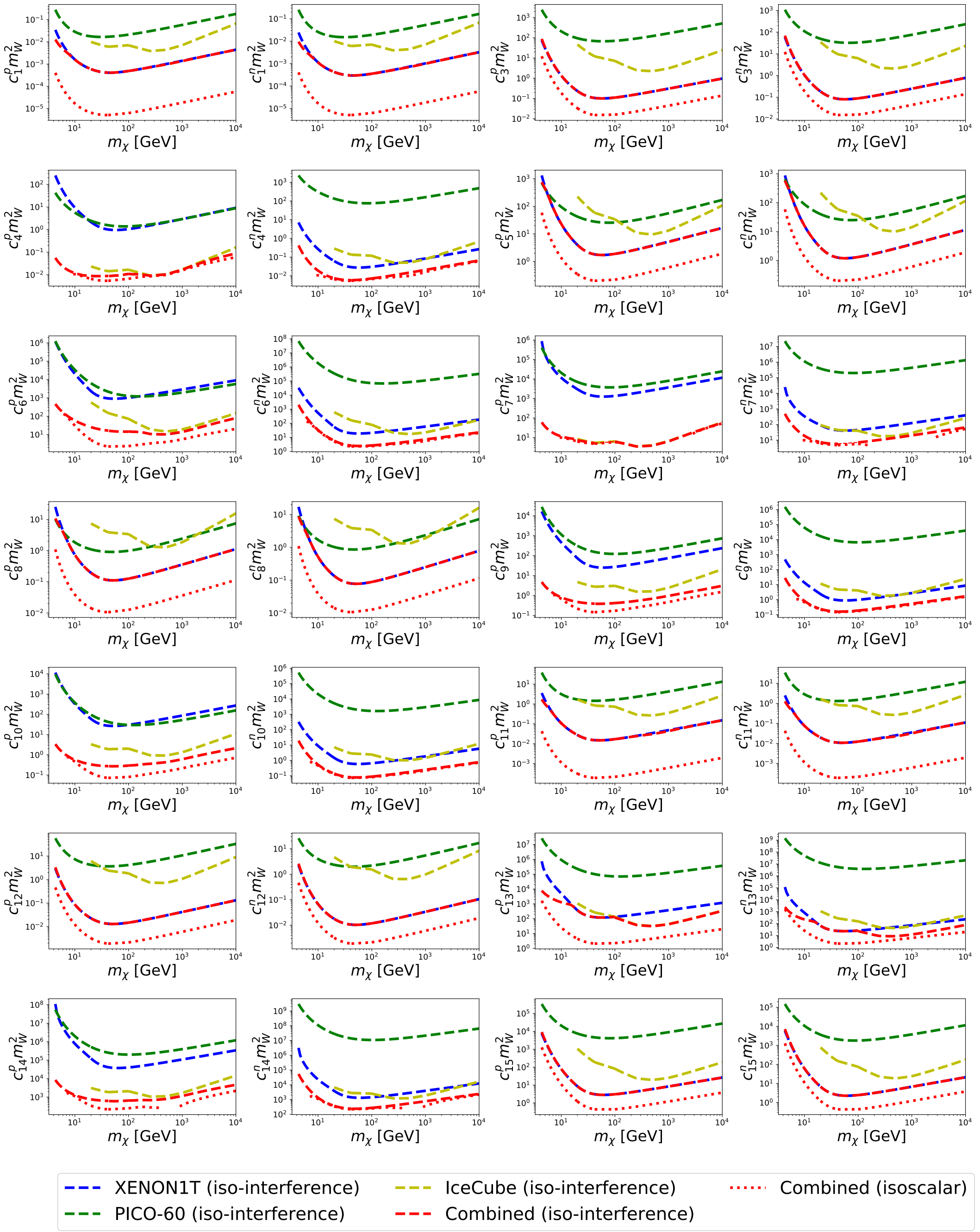

Figure 5.6: 90% C.L. limit on the dark matter-neutron couplings for the interaction operators $\hat{\mathcal{O}}_i$ $(i = 1, 3, ..., 15)$ using data from XENON1T (blue), PICO-60 (green), IceCube (yellow) and the combination of data provided by the three experiments, under the assumption of isospin interference.

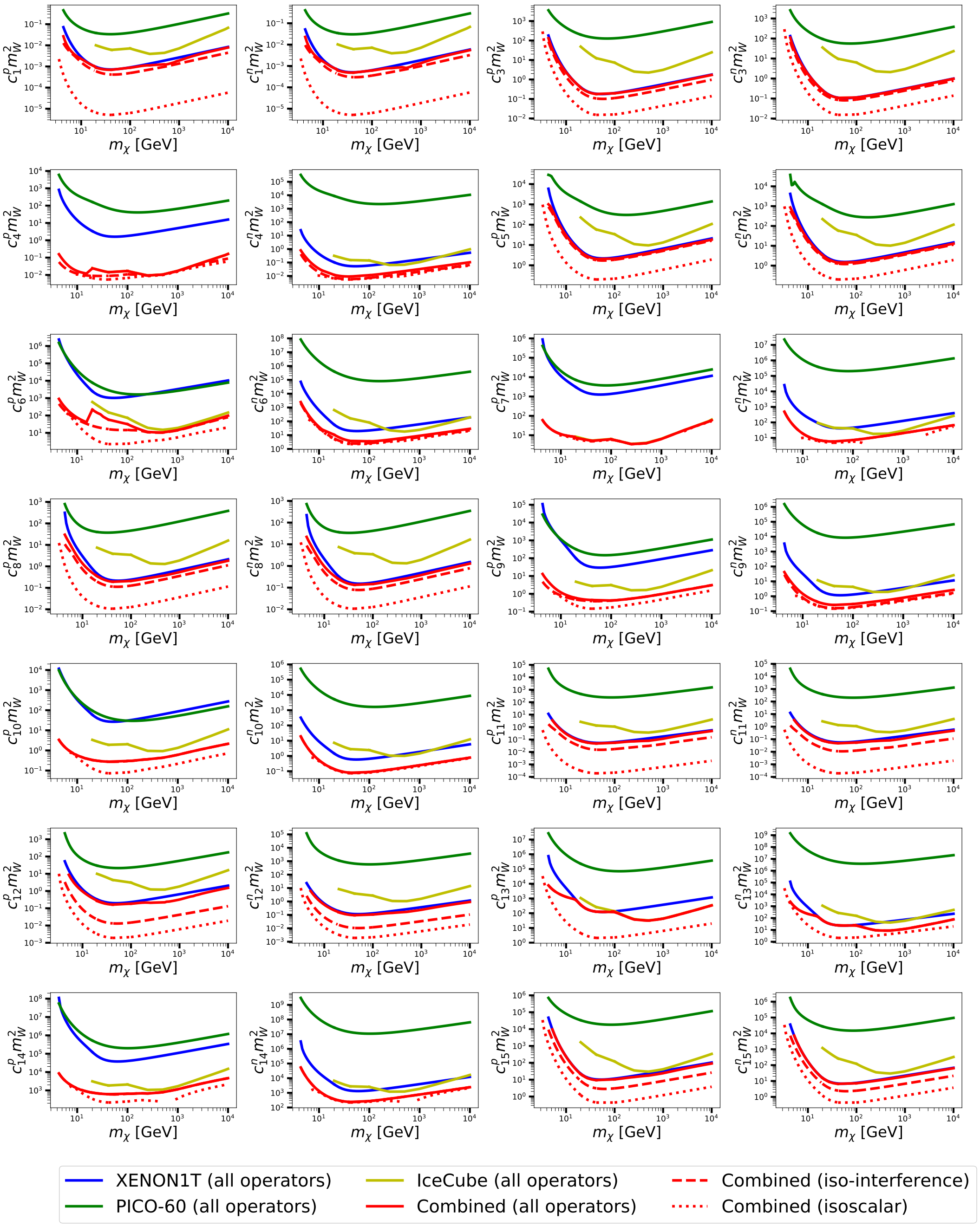

Figure 5.7: 90% C.L. limit on the dark matter-neutron couplings for the interaction operators $\hat{\mathcal{O}}_i$ ($i = 1, 3, ..., 15$) using data from XENON1T (blue), PICO-60 (green), IceCube (yellow) and the combination of data provided by the three experiments, under the assumption of isospin interference and interference among all operators.

6

A model- and halo-independent analysis

Another common assumption is the Standard Halo Model in which the local dark matter density is $\rho_{\rm loc} = 0.3\,\mathrm{GeV\,cm^{-3}}$ and the dark matter particles follow a Maxwell-Boltzmann velocity distribution truncated at the escape velocity of the Milky Way, $v_{\rm esc} = 550\,\mathrm{km\,s^{-1}}$, and the velocity dispersion $v_0 \simeq 220\,\mathrm{km\,s^{-1}}$. However, the true values of the local dark matter density and velocity distribution are unknown. Possible signals from direct detection experiments and the dark matter capture in the Sun, though, depend on these quantities: Dark matter particles in the high velocity tail of the velocity distribution generate more energetic recoils in direct detection experiments [150], whereas dark matter particles in the low velocity tail are more likely to be captured by the Sun [151, 152].

The model-independent limits in the previous chapters are only valid for the Standard Halo Model, *i.e.* if the dark matter velocity distribution in the galactic halo follows a Maxwell-Boltzmann velocity distribution. Due to the expected deviations from the Standard Halo Model and Maxwell-Boltzmann velocity distribution in the Solar System, we use the methods presented in section 4.1 and in [146, 153] to subject the limits to a model- *and* halo-independent analysis. For this, one introduces the parameter [153]

$$\mathit{\Delta} \geq \left| \frac{f(\mathbf{w}) - f_{\rm MB}(\mathbf{w})}{f_{\rm MB}(\mathbf{w})} \right| \tag{6.1}$$

which quantifies the deviation of the actual velocity distribution $f(\mathbf{w})$ from the Maxwellian. In Fig. 6.1 we show the Maxwell-Boltzmann distribution (black) and the bands around are characterized by specific $\mathit{\Delta}$'s. We chose $\mathit{\Delta} = 1$, 10, 100 and 1000 (see legend).

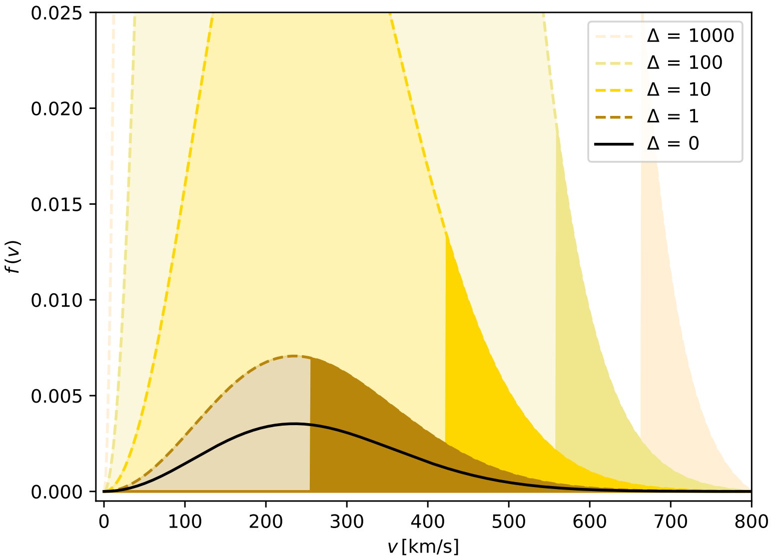

Figure 6.1: Optimized velocity distributions (non-transparent) providing the weakest limits on the dark matter-nucleon coupling strength in the case of IceCube for $\Delta = 0$ (Maxwell-Boltzmann), 1, 10, 100 and 1000. For each of these values we additionally show the largest possible deviation from the Maxwell-Boltzmann distribution as transparent region limited by a dashed line colored correspondingly.

Since we want to obtain the weakest halo-independent limit, we have to find a velocity distribution that leads to the smallest capture rate. Since the capture rate decreases monotonically for increasing dark matter velocity, it is minimized when the dark matter particles carry velocities as high as possible. We show these velocity distributions in Fig. 6.1 for different values of Δ. The optimized velocity distribution saturates the upper boundary of the corresponding band at the high velocity tail down towards lower velocities until it switches down to the lower boundary caused by the normalization condition in Eq. (2.11).

Assuming $\Delta = 0$ (Maxwell-Boltzmann), 1, 10, 100 and 1000, we calculate the 90% C.L. model- and halo-independent limits on the dark matter-nucleon couplings using IceCube data, taking only one operator at a time and assuming interference among the proton and neutron components. As in the previous section we consider the W-channel for $m_\chi \geq 100$ GeV and the τ-channel for

m_χ < 100 GeV. We show the results in the Figs. 6.3 - 6.11.

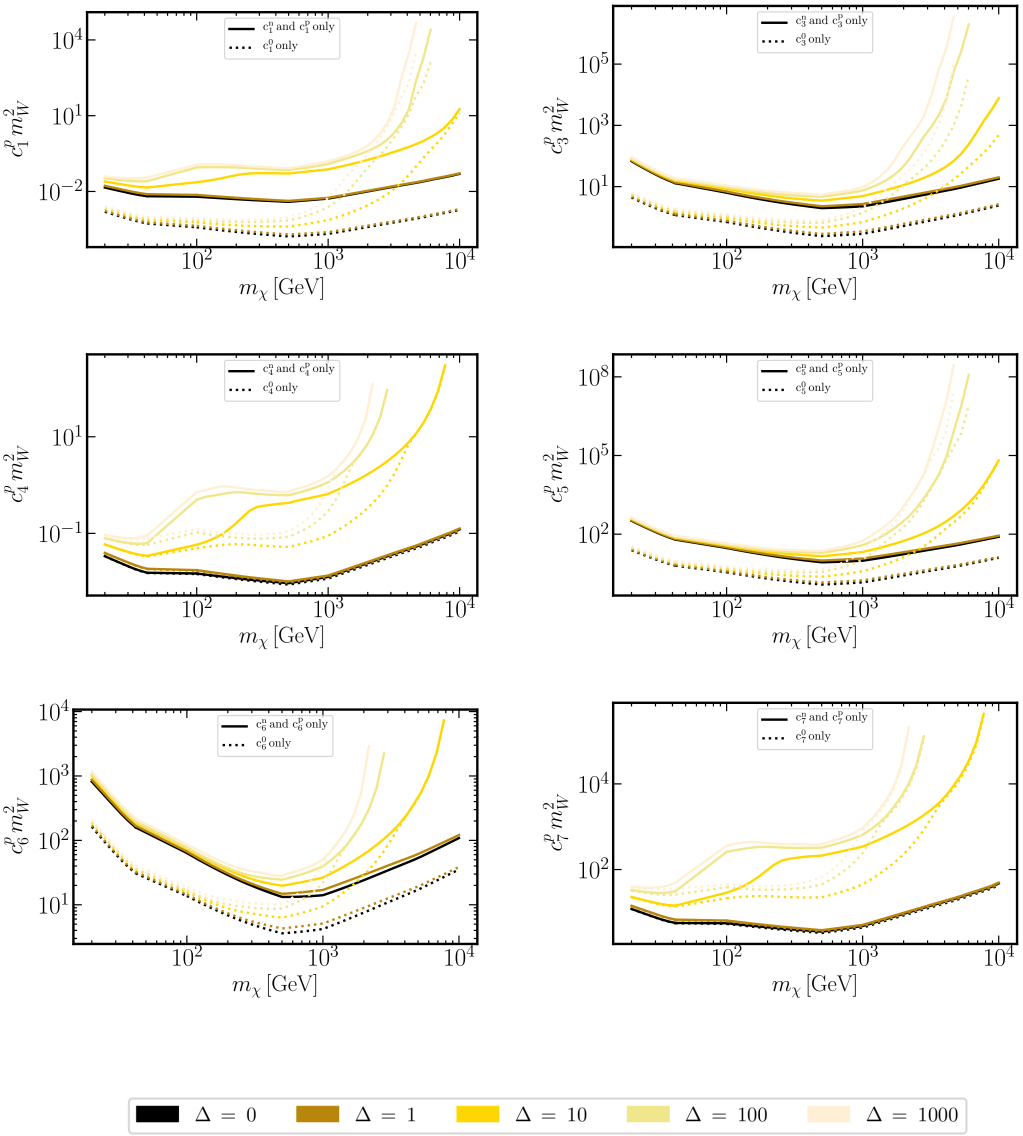

Figure 6.3: Model- and halo-independent 90% C.L. limits on the coupling strengths c_i^p ($i = 1, 3, ..., 7$) assuming $\varDelta = 0$ (Maxwell-Boltzmann), 1, 10, 100 and 1000 taking one operator at a time and assuming interference among the proton and neutron components.

While for dark matter masses $\lesssim$ 100 GeV the limits get relaxed by up to a factor of 2, the limits in the range of 100 GeV $\lesssim m_\chi \lesssim$ 1 TeV can be relaxed by up to two orders of magnitude for $\varDelta \geq 10$ (see *e.g.* $\hat{\mathcal{O}}_4$). The couplings for the largest dark matter masses cannot be constrained for high values of

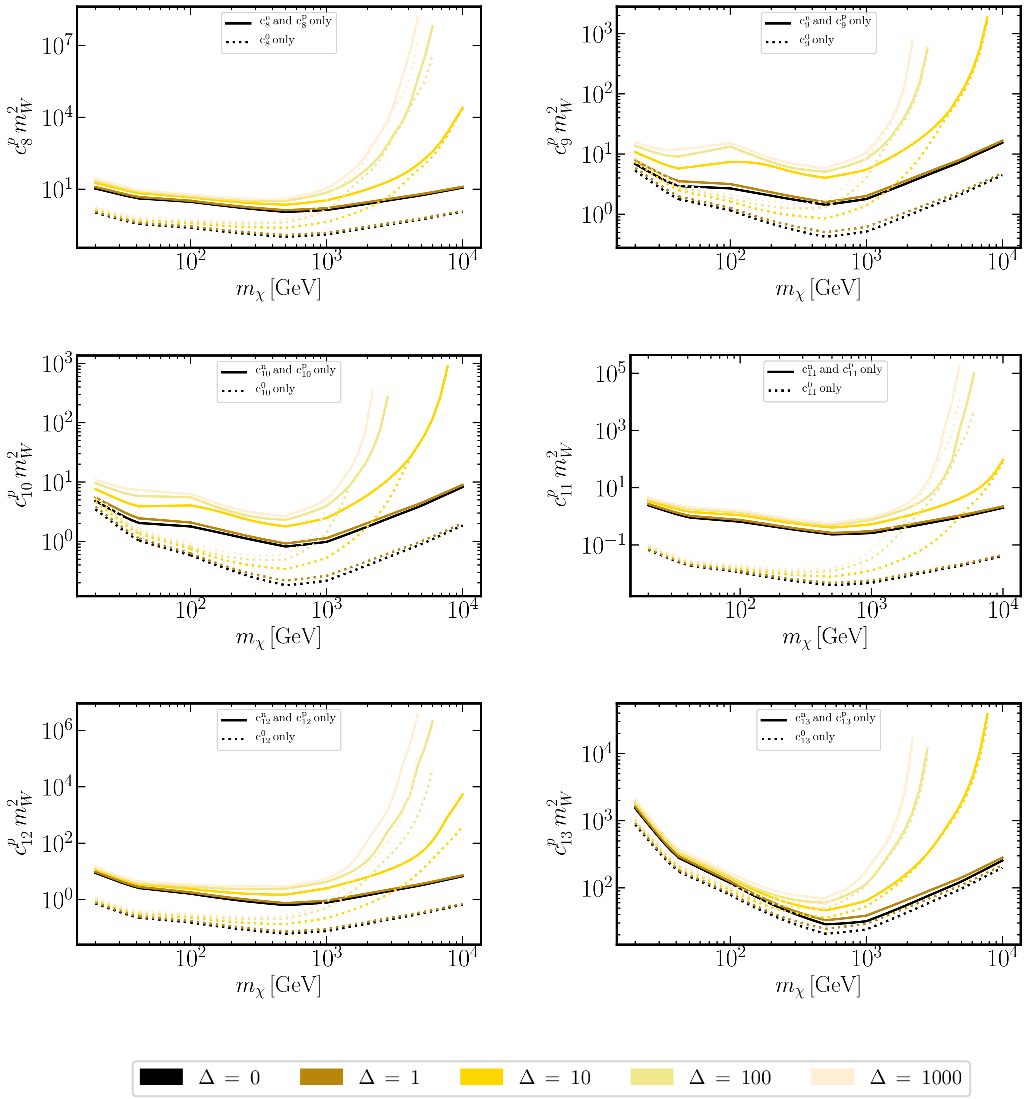

Figure 6.5: Model- and halo-independent 90% C.L. limits on the coupling strengths c_i^p ($i = 8, ..., 13$) assuming $\varDelta = 0$ (Maxwell-Boltzmann), 1, 10, 100 and 1000 taking one operator at a time and assuming interference among the proton and neutron components.

$\varDelta$, since the combination with high velocities prohibits capture kinematically which results in having no limit for this mass range.

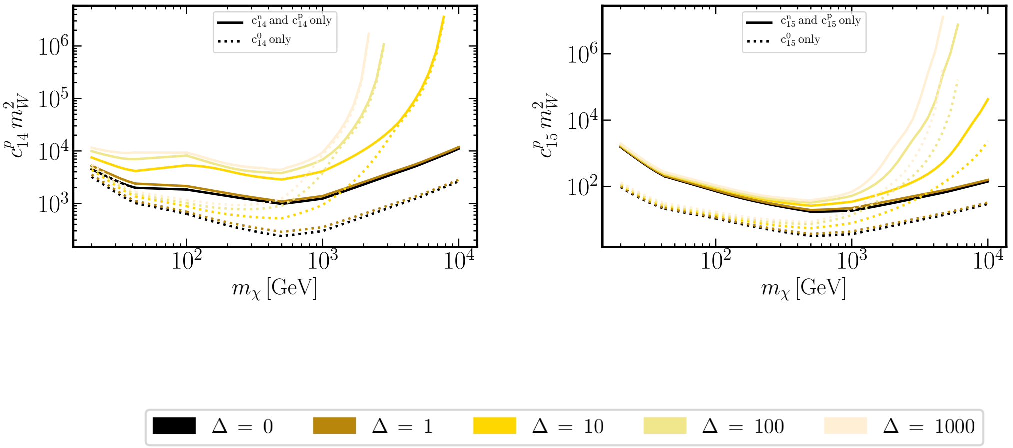

Figure 6.6: Model- and halo-independent 90% C.L. limits on the coupling strengths c_i^p ($i = 14,\ 15$) assuming $\varDelta = 0$ (Maxwell-Boltzmann), 1, 10, 100 and 1000 taking one operator at a time and assuming interference among the proton and neutron components.

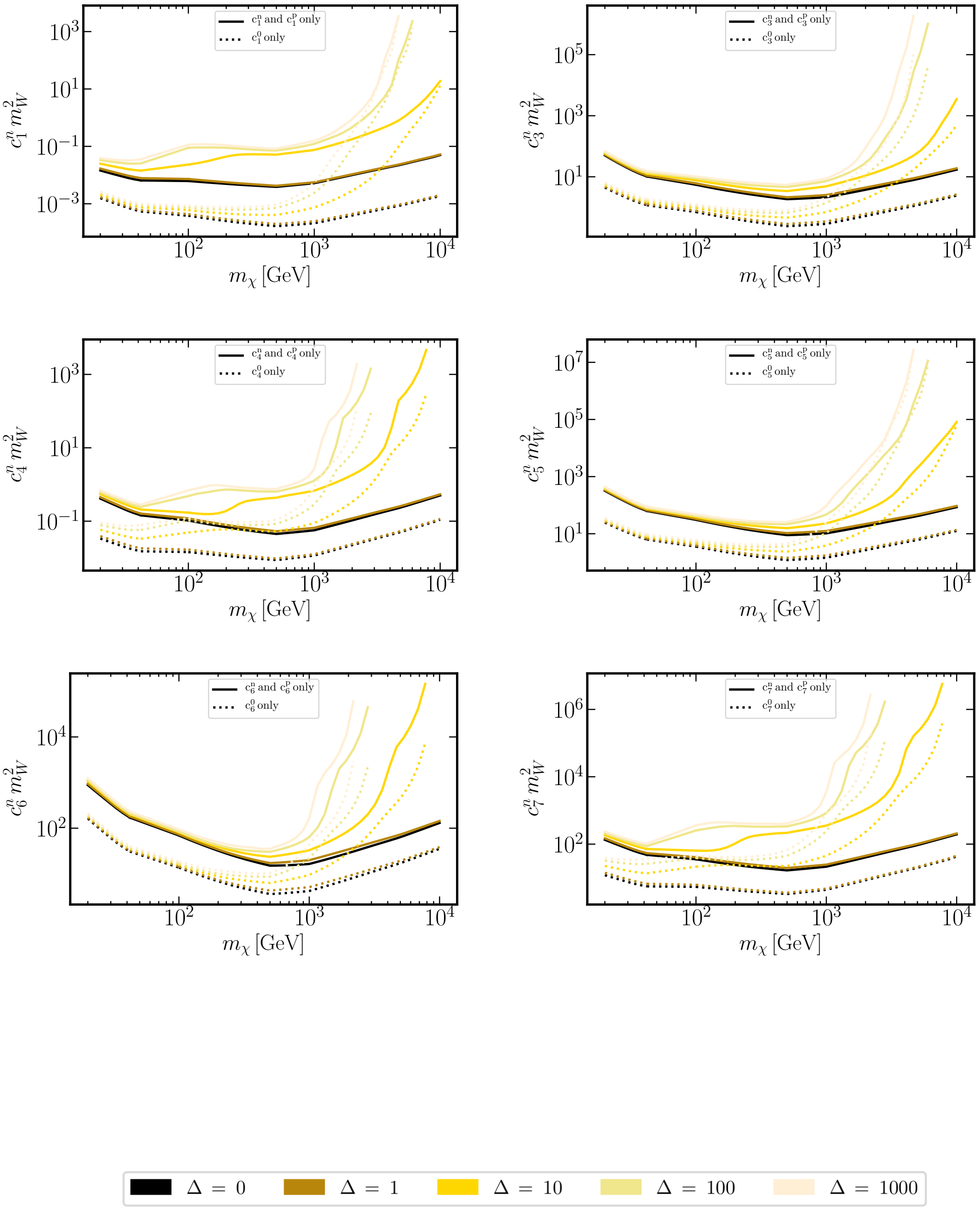

Figure 6.8: Model- and halo-independent 90% C.L. limits on the coupling strengths c_i^n ($i = 1, 3, ..., 7$) assuming $\varDelta = 0$ (Maxwell-Boltzmann), 1, 10, 100 and 1000 taking one operator at a time and assuming interference among the proton and neutron components.

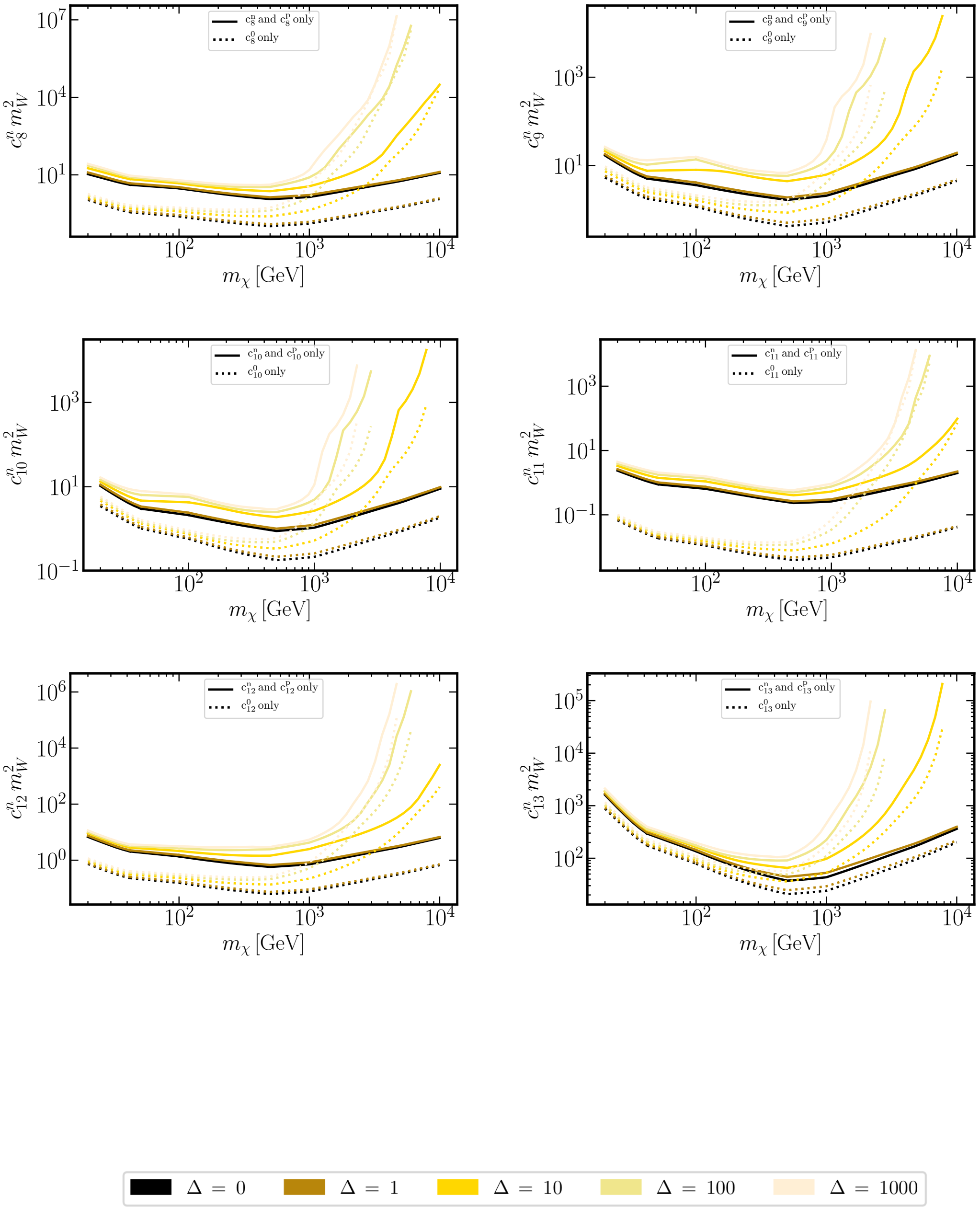

Figure 6.10: Model- and halo-independent 90% C.L. limits on the coupling strengths c_i^n ($i = 8, ..., 13$) assuming $\mathit{\Delta} = 0$ (Maxwell-Boltzmann), 1, 10, 100 and 1000 taking one operator at a time and assuming interference among the proton and neutron components.

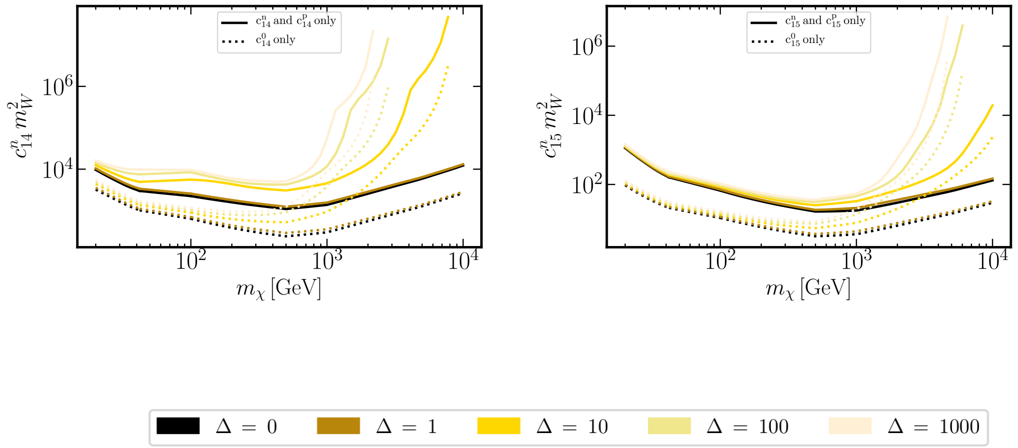

Figure 6.11: Model- and halo-independent 90% C.L. limits on the coupling strengths c_i^n ($i = 14, 15$) assuming $\varDelta = 0$ (Maxwell-Boltzmann), 1, 10, 100 and 1000 taking one operator at a time and assuming interference among the proton and neutron components.

7

Conclusions

In the non-relativistic effective theory the interaction of dark matter particles with nucleons can be induced by different operators (4 (14) for spin-0 (spin-1/2) dark matter). These operators are constructed by considering all possible combinations of the dark matter and nucleon spins, momentum transfer and relative velocity of the scattering, up to second order in the latter. Further, the operators must be Galilean invariant and Hermitian. Since the target for the dark matter particles in this interaction is a nucleon doublet, we further have to take into account its number of internal degrees of freedom, *i.e.* the isospin. It can either be expressed in terms of the isoscalar and isovector, or the proton and neutron components. Together with the interaction operators, we count 8 (28) possible interactions for spin-0 (spin-1/2) dark matter with a nucleus. In order to reduce the number of degrees of freedom, it is common to assume that dark matter couples to protons and neutrons with equal strength when casting null-search results into limits on the dark matter-nucleon interactions. However, it is possible that some interactions interfere with one another, which means that published limits cannot be compared directly to model predictions. In this work, we derived an analytical formula that allows to determine a model-independent upper limit on the coupling strengths. We have applied the derived formula to determine model-independent single-experiment 90% C.L. upper limits of the 28 coupling strengths using data provided by XENON1T, PICO-60 and IceCube. For each coupling strength, we have investigated the impact of, firstly, having only one operator at a time, but interference among the proton and neutron components, and, secondly, taking all operators and the interference among the proton and neutron components into account. We find that, depending on the interaction, the limits can be weakened by up to 4 orders of magnitude for XENON1T (*e.g.* c_{11}^p), 6 orders of magnitude for PICO-60 (*e.g.* c_4^n) and 2 orders of magnitude for IceCube (*e.g.* c_{11}^τ).

We also scrutinized the impact of the complementarity of experiments consisting of elements with different properties. Similar as in our previous study, we developed a methodology that takes into account interference among operators, but considering a set of experiments at a time. This allowed us to determine model-independent 90% C.L. upper limits on the dark matter-nucleon coupling strengths by combining data provided by XENON1T, PICO-60 and IceCube. We found that especially the limits of those operators which depend on the nuclear spin can be strongly affected by the combined analysis; for some couplings it is possible to achieve a strengthening of the limits by 4 orders of magnitude compared to the strongest single-experiment limit (*e.g.* c_4^p).

Another common assumption is that the dark matter velocity distribution in the Solar System follows a Maxwell-Boltzmann distribution. In order to see the effect of possible deviations from the Maxwell-Boltzmann distribution, we additionally subjected the data to a halo-independent analysis. We found that the limits in the small dark matter mass range ($\lesssim$ 100 GeV) are relaxed by up to a factor of 2 and in the intermediate dark matter mass range ($\sim$ 100 GeV to $\sim$ 1 TeV) by up to two orders of magnitude (see *e.g.* $\hat{\mathcal{O}}_4$), whereas the interactions cannot be constrained in the high dark matter mass range ($\gtrsim$ 1 TeV) for large deviations from the Maxwell-Boltzmann distribution.

A

Nuclear response functions

Below, we list the nuclear response functions for te nuclei that are relevant for this thesis, originally provided in Ref. [144]. They only depend on the dimensionless variable $y = \left(\frac{bq}{2}\right)^2$, with the length parameter $b = \sqrt{\frac{41.467}{45A^{-1/3} - 25A^{-2/3}}}$ [143]. Note that we only show the non-zero contributions.

Hydrogen (H)

$$\begin{array}{lll}
W_M^{00}(y) = 0.0397887 & W_{\Sigma''}^{00}(y) = 0.0397887 & W_{\Sigma'}^{00}(y) = 0.0795775 \\
W_M^{11}(y) = 0.0397887 & W_{\Sigma''}^{11}(y) = 0.0397887 & W_{\Sigma'}^{11}(y) = 0.0795775 \\
W_M^{10}(y) = 0.0397887 & W_{\Sigma''}^{10}(y) = 0.0397887 & W_{\Sigma'}^{10}(y) = 0.0795775 \\
W_M^{01}(y) = 0.0397887 & W_{\Sigma''}^{01}(y) = 0.0397887 & W_{\Sigma'}^{01}(y) = 0.0795775
\end{array}$$

Helium (^{3}He)

$$\begin{array}{lll}
W_M^{00}(y) = 0.358099\ e^{-2y} & W_{\Sigma''}^{00}(y) = 0.0397887\ e^{-2y} & W_{\Sigma'}^{00}(y) = 0.0795775\ e^{-2y} \\
W_M^{11}(y) = 0.0397887\ e^{-2y} & W_{\Sigma''}^{11}(y) = 0.0397887\ e^{-2y} & W_{\Sigma'}^{11}(y) = 0.0795775\ e^{-2y} \\
W_M^{10}(y) = 0.119366\ e^{-2y} & W_{\Sigma''}^{10}(y) = -0.0397887\ e^{-2y} & W_{\Sigma'}^{10}(y) = -0.0795775\ e^{-2y} \\
W_M^{01}(y) = 0.119366\ e^{-2y} & W_{\Sigma''}^{01}(y) = -0.0397887\ e^{-2y} & W_{\Sigma'}^{01}(y) = -0.0795775\ e^{-2y}
\end{array}$$

Helium (^{4}He)

$$W_M^{00}(y) = 0.31831\ e^{-2y}$$

Carbon (^{12}C)

$$
\begin{aligned}
W_{M}^{00}(y) &= 0.565882\, e^{-2y}(2.25 - y)^2 \\
W_{\Phi''}^{00}(y) &= 0.0480805\, e^{-2y} \\
W_{M\Phi''}^{00}(y) &= e^{-2y}(-0.371134 + 0.164948y)
\end{aligned}
$$

Nitrogen (^{14}N)

$$
\begin{aligned}
W_{M}^{00}(y) &= e^{-2y}(11.6979 - 11.1409y + 2.67574y^2) \\
W_{\Sigma''}^{00}(y) &= 0.0230079e^{-2y}(1.20986 + y)^2 \\
W_{\Sigma'}^{00}(y) &= 0.134532e^{-2y}(0.707578 - y)^2 \\
W_{\Phi''}^{00}(y) &= 0.0905048\, e^{-2y} \\
W_{\tilde{\Phi}''}^{00}(y) &= 0.00126432\, e^{-2y} \\
W_{\Delta}^{00}(y) &= 0.0424075\, e^{-2y} \\
W_{M\Phi''}^{00}(y) &= e^{-2y}(-1.02414 + 0.483267y) \\
W_{\Sigma'\Delta}^{00}(y) &= e^{-2y}(0.0534451 - 0.0755325y)
\end{aligned}
$$

Oxygen (^{16}O)

$$
\begin{aligned}
W_{M}^{00}(y) &= 0.000032628e^{-2y}(395.084 - 200.042y + y^2)^2 \\
W_{\Phi''}^{00}(y) &= 0.000032628e^{-2y}(3.66055 - y)^2 \\
W_{M\Phi''}^{00}(y) &= e^{-2y}(-0.0471874 + 0.0367831y - 0.00664641y^2 + 0.000032628y^3)
\end{aligned}
$$

Fluorine (^{19}F)

$$
\begin{aligned}
W_{M}^{pp}(y) &= e^{-2y}(81. - 96.y + 36.y^2 - 4.7y^3 + 0.19y^4)\\
W_{M}^{nn}(y) &= e^{-2y}(100. - 130.y + 61.y^2 - 11.y^3 + 0.73y^4)\\
W_{M}^{np}(y) &= e^{-2y}(90. - 110.y + 48.y^2 - 7.5y^3 + 0.37y^4)\\
W_{M}^{pn}(y) &= e^{-2y}(90. - 110.y + 48.y^2 - 7.5y^3 + 0.37y^4)\\
W_{\Sigma''}^{pp}(y) &= e^{-2y}(0.903 - 2.37y + 2.35y^2 - 1.05y^3 + 0.175y^4)\\
W_{\Sigma''}^{nn}(y) &= e^{-2y}(0.000303 - 0.00107y + 0.00114y^2 - 0.000348y^3 + 0.0000320y^4)\\
W_{\Sigma''}^{np}(y) &= e^{-2y}(-0.0166 + 0.0509y - 0.0510y^2 + 0.0199y^3 - 0.00237y^4)\\
W_{\Sigma''}^{np}(y) &= e^{-2y}(-0.0166 + 0.0509y - 0.0510y^2 + 0.0199y^3 - 0.00237y^4)\\
W_{\Sigma'}^{pp}(y) &= e^{-2y}(1.81 - 4.85y + 4.88y^2 - 2.18y^3 + 0.364y^4)\\
W_{\Sigma'}^{nn}(y) &= e^{-2y}(0.000607 - 0.00136y + 0.000266y^2 + 0.000550y^3 + 0.0000997y^4)\\
W_{\Sigma'}^{np}(y) &= e^{-2y}(-0.0331 + 0.0815y - 0.0511y^2 - 0.00142y^3 + 0.00602y^4)\\
W_{\Sigma'}^{pn}(y) &= e^{-2y}(-0.0331 + 0.0815y - 0.0511y^2 - 0.00142y^3 + 0.00602y^4)\\
W_{\Phi''}^{pp}(y) &= e^{-2y}(0.0392 - 0.0314y + 0.00627y^2)\\
W_{\Phi''}^{nn}(y) &= e^{-2y}(0.255 - 0.204y + 0.0408y^2)\\
W_{\Phi''}^{np}(y) &= e^{-2y}(100 - 0.0800y + 0.0160y^2)\\
W_{\Phi''}^{pn}(y) &= e^{-2y}(0251 - 0.0800y + 0.0160y^2)\\
W_{\Delta}^{pp}(y) &= e^{-2y}(0.0335711 - 0.0201y + 0.00401y^2)\\
W_{\Delta}^{nn}(y) &= e^{-2y}(0.0181 - 0.0145y + 0.00290y^2)\\
W_{\Delta}^{np}(y) &= e^{-2y}(-0.0213 + 0.0170y - 0.00341y^2)\\
W_{\Delta}^{pn}(y) &= e^{-2y}(-0.0213 + 0.0170y - 0.00341y^2)\\
W_{M\Phi''}^{pp}(y) &= e^{-2y}(-1.78 + 1.77y - 0.509y^2 + 0.0347y^3)\\
W_{M\Phi''}^{nn}(y) &= e^{-2y}(-5.05 + 5.39y - 1.78y^2 + 0.172y^3)\\
W_{M\Phi''}^{np}(y) &= e^{-2y}(-1.98 + 2.11y - 0.697y^2 + 0.0675y^3)\\
W_{M\Phi''}^{pn}(y) &= e^{-2y}(-4.55 + 4.51y - 1.30y^2 + 0.0884y^3)\\
W_{\Sigma'\Delta}^{pp}(y) &= e^{-2y}(-0.213 + 0.371y - 0.210y^2 + 0.0382y^3)\\
W_{\Sigma'\Delta}^{nn}(y) &= e^{-2y}(-0.00331 + 0.00503y - 0.000138y^2 + 0.000537y^3)\\
W_{\Sigma'\Delta}^{np}(y) &= e^{-2y}(0.00390 - 0.00592y + 0.000163y^2 + 0.000632y^3)\\
W_{\Sigma'\Delta}^{pn}(y) &= e^{-2y}(0.181 - 0.315y + 0.178y^2 - 0.0325y^3)
\end{aligned}
$$

Neon (^{20}Ne)

$$\begin{aligned}
W_M^{00}(y) &= 0.0431723e^{-2y}(13.5766 - 9.05108y + y^2)^2\\
W_{\Phi''}^{00}(y) &= 0.00348077e^{-2y}(2.50001 - y)^2\\
W_{M\Phi''}^{00}(y) &= e^{-2y}(-0.416077 + 0.443815y - 0.1416y^2 + 0.0122586y^3)
\end{aligned}$$

Magnesium (^{24}Mg)

$$\begin{aligned}
W_M^{00}(y) &= 0.123467e^{-2y}(9.63385 - 7.49299y + y^2)^2\\
W_{\Phi''}^{00}(y) &= 0.0260816e^{-2y}(2.5 - y)^2\\
W_{M\Phi''}^{00}(y) &= e^{-2y}(-1.36673 + 1.6097y - 0.567072y^2 + 0.056747y^3)
\end{aligned}$$

Sodium (^{23}Na)

$$W_M^{00}(y) = e^{-2y}(42.0965 - 63.4498y + 32.5913y^2 - 6.57878y^3 + 0.483166y^4)$$

$$W_M^{11}(y) = e^{-2y}(0.0795776 - 0.212207y + 0.182941y^2 - 0.0543892y^3 + 0.00523012y^4)$$

$$W_M^{10}(y) = e^{-2y}(-1.83028 + 3.81972y - 2.50445y^2 + 0.597822y^3 - 0.04545y^4)$$

$$W_M^{01}(y) = e^{-2y}(-1.83028 + 3.81972y - 2.50445y^2 + 0.597822y^3 - 0.04545y^4)$$

$$W_{\Sigma''}^{00}(y) = e^{-2y}(0.0126672 - 0.0262533y + 0.0401886y^2 - 0.010514y^3 + 0.00078605y^4)$$

$$W_{\Sigma''}^{11}(y) = e^{-2y}(0.00917577 - 0.0167053y + 0.0332751y^2 - 0.00765719y^3 + 0.000597676y^4)$$

$$W_{\Sigma''}^{10}(y) = e^{-2y}(0.0107811 - 0.020986y + 0.0360971y^2 - 0.00876213y^3 + 0.000626718y^4)$$

$$W_{\Sigma''}^{01}(y) = e^{-2y}(0.0107811 - 0.020986y + 0.0360971y^2 - 0.00876213y^3 + 0.000626718y^4)$$

$$W_{\Sigma'}^{00}(y) = e^{-2y}(0.0253345 - 0.0750847y + 0.100235y^2 - 0.0384261y^3 + 0.00466396y^4)$$

$$W_{\Sigma'}^{11}(y) = e^{-2y}(0.0183515 - 0.0567009y + 0.0887794y^2 - 0.0374699y^3 + 0.00477955y^4)$$

$$W_{\Sigma'}^{10}(y) = e^{-2y}(0.0215622 - 0.0652627y + 0.0941439y^2 - 0.0379511y^3 + 0.00472138y^4)$$

$$W_{\Sigma'}^{01}(y) = e^{-2y}(0.0215622 - 0.0652627y + 0.0941439y^2 - 0.0379511y^3 + 0.00472138y^4)$$

$$W_{\Phi''}^{00}(y) = e^{-2y}(0.612149 - 0.49308y + 0.107832y^2)$$

$$W_{\Phi''}^{11}(y) = e^{-2y}(0.00940911 - 0.00747826y + 0.00163204y^2)$$

$$W_{\Phi''}^{10}(y) = e^{-2y}(-0.075893 + 0.060682y - 0.0110124y^2)$$

$$W_{\Phi''}^{01}(y) = e^{-2y}(-0.075893 + 0.060682y - 0.0110124y^2)$$

$$
\begin{aligned}
W^{00}_{\tilde{\Phi}''}(y) &= e^{-2y}(0.000495589 - 0.00010394y + 0.00000544981y^2)\\
W^{11}_{\tilde{\Phi}''}(y) &= e^{-2y}(0.00000616583 + 0.00008381y + 0.0002848y^2)\\
W^{10}_{\tilde{\Phi}''}(y) &= e^{-2y}(-0.0000552785 - 0.000369894y + 0.0000393968y^2)\\
W^{01}_{\tilde{\Phi}''}(y) &= e^{-2y}(-0.0000552785 - 0.000369894y + 0.0000393968y^2)\\
W^{00}_{\Delta}(y) &= e^{-2y}(0.0335711 - 0.0268568y + 0.00656896y^2)\\
W^{11}_{\Delta}(y) &= e^{-2y}(0.00772326 - 0.00617861y + 0.0021619y^2)\\
W^{10}_{\Delta}(y) &= e^{-2y}(0.0161021 - 0.0128817y + 0.00362952y^2)\\
W^{01}_{\Delta}(y) &= e^{-2y}(0.0161021 - 0.0128817y + 0.00362952y^2)\\
W^{00}_{M\Phi''}(y) &= e^{-2y}(-5.07498 + 5.86765y - 2.09908y^2 + 0.226345y^3)\\
W^{11}_{M\Phi''}(y) &= e^{-2y}(-0.0273574 + 0.0474719y - 0.0213121y^2 + 0.00280825y^3)\\
W^{10}_{M\Phi''}(y) &= e^{-2y}(0.220651 - 0.382932y + 0.17682y^2 - 0.0226015y^3)\\
W^{01}_{M\Phi''}(y) &= e^{-2y}(0.62922 - 0.727336y + 0.243236y^2 - 0.0210943y^3)\\
W^{00}_{\Sigma'\Delta}(y) &= e^{-2y}(-0.0291634 + 0.0548817y - 0.0305345y^2 + 0.00476387y^3)\\
W^{11}_{\Sigma'\Delta}(y) &= e^{-2y}(-0.0119052 + 0.0231539y - 0.0164035y^2 + 0.00310235y^3)\\
W^{10}_{\Sigma'\Delta}(y) &= e^{-2y}(-0.024821 + 0.0482732y - 0.02884y^2 + 0.00481368y^3)\\
W^{01}_{\Sigma'\Delta}(y) &= e^{-2y}(-0.013988 + 0.0263236y - 0.0171362y^2 + 0.00306717y^3)
\end{aligned}
$$

Aluminium (^{27}Al)

$$W_M^{00}(y) = e^{-2y}(87.0146 - 146.097y + 83.5367y^2 - 18.5981y^3 + 1.43446y^4)$$

$$W_M^{11}(y) = e^{-2y}(0.119366 - 0.31831y + 0.337291y^2 - 0.132526y^3 + 0.018155y^4)$$

$$W_M^{10}(y) = e^{-2y}(-3.22283 + 7.00266y - 4.92756y^2 + 1.33587y^3 - 0.11524y^4)$$

$$W_M^{01}(y) = e^{-2y}(-3.22283 + 7.00266y - 4.92756y^2 + 1.33587y^3 - 0.11524y^4)$$

$$W_{\Sigma''}^{00}(y) = e^{-2y}(0.0309465 - 0.0367242y + 0.0265347y^2 - 0.00241606y^3 + 0.0110011y^4)$$

$$W_{\Sigma''}^{11}(y) = e^{-2y}(0.0218834 - 0.00944476y + 0.011506y^2 + 0.000953537y^3 + 0.0104813y^4)$$

$$W_{\Sigma''}^{10}(y) = e^{-2y}(0.0260233 - 0.0210567y + 0.0158643y^2 + 0.000606077y^3 + 0.0105713y^4)$$

$$W_{\Sigma''}^{01}(y) = e^{-2y}(0.0260233 - 0.0210567y + 0.0158643y^2 + 0.000606077y^3 + 0.0105713y^4)$$

$$W_{\Sigma'}^{00}(y) = e^{-2y}(0.0618929 - 0.210848y + 0.244466y^2 - 0.0942682y^3 + 0.0243737y^4)$$

$$W_{\Sigma'}^{11}(y) = e^{-2y}(0.0437667 - 0.165622y + 0.221193y^2 - 0.101991y^3 + 0.0277477y^4)$$

$$W_{\Sigma'}^{10}(y) = e^{-2y}(0.0520466 - 0.18713y + 0.233007y^2 - 0.0985082y^3 + 0.0259327y^4)$$

$$W_{\Sigma'}^{01}(y) = e^{-2y}(0.0520466 - 0.18713y + 0.233007y^2 - 0.0985082y^3 + 0.0259327y^4)$$

$$W_{\Phi''}^{00}(y) = e^{-2y}(2.80498 - 2.24306y + 0.455491y^2)$$

$$W_{\Phi''}^{11}(y) = e^{-2y}(0.021493 - 0.0156159y + 0.00596886y^2)$$

$$W_{\Phi''}^{10}(y) = e^{-2y}(-0.180417 + 0.137389y - 0.0239615y^2)$$

$$W_{\Phi''}^{01}(y) = e^{-2y}(-0.180417 + 0.137389y - 0.0239615y^2)$$

Xenon (^{128}Xe)

$W_M^{pp}(y) = e^{-2y}(2900. - 11000.y + 15000.y^2 - 11000y^3 + 4200y^4 - 950.y^5 + 120.y^6 - 7.8y^7 + 0.20y^8)$

$W_M^{nn}(y) = e^{-2y}(5500. - 23000.y + 38000.y^2 - 32000.y^3 + 16000.y^4 - 4600.y^5 + 790.y^6 - 75.y^7 + 3.3y^8 - 0.041y^9 + 0.00015y^{10})$

$W_M^{np}(y) = e^{-2y}(4000. - 15000.y + 24000.y^2 - 19000.y^3 + 8300.y^4 - 2100.y^5 + 320.y^6 - 25.y^7 + 0.85y^8 - 0.0055y^9)$

$W_M^{pn}(y) = e^{-2y}(4000. - 15000.y + 24000.y^2 - 19000.y^3 + 8300.y^4 - 2100.y^5 + 320.y^6 - 25.y^7 + 0.85y^8 - 0.0055y^9)$

$W_{\Phi''}^{pp}(y) = e^{-2y}(180. - 440.y + 410.y^2 - 180.y^3 + 42.y^4 - 4.9y^5 + 0.22y^6)$

$W_{\Phi''}^{nn}(y) = e^{-2y}(44. - 140.y + 170.y^2 - 110.y^3 + 36.y^4 - 6.8y^5 + 0.74y^6 - 0.042y^7 + 0.00095y^8)$

$W_{\Phi''}^{np}(y) = e^{-2y}(91. - 250.y + 270.y^2 - 140.y^3 + 40.y^4 - 6.2y^5 + 0.48y^6 - 0.014y^7)$

$W_{\Phi''}^{pn}(y) = e^{-2y}(91. - 250.y + 270.y^2 - 140.y^3 + 40.y^4 - 6.2y^5 + 0.48y^6 - 0.014y^7)$

$W_{M\Phi''}^{pp}(y) = e^{-2y}(-730. + 2200.y - 2500.y^2 + 1500.y^3 - 450.y^4 + 76.y^5 - 6.4y^6 + 0.21y^7)$

$W_{M\Phi''}^{nn}(y) = e^{-2y}(-490. + 1800.y - 2600.y^2 + 1900.y^3 - 780.y^4 + 190.y^5 - 25.y^6 + 1.9y^7 - 0.060y^8 + 0.00038y^9)$

$W_{M\Phi''}^{np}(y) = e^{-2y}(-1000. + 3300.y - 4200.y^2 + 2700.y^3 - 940.y^4 + 180.y^5 - 19.y^6 + 0.85y^7 - 0.0058y^8)$

$W_{M\Phi''}^{pn}(y) = e^{-2y}(-360. + 1200.y - 1600.y^2 + 1100.y^3 - 390.y^4 + 81.y^5 - 9.5y^6 + 0.57y^7 - 0.014y^8)$

Xenon (^{129}Xe)

$$W_M^{pp}(y) = e^{-2y}(2900. - 11000.y + 15000.y^2 - 10000y^3 + 3900y^4 - 840.y^5 + 98.y^6 - 5.6y^7 + 0.12y^8)$$

$$W_M^{nn}(y) = e^{-2y}(5600. - 24000.y + 39000.y^2 - 34000.y^3 + 17000.y^4 - 4900.y^5 + 850.y^6 - 82.y^7 + 3.9y^8 - 0.065y^9 + 0.00034y^{10})$$

$$W_M^{np}(y) = e^{-2y}(4000. - 16000.y + 24000.y^2 - 19000.y^3 + 8200.y^4 - 2100.y^5 + 300.y^6 - 23.y^7 + 0.77y^8 - 0.0065y^9)$$

$$W_M^{pn}(y) = e^{-2y}(4000. - 16000.y + 24000.y^2 - 19000.y^3 + 8200.y^4 - 2100.y^5 + 300.y^6 - 23.y^7 + 0.77y^8 - 0.0065y^9)$$

$$W_{\Sigma''}^{pp}(y) = e^{-2y}(0.00021 - 0.0015y + 0.0043y^2 - 0.0063y^3 + 0.0049y^4 - 0.0020y^5 + 0.00042y^6)$$

$$W_{\Sigma''}^{nn}(y) = e^{-2y}(0.25 - 0.84y + 1.4y^2 - 1.5y^3 + 0.94y^4 - 0.37y^5 + 0.089y^6 - 0.012y^7 + 0.00076y^8)$$

$$W_{\Sigma''}^{np}(y) = e^{-2y}(0.0072 - 0.038y + 0.082y^2 - 0.097y^3 + 0.068y^4 - 0.027y^5 + 0.0061y^6 - 0.00073y^7)$$

$$W_{\Sigma''}^{np}(y) = e^{-2y}(0.0072 - 0.038y + 0.082y^2 - 0.097y^3 + 0.068y^4 - 0.027y^5 + 0.0061y^6 - 0.00073y^7)$$

$$W_{\Sigma'}^{pp}(y) = e^{-2y}(0.00042 - 0.0019y + 0.0065y^2 - 0.012y^3 + 0.017y^4 - 0.012y^5 + 0.0041y^6 - 0.00063y^7)$$

$$W_{\Sigma'}^{nn}(y) = e^{-2y}(0.49 - 3.3y + 8.8y^2 - 12.y^3 + 9.8y^4 - 4.5y^5 + 1.2y^6 - 0.16y^7 + 0.010y^8)$$

$$W_{\Sigma'}^{np}(y) = e^{-2y}(0.014 - 0.080y + 0.23y^2 - 0.41y^3 + 0.43y^4 - 0.24y^5 + 0.070y^6 - 0.010y^7 + 0.00058y^8)$$

$$W_{\Sigma'}^{pn}(y) = e^{-2y}(0.014 - 0.080y + 0.23y^2 - 0.41y^3 + 0.43y^4 - 0.24y^5 + 0.070y^6 - 0.010y^7 + 0.00058y^8)$$

$$W_{\Phi''}^{pp}(y) = e^{-2y}(130. - 300.y + 280.y^2 - 130.y^3 + 30.y^4 - 3.5y^5 + 0.16y^6)$$

$$W_{\Phi''}^{nn}(y) = e^{-2y}(120. - 360.y + 440.y^2 - 270.y^3 + 93.y^4 - 18.y^5 + 1.9y^6 - 0.10y^7 + 0.0021y^8)$$

$$W_{\Phi''}^{np}(y) = e^{-2y}(120. - 330.y + 360.y^2 - 190.y^3 + 55.y^4 - 8.4y^5 + 0.64y^6 - 0.019y^7)$$

$$W_{\Phi''}^{pn}(y) = e^{-2y}(120. - 330.y + 360.y^2 - 190.y^3 + 55.y^4 - 8.4y^5 + 0.64y^6 - 0.019y^7)$$

$$W_{\Delta}^{pp}(y) = e^{-2y}(0.038 - 0.090y + 0.091y^2 - 0.048y^3 + 0.014y^4 - 0.0021y^5 + 0.00012y^6)$$

$$W_{\Delta}^{nn}(y) = e^{-2y}(0.00046 + 0.0038y + 0.0091y^2 + 0.0054y^3 - 0.00062y^5)$$

$$W_{\Delta}^{np}(y) = e^{-2y}(-0.0041 - 0.012y + 0.012y^2 + 0.00056y^3 - 0.0032y^4 + 0.00062y^5)$$

$$W_{\Delta}^{pn}(y) = e^{-2y}(-0.0041 - 0.012y + 0.012y^2 + 0.00056y^3 - 0.0032y^4 + 0.00062y^5)$$

$$W_{M\Phi''}^{pp}(y) = e^{-2y}(-610. + 1800.y - 2100.y^2 + 1200.y^3 - 360.y^4 + 59.y^5 - 4.8y^6 + 0.14y^7)$$

$$W_{M\Phi''}^{nn}(y) = e^{-2y}(-800. + 3000.y - 4300.y^2 + 3100.y^3 - 1300.y^4 + 310.y^5 - 42.y^6 + 3.1y^7 - 0.10y^8 + 0.00085y^9)$$

$$W_{M\Phi''}^{np}(y) = e^{-2y}(-840. + 2800.y - 3500.y^2 + 2300.y^3 - 810.y^4 + 160.y^5 - 17.y^6 + 0.78y^7 - 0.0074y^8)$$

$$W_{M\Phi''}^{pn}(y) = e^{-2y}(-580. + 2000.y - 2600.y^2 + 1700.y^3 - 600.y^4 + 120.y^5 - 14.y^6 + 0.76y^7 - 0.014y^8)$$

$$W_{\Sigma'\Delta}^{pp}(y) = e^{-2y}(-0.0040 + 0.014y - 0.033y^2 + 0.040y^3 - 0.024y^4 + 0.0076y^5 - 0.0011y^6)$$

$$W_{\Sigma'\Delta}^{nn}(y) = e^{-2y}(0.015 + 0.012y - 0.13y^2 + 0.11y^3 + 0.018y^4 - 0.030y^5 + 0.0050y^6 + 0.00051y^7 - 0.00012y^8)$$

$$W_{\Sigma'\Delta}^{np}(y) = e^{-2y}(-0.14 + 0.61y - 1.1y^2 + 0.95y^3 - 0.47y^4 + 0.13y^5 - 0.019y^6 + 0.0011y^7)$$

$$W_{\Sigma'\Delta}^{pn}(y) = e^{-2y}(0.00044 + 0.00083y - 0.0010y^2 + 0.0067y^3 - 0.00090y^4 - 0.0018y^5 + 0.00037y^6)$$

Xenon (^{130}Xe)

$$W_M^{pp}(y) = e^{-2y}(2900. - 11000.y + 15000.y^2 - 11000y^3 + 4100y^4 - 910.y^5 + 110.y^6 - 7.y^7 + 0.17y^8)$$

$$W_M^{nn}(y) = e^{-2y}(5800. - 24000.y + 41000.y^2 - 36000.y^3 + 18000.y^4 - 5200.y^5 + 910.y^6 - 89.y^7 + 4.2y^8 - 0.068y^9 + 0.00034y^{10})$$

$$W_M^{np}(y) = e^{-2y}(4100. - 16000.y + 25000.y^2 - 19000.y^3 + 8600.y^4 - 2200.y^5 + 330.y^6 - 26.y^7 + 0.91y^8 - 0.0076y^9)$$

$$W_M^{pn}(y) = e^{-2y}(4100. - 16000.y + 25000.y^2 - 19000.y^3 + 8600.y^4 - 2200.y^5 + 330.y^6 - 26.y^7 + 0.91y^8 - 0.0076y^9)$$

$$W_{\Phi''}^{pp}(y) = e^{-2y}(150. - 370.y + 330.y^2 - 150.y^3 + 34.y^4 - 3.8y^5 + 0.17y^6)$$

$$W_{\Phi''}^{nn}(y) = e^{-2y}(100. - 320.y + 390.y^2 - 240.y^3 + 80.y^4 - 15.y^5 + 1.7y^6 - 0.094y^7 + 0.0021y^8)$$

$$W_{\Phi''}^{np}(y) = e^{-2y}(120. - 350.y + 370.y^2 - 190.y^3 + 54.y^4 - 8.2y^5 + 0.63y^6 - 0.019y^7)$$

$$W_{\Phi''}^{pn}(y) = e^{-2y}(120. - 350.y + 370.y^2 - 190.y^3 + 54.y^4 - 8.2y^5 + 0.63y^6 - 0.019y^7)$$

$$W_{M\Phi''}^{pp}(y) = e^{-2y}(-670. + 2000.y - 2300.y^2 + 1300.y^3 - 400.y^4 + 65.y^5 - 5.4y^6 + 0.17y^7)$$

$$W_{M\Phi''}^{nn}(y) = e^{-2y}(-760. + 2800.y - 4100.y^2 + 3000.y^3 - 1200.y^4 - 300.y^5 - 41.y^6 + 3.1y^7 - 0.10y^8 + 0.00085y^9)$$

$$W_{M\Phi''}^{np}(y) = e^{-2y}(-940. + 3100.y - 4000.y^2 + 2500.y^3 - 900.y^4 + 180.y^5 - 18.y^6 + 0.84y^7 - 0.0075y^8)$$

$$W_{M\Phi''}^{pn}(y) = e^{-2y}(-540. + 1800.y - 2400.y^2 + 1600.y^3 - 580.y^4 + 120.y^5 - 14.y^6 + 0.81y^7 - 0.019y^8)$$

Xenon (^{131}Xe)

$$W_M^{pp}(y) = e^{-2y}(2900. - 11000.y + 15000.y^2 - 10000y^3 + 3800y^4 - 810.y^5 + 92.y^6 - 5.1y^7 + 0.11y^8)$$

$$W_M^{nn}(y) = e^{-2y}(5900. - 25000.y + 43000.y^2 - 37000.y^3 + 19000.y^4 - 5500.y^5 + 980.y^6 - 97.y^7 + 4.9y^8 - 0.096y^9 + 0.00061y^{10})$$

$$W_M^{np}(y) = e^{-2y}(4200. - 16000.y + 25000.y^2 - 20000.y^3 + 8600.y^4 - 2200.y^5 + 310.y^6 - 24.y^7 + 0.83y^8 - 0.0082y^9)$$

$$W_M^{pn}(y) = e^{-2y}(4200. - 16000.y + 25000.y^2 - 20000.y^3 + 8600.y^4 - 2200.y^5 + 310.y^6 - 24.y^7 + 0.83y^8 - 0.0082y^9)$$

$$W_{\Sigma''}^{pp}(y) = e^{-2y}(0.00013y^2 - 0.00062y^3 + 0.00088y^4 - 0.00053y^5 + 0.00015y^6)$$

$$W_{\Sigma''}^{nn}(y) = e^{-2y}(0.088 + 0.30y - 0.23y^2 - 0.47y^3 + 1.2y^4 - 1.1y^5 + 0.44y^6 - 0.086y^7 + 0.0067y^8)$$

$$W_{\Sigma''}^{np}(y) = e^{-2y}(0.0023 + 0.0032y - 0.011y^2 - 0.00077y^3 + 0.019y^4 - 0.018y^5 + 0.0066y^6 - 0.0011y^7)$$

$$W_{\Sigma''}^{np}(y) = e^{-2y}(0.0023 + 0.0032y - 0.011y^2 - 0.00077y^3 + 0.019y^4 - 0.018y^5 + 0.0066y^6 - 0.0011y^7)$$

$$W_{\Sigma'}^{pp}(y) = e^{-2y}(0.00012 - 0.00089y + 0.0015y^2 + 0.0015y^3 - 0.00069y^4 - 0.0012y^5 + 0.00080y^6 - 0.00016y^7)$$

$$W_{\Sigma'}^{nn}(y) = e^{-2y}(0.18 - 1.6y + 5.8y^2 - 9.7y^3 + 9.1y^4 - 4.9y^5 + 1.4y^6 - 0.21y^7 + 0.012y^8)$$

$$W_{\Sigma'}^{np}(y) = e^{-2y}(0.0045 - 0.039y + 0.095y^2 - 0.038y^3 - 0.077y^4 + 0.087y^5 - 0.035y^6 + 0.0059y^7 - 0.00035y^8)$$

$$W_{\Sigma'}^{pn}(y) = e^{-2y}(0.0045 - 0.039y + 0.095y^2 - 0.038y^3 - 0.077y^4 + 0.087y^5 - 0.035y^6 + 0.0059y^7 - 0.00035y^8)$$

$$W_{\Phi''}^{pp}(y) = e^{-2y}(130. - 300.y + 280.y^2 - 130.y^3 + 30.y^4 - 3.5y^5 + 0.16y^6)$$

$$W_{\Phi''}^{nn}(y) = e^{-2y}(120. - 360.y + 440.y^2 - 270.y^3 + 93.y^4 - 18.y^5 + 1.9y^6 - 0.10y^7 + 0.0021y^8)$$

$$W_{\Phi''}^{np}(y) = e^{-2y}(120. - 330.y + 360.y^2 - 190.y^3 + 55.y^4 - 8.4y^5 + 0.64y^6 - 0.019y^7)$$

$$W_{\Phi''}^{pn}(y) = e^{-2y}(120. - 330.y + 360.y^2 - 190.y^3 + 55.y^4 - 8.4y^5 + 0.64y^6 - 0.019y^7)$$

$$W^{pp}_{\Delta}(y) = e^{-2y}(0.022 - 0.054y + 0.053y^2 - 0.026y^3 + 0.0071y^4 - 0.00098y^5 + 0.00012y^6)$$

$$W^{nn}_{\Delta}(y) = e^{-2y}(0.56 - 1.4y + 1.8y^2 - 1.3y^3 + 0.51y^4 - 0.11y^5 + 0.0097y^6 - 0.00015y^7)$$

$$W^{np}_{\Delta}(y) = e^{-2y}(0.11 - 0.28y + 0.31y^2 - 0.19y^3 + 0.062y^4 - 0.010y^5 + 0.00073y^6)$$

$$W^{pn}_{\Delta}(y) = e^{-2y}(0.11 - 0.28y + 0.31y^2 - 0.19y^3 + 0.062y^4 - 0.010y^5 + 0.00073y^6)$$

$$W^{pp}_{M\Phi''}(y) = e^{-2y}(-550. + 1700.y - 1900.y^2 + 1100.y^3 - 320.y^4 + 51.y^5 - 4.0y^6 + 0.11y^7)$$

$$W^{nn}_{M\Phi''}(y) = e^{-2y}(-1100. + 4100.y - 5900.y^2 + 4400.y^3 - 1800.y^4 + 440.y^5 - 61.y^6 + 4.5y^7 - 0.16y^8 + 0.0015y^9)$$

$$W^{np}_{M\Phi''}(y) = e^{-2y}(-790. + 2600.y - 3400.y^2 + 2200.y^3 - 770.y^4 + 150.y^5 - 16.y^6 + 0.77y^7 - 0.0086y^8)$$

$$W^{pn}_{M\Phi''}(y) = e^{-2y}(-770. + 2600.y - 3400.y^2 + 2200.y^3 - 790.y^4 + 160.y^5 - 17.y^6 + 0.96y^7 - 0.021y^8)$$

$$W^{pp}_{\Sigma'\Delta}(y) = e^{-2y}(0.0016 - 0.0081y + 0.0047y^2 + 0.0049y^3 - 0.0061y^4 + 0.0023y^5 - 0.00039y^6)$$

$$W^{nn}_{\Sigma'\Delta}(y) = e^{-2y}(0.31 - 1.9y + 3.8y^2 - 4.1y^3 + 2.5y^4 - 0.87y^5 + 0.15y^6 - 0.011y^7)$$

$$W^{np}_{\Sigma'\Delta}(y) = e^{-2y}(0.063 - 0.37y + 0.72y^2 - 0.68y^3 + 0.35y^4 - 0.098y^5 + 0.014y^6 - 0.00077y^7)$$

$$W^{pn}_{\Sigma'\Delta}(y) = e^{-2y}(0.0080 - 0.041y + 0.027y^2 + 0.020y^3 - 0.038y^4 + 0.020y^5 - 0.0042y^6 + 0.00032y^7)$$

Xenon (^{132}Xe)

$$W_{M}^{pp}(y) = e^{-2y}(2900. - 11000.y + 15000.y^2 - 10000y^3 + 4000y^4 - 880.y^5 + 110.y^6 - 6.4y^7 + 0.15y^8)$$

$$W_{M}^{nn}(y) = e^{-2y}(6100. - 26000.y + 44000.y^2 - 39000.y^3 + 20000.y^4 - 5900.y^5 + 1000.y^6 - 100.y^7 + 5.3y^8 - 0.099y^9 + 0.00061y^{10})$$

$$W_{M}^{np}(y) = e^{-2y}(4200. - 17000.y + 26000.y^2 - 20000.y^3 + 9000.y^4 - 2300.y^5 + 340.y^6 - 27.y^7 + 0.98y^8 - 0.0095y^9)$$

$$W_{M}^{pn}(y) = e^{-2y}(4100. - 16000.y + 25000.y^2 - 19000.y^3 + 8600.y^4 - 2200.y^5 + 330.y^6 - 26.y^7 + 0.91y^8 - 0.0076y^9)$$

$$W_{\Phi''}^{pp}(y) = e^{-2y}(6100. - 26000.y + 44000.y^2 - 39000.y^3 + 20000.y^4 - 5900.y^5 + 1000.y^6 - 100.y^7 + 5.3y^8 - 0.099y^9 + 0.00061y^{10})$$

$$W_{\Phi''}^{nn}(y) = e^{-2y}(180. - 570.y + 700.y^2 - 430.y^3 + 140.y^4 - 27.y^5 + 3.y^6 - 0.17y^7 + 0.0038y^8)$$

$$W_{\Phi''}^{np}(y) = e^{-2y}(150. - 430.y + 460.y^2 - 240.y^3 + 67.y^4 - 10.y^5 + 0.77y^6 - 0.023y^7)$$

$$W_{\Phi''}^{pn}(y) = e^{-2y}(150. - 430.y + 460.y^2 - 240.y^3 + 67.y^4 - 10.y^5 + 0.77y^6 - 0.023y^7)$$

$$W_{M\Phi''}^{pp}(y) = e^{-2y}(-620. + 1900.y - 2100.y^2 + 1200.y^3 - 360.y^4 + 59.y^5 - 4.7y^6 + 0.14y^7)$$

$$W_{M\Phi''}^{nn}(y) = e^{-2y}(-1000. + 3900.y - 5700.y^2 + 4200.y^3 - 1700.y^4 - 420.y^5 - 59.y^6 + 4.5y^7 - 0.16y^8 + 0.0015y^9)$$

$$W_{M\Phi''}^{np}(y) = e^{-2y}(-900. + 3000.y - 3800.y^2 + 2500.y^3 - 880.y^4 + 170.y^5 - 18.y^6 + 0.85y^7 - 0.0092y^8)$$

$$W_{M\Phi''}^{pn}(y) = e^{-2y}(-720. + 2400.y - 3200.y^2 + 2100.y^3 - 760.y^4 + 160.y^5 - 18.y^6 + 1.y^7 - 0.024y^8)$$

Xenon (^{134}Xe)

$W_M^{pp}(y) = e^{-2y}(2900. - 11000.y + 15000.y^2 - 10000y^3 + 3700y^4 - 770.y^5 + 85.y^6 - 4.5y^7 + 0.098y^8 - 0.00028y^9)$

$W_M^{nn}(y) = e^{-2y}(6400. - 28000.y + 48000.y^2 - 43000.y^3 + 22000.y^4 - 6600.y^5 + 1200.y^6 - 120.y^7 + 6.6y^8 - 0.15y^9 + 0.0012y^{10})$

$W_M^{np}(y) = e^{-2y}(4300. - 17000.y + 27000.y^2 - 21000.y^3 + 9200.y^4 - 2300.y^5 + 340.y^6 - 26.y^7 + 0.93y^8 - 0.011y^9)$

$W_M^{pn}(y) = e^{-2y}(4300. - 17000.y + 27000.y^2 - 21000.y^3 + 9200.y^4 - 2300.y^5 + 340.y^6 - 26.y^7 + 0.93y^8 - 0.011y^9)$

$W_{\Phi''}^{pp}(y) = e^{-2y}(80. - 190.y + 180.y^2 - 77.y^3 + 17.y^4 - 1.9y^5 + 0.085y^6 - 0.00064y^7)$

$W_{\Phi''}^{nn}(y) = e^{-2y}(380. - 1200.y + 1500.y^2 - 910.y^3 + 310.y^4 - 59.y^5 + 6.3y^6 - 0.35y^7 + 0.0075y^8)$

$W_{\Phi''}^{np}(y) = e^{-2y}(180. - 490.y + 520.y^2 - 270.y^3 + 75.y^4 - 11.y^5 + 0.85y^6 - 0.026y^7)$

$W_{\Phi''}^{pn}(y) = e^{-2y}(180. - 490.y + 520.y^2 - 270.y^3 + 75.y^4 - 11.y^5 + 0.85y^6 - 0.026y^7)$

$W_{M\Phi''}^{pp}(y) = e^{-2y}(-480. + 1500.y - 1700.y^2 + 920.y^3 - 270.y^4 + 41.y^5 - 3.1y^6 + 0.094y^7 - 0.00047y^8)$

$W_{M\Phi''}^{nn}(y) = e^{-2y}(-1600. + 5900.y - 8700.y^2 + 6500.y^3 - 2700.y^4 - 660.y^5 - 92.y^6 + 7.1y^7 - 0.26y^8 + 0.0030y^9)$

$W_{M\Phi''}^{np}(y) = e^{-2y}(-720. + 2400.y - 3100.y^2 + 2000.y^3 - 720.y^4 + 140.y^5 - 15.y^6 + 0.75y^7 - 0.012y^8)$

$W_{M\Phi''}^{pn}(y) = e^{-2y}(-1100. + 3600.y - 4700.y^2 + 3000.y^3 - 1100.y^4 + 210.y^5 - 23.y^6 + 1.3y^7 - 0.027y^8)$

Xenon (^{136}Xe)

$$W_M^{pp}(y) = e^{-2y}(2900. - 11000.y + 15000.y^2 - 10000y^3 + 3700y^4 - 770.y^5 + 85.y^6 - 4.5y^7 + 0.097y^8 - 0.00028y^9)$$

$$W_M^{nn}(y) = e^{-2y}(6700. - 30000.y + 51000.y^2 - 46000.y^3 + 24000.y^4 - 7300.y^5 + 1300.y^6 - 140.y^7 + 7.6y^8 - 0.17y^9 + 0.0014y^{10})$$

$$W_M^{np}(y) = e^{-2y}(4400. - 18000.y + 28000.y^2 - 22000.y^3 + 9700.y^4 - 2500.y^5 + 360.y^6 - 28.y^7 + 1.0y^8 - 0.012y^9)$$

$$W_M^{pn}(y) = e^{-2y}(4400. - 18000.y + 28000.y^2 - 22000.y^3 + 9700.y^4 - 2500.y^5 + 360.y^6 - 28.y^7 + 1.0y^8 - 0.012y^9)$$

$$W_{\Phi''}^{pp}(y) = e^{-2y}(81. - 200.y + 180.y^2 - 78.y^3 + 17.y^4 - 1.9y^5 + 0.088y^6 - 0.00065y^7)$$

$$W_{\Phi''}^{nn}(y) = e^{-2y}(400. - 1200.y + 1600.y^2 - 910.y^3 + 320.y^4 - 62.y^5 + 6.7y^6 - 0.38y^7 + 0.0085y^8)$$

$$W_{\Phi''}^{np}(y) = e^{-2y}(180. - 510.y + 540.y^2 - 280.y^3 + 78.y^4 - 12.y^5 + 0.90y^6 - 0.028y^7 + 0.00011y^8)$$

$$W_{\Phi''}^{pn}(y) = e^{-2y}(180. - 510.y + 540.y^2 - 280.y^3 + 78.y^4 - 12.y^5 + 0.90y^6 - 0.028y^7 + 0.00011y^8)$$

$$W_{M\Phi''}^{pp}(y) = e^{-2y}(-490. + 1500.y - 1700.y^2 + 930.y^3 - 270.y^4 + 42.y^5 - 3.2y^6 + 0.095y^7 - 0.00048y^8)$$

$$W_{M\Phi''}^{nn}(y) = e^{-2y}(-1600. + 6200.y - 9200.y^2 + 6900.y^3 - 2900.y^4 - 710.y^5 - 100.y^6 + 7.8y^7 - 0.29y^8 + 0.0034y^9)$$

$$W_{M\Phi''}^{np}(y) = e^{-2y}(-740. + 2500.y - 3300.y^2 + 2100.y^3 - 760.y^4 + 150.y^5 - 16.y^6 + 0.82y^7 - 0.013y^8)$$

$$W_{M\Phi''}^{pn}(y) = e^{-2y}(-1100. + 3700.y - 4800.y^2 + 3100.y^3 - 1100.y^4 + 220.y^5 - 24.y^6 + 1.3y^7 - 0.029y^8)$$

B

Experimental likelihoods and upper limits

The likelihood-ratio test is defined as

$$\Lambda\left(m_\chi,\, N_\varepsilon^{\rm sig}\right) \;=\; -2\log\left[\frac{\mathcal{L}_\varepsilon\left(m_\chi,\, N_\varepsilon^{\rm sig}\right)}{\mathcal{L}_{\varepsilon,\min}\left(m_\chi,\, N_\varepsilon^{\rm sig}\right)}\right], \tag{B.1}$$

where $\mathcal{L}_\varepsilon\left(m_\chi,\, N_\varepsilon^{\rm sig}\right)$ is the experimental likelihood of the signal + background hypothesis and $\mathcal{L}_{\varepsilon,\min}\left(m_\chi,\, N_\varepsilon^{\rm sig}\right)$ is the minimum of the likelihood function after varying over all parameters. According to Wilks' theorem [154], $\Lambda\left(m_\chi,\, N_\varepsilon^{\rm sig}\right)$ asymptotically converges to a χ^2-distribution, where the significance and degrees of freedom define the difference in dimensionality between $\mathcal{L}_\varepsilon$ and $\mathcal{L}_{\varepsilon,\min}$. In this work, we consider the experiments XENON1T [24], PICO-60 [25, 26] and IceCube [13]. The degrees of freedom of the χ^2 for the single experiment upper limits of XENON1T, PICO-60 (first bin) and IceCube, and their combination of limits is one. In this case, the 90% C.L. upper limit condition is

$$2\log\left[\mathcal{L}_{\varepsilon,\min}\left(m_\chi,\, N_\varepsilon^{\rm sig}\right)\right] \,-\, 2\log\left[\mathcal{L}_\varepsilon\left(m_\chi,\, N_\varepsilon^{\rm sig}\right)\right] \;=\; 2.71. \tag{B.2}$$

Since there are no observed events for PICO-60 (second bin), $\mathcal{L}_{\min}$ is zero for all dark matter masses. In this case, the degrees of freedom are two, and the condition for the 90% C.L. single-experiment upper limits reads

$$-\,2\log\left[\mathcal{L}_\varepsilon\left(m_\chi,\, N_\varepsilon^{\rm sig}\right)\right] \;=\; 4.6. \tag{B.3}$$

Since the likelihoods of the experiments depend on several parameters and are complicated to reproduce, we consider the poissonian likelihood

Experiment	$N_\varepsilon^{\rm obs}$	$N_\varepsilon^{\rm back}$
XENON1T	14	7.36
PICO-60 (first bin)	3	1
PICO-60 (second bin)	0	0
IceCube	926	931
DeepCore	427	414

Table B.1: Number of observed and background events for the considered experiments.

$$\mathcal{L}_\varepsilon\left(N_\varepsilon^{\rm obs}|N_\varepsilon^{\rm sig}+N_\varepsilon^{\rm back}\right)=\frac{\left(N_\varepsilon^{\rm sig}+N_\varepsilon^{\rm back}\right)^{N_\varepsilon^{\rm obs}}}{N_\varepsilon^{\rm obs}!}\,e^{-\left(N_\varepsilon^{\rm sig}+N_\varepsilon^{\rm back}\right)}, \tag{B.4}$$

with the number of predicted signal $N_\varepsilon^{\rm sig}$, observed $N_\varepsilon^{\rm obs}$ and background $N_\varepsilon^{\rm back}$ events.

Taking the logarithm of the likelihood for a given set of n experiments,

$$\mathcal{L}_{\rm tot}=\prod_{\varepsilon=1}^{n}\mathcal{L}_\varepsilon, \tag{B.5}$$

and multiplying by -2, we get

$$-2\log\left[\mathcal{L}_{\rm tot}\right]=2\sum_{\varepsilon=1}^{n}\left[N_\varepsilon^{\rm sig}+N_\varepsilon^{\rm back}-N_\varepsilon^{\rm obs}\log\left(N_\varepsilon^{\rm sig}+N_\varepsilon^{\rm back}\right)+\log\left(N_\varepsilon^{\rm obs}!\right)\right]. \tag{B.6}$$

The numbers of observed and background events for each experiment we take into account are given in Tab. B.1.

C

The solar composition and its impact on the dark matter capture

In this Appendix, we investigate the link between the operator, target properties and the orientation of the allowed parameter space. For demonstration, we choose the solar interior as target. Due to its composition, it can be seen as multiple target experiment and allows an investigation of multiple targets with different properties at the same time.

In the first section, we comment on the commonly used model of the solar interior, AGSS09ph [155], and list the element's properties that are important for the eccentricity of the allowed parameter space. In the second section, we present the allowed parameter space, capture rates and differential cross-sections for the most important elements for each operator and interpret the outcome.

C.1 The solar model AGSS09ph

In the solar model AGSS09ph [155], Serenelli et al. divide the Sun in shells. The width of each shell is $0.00150\,R_\odot$. Here, $R_\odot$ denotes the solar radius for which they assume $6.9598 \times 10^{10}\,\text{cm}$. Further, AGSS09ph provides information about the total mass fraction, temperature, density, pressure, luminosity fraction and the mass fraction of the contained elements for each shell. The elements appearing in AGSS09ph and their relevant nuclear properties are listed in Tab. C.1.

Element	N_p	N_n	J	α_m	α_N	Nuclear shell	p	n
^{1}H	1	0	1/2	0.75144	0.92661	$1s_{1/2}$	↑ ✗	——
^{3}He	2	1	1/2	1.003×10^{-4}	4.123×10^{-5}	$1s_{1/2}$	↑↓ ✓	↑ ✗
^{4}He	2	2	0	0.23484	0.07240	$1s_{1/2}$	↑↓ ✓	↑↓ ✓
^{12}C	6	6	0	2.355×10^{-3}	0.00024	$1s_{1/2}1p_{3/2}$	↑↓ ✓	↑↓ ✓
^{13}C	6	7	1/2	2.782×10^{-5}	2.639×10^{-6}	$1s_{1/2}1p_{3/2}\left(1p_{1/2}\right)$	↑↓ ✓	↑ ✗
^{14}N	7	7	1	6.959×10^{-4}	6.129×10^{-5}	$1s_{1/2}1p_{3/2}1p_{1/2}$	↑ ✗	↑ ✗
^{15}N	7	8	1/2	2.695×10^{-6}	2.215×10^{-7}	$1s_{1/2}1p_{3/2}1p_{1/2}$	↑ ✗	↑↓ ✓
^{16}O	8	8	0	5.779×10^{-3}	0.00045	$1s_{1/2}1p_{3/2}1p_{1/2}$	↑↓ ✓	↑↓ ✓
^{17}O	8	9	5/2	2.862×10^{-6}	2.076×10^{-7}	$1s_{1/2}1p_{3/2}1p_{1/2}\left(1d_{5/2}\right)$	↑↓ ✓	↑ ✗
^{18}O	8	10	0	1.631×10^{-5}	1.117×10^{-6}	$1s_{1/2}1p_{3/2}1p_{1/2}\left(1d_{5/2}\right)$	↑↓ ✓	↑↓ ✗
^{20}Ne	10	10	0	1.281×10^{-3}	7.898×10^{-5}	$1s_{1/2}1p_{3/2}1p_{1/2}1d_{5/2}$	↑↓ ✗	↑↓ ✗
^{23}Na	11	12	3/2	3.049×10^{-5}	1.635×10^{-6}	$1s_{1/2}1p_{3/2}1p_{1/2}1d_{5/2}$	↑ ✗	↑↓ ✗
^{24}Mg	12	12	0	7.384×10^{-4}	3.794×10^{-5}	$1s_{1/2}1p_{3/2}1p_{1/2}1d_{5/2}$	↑↓ ✗	↑↓ ✗
^{27}Al	13	14	5/2	5.803×10^{-5}	2.650×10^{-6}	$1s_{1/2}1p_{3/2}1p_{1/2}1d_{5/2}$	↑ ✗	↑↓ ✓
^{28}Si	14	14	0	6.935×10^{-4}	3.054×10^{-5}	$1s_{1/2}1p_{3/2}1p_{1/2}1d_{5/2}2s_{1/2}$	↑↓ ✗	↑↓ ✗
^{31}P	15	16	1/2	6.076×10^{-6}	2.417×10^{-7}	$1s_{1/2}1p_{3/2}1p_{1/2}1d_{5/2}2s_{1/2}$	↑ ✗	↑↓ ✓
^{32}S	16	16	0	3.226×10^{-4}	1.243×10^{-5}	$1s_{1/2}1p_{3/2}1p_{1/2}1d_{5/2}2s_{1/2}$	↑↓ ✓	↑↓ ✓
^{35}Cl	17	18	3/2	8.555×10^{-6}	3.014×10^{-7}	$1s_{1/2}1p_{3/2}1p_{1/2}1d_{5/2}2s_{1/2}1d_{3/2}$	↑ ✗	↑↓ ✗
^{39}K	19	20	3/2	3.197×10^{-6}	1.011×10^{-7}	$1s_{1/2}1p_{3/2}1p_{1/2}1d_{5/2}2s_{1/2}1d_{3/2}$	↑ ✗	↑↓ ✓
^{40}Ar	18	22	0	6.958×10^{-5}	2.145×10^{-6}	$...1d_{5/2}2s_{1/2}1d_{3/2}\left(1f_{7/2}\right)$	↑↓ ✗	↑↓ ✗
^{40}Ca	20	20	0	6.691×10^{-5}	2.063×10^{-6}	$1s_{1/2}1p_{3/2}1p_{1/2}1d_{5/2}2s_{1/2}1d_{3/2}$	↑↓ ✓	↑↓ ✓
^{45}Sc	21	24	7/2	4.846×10^{-8}	1.328×10^{-9}	$...1d_{5/2}2s_{1/2}1d_{3/2}1f_{7/2}$	↑ ✗	↑↓ ✗
^{48}Ti	22	26	0	3.256×10^{-6}	8.365×10^{-8}	$...1d_{5/2}2s_{1/2}1d_{3/2}1f_{7/2}$	↑↓ ✗	↑↓ ✗
^{51}V	23	28	7/2	3.309×10^{-7}	8.001×10^{-9}	$...1d_{5/2}2s_{1/2}1d_{3/2}1f_{7/2}$	↑ ✗	↑↓ ✓
^{52}Cr	24	28	0	1.732×10^{-5}	4.107×10^{-7}	$...1d_{5/2}2s_{1/2}1d_{3/2}1f_{7/2}$	↑↓ ✗	↑↓ ✓
^{55}Mn	25	30	5/2	1.128×10^{-5}	2.529×10^{-7}	$...1d_{5/2}2s_{1/2}1d_{3/2}1f_{7/2}\left(2p_{3/2}\right)$	↑ ✗	↑↓ ✗
^{56}Fe	26	30	0	1.348×10^{-3}	2.968×10^{-5}	$...1d_{5/2}2s_{1/2}1d_{3/2}1f_{7/2}\left(2p_{3/2}\right)$	↑↓ ✗	↑↓ ✗
^{58}Ni	28	30	0	7.433×10^{-5}	1.580×10^{-6}	$...1d_{5/2}2s_{1/2}1d_{3/2}1f_{7/2}\left(2p_{3/2}\right)$	↑↓ ✓	↑↓ ✗
^{59}Co	27	32	7/2	4.395×10^{-6}	9.186×10^{-8}	$...1d_{5/2}2s_{1/2}1d_{3/2}1f_{7/2}\left(2p_{3/2}\right)$	↑ ✗	↑↓ ✓

Table C.1: In this table, we list all elements contained in the AGSS09ph together with the corresponding number of protons (neutrons) N_p (N_n), nuclear spin J, mass (number) density α_m (α_N), and the nuclear shells which the protons and neutrons occupy. Notice that the latter needs to be treated independently for protons and neutrons. Some of the elements have enough neutrons so that they occupy an additional shell compared to the protons. Those shells are given in brackets. Further we specify the properties for each element for the protons and neutrons having an unpaired nucleon "↑" or only paired nucleons "↑↓". If the element's most outer shell is (not) fully occupied, we mark this with a cross (tick). Some of the rows are shaded in gray. This marks the elements for which no form factor is provided.

C.2 Interpretation of the allowed parameter space

In order to investigate the impact of different elements on the coupling constraints, we present three sets of plots for each interaction operator in this section, in which we show the

(1) $c_i^p - c_i^n$-parameter space (Figs. C.1, C.4, C.7, C.10, C.13, C.16, C.19, C.22, C.25, C.28, C.31, C.34, C.37 and C.40),

(2) capture rate versus dark matter mass (Figs. C.2, C.5, C.8, C.11, C.14, C.17, C.20, C.23, C.26, C.29, C.32, C.35, C.38 and C.41),

(3) differential cross-section versus recoil energy Figs. C.3, C.6, C.9, C.12, C.15, C.18, C.21, C.24, C.27, C.30, C.33, C.36, C.39, C.42.

Before we deal with the specifics of the plots for each operator, we explain the plots and give conclusions applicable for all operators in advance:

(1) **c_i^p-c_i^n-parameter space**

For the *plots displaying the allowed parameter space*, we show the parameter space spanned by c_i^p and c_i^n. The parameter space allowed by IceCube data [13] is depicted as black region, whereas the allowed parameter space for a single isotope is presented as colored region. As will become apparent in the next subsections, the elements we choose are not the same in every plot, since we show the elements that make the most important contribution to the dark matter capture rate for each operator. To create the plots, we assume $m_\chi = 1$ TeV. While the horizontal and vertical black lines are the axes in the c_i^p-c_i^n basis, the diagonal blue lines are the axes in the c_i^0-c_i^1 basis. The results can be transformed into one another using Eq. (3.10).

(2) **Capture rate versus dark matter mass**

For the presentation of a plot of type (1), we have to assume one specific dark matter mass. In order to get an idea of how the importance of the elements changes with the dark matter mass, we also show how the capture rate depends on m_χ for the most important elements for each operator. The presented elements correspond to the ones in the related plots of type (1). In the left (right) panel, we assume that only the coupling c_i^0 (c_i^1) for the single operator $\hat{\mathcal{O}}_i$ is non-zero. The vertical dashed line indicates $m_\chi = 1$ TeV which fits the case presented in plots of type (1).

(3) **Differential cross-section versus recoil energy**

In the upper (lower) panel of the figure, we present the results assuming a scattering in the center (on the surface) of the Sun. For the left (middle) [right] panel, we assume the asymptotic dark matter velocity $v = 0$ (200) [400] km/s. Each of the plots shows colored lines for the relevant elements of the corresponding operator, matching the ones in the plots of type (1) and (2). Note that the thick solid line indicates the range of possible recoil energies for the respective element. The dashed line, on the other hand, shows the general behavior of the curve, however, these recoil energies are not possible for the chosen scattering position and asymptotic dark matter velocity.

The lower limit of the possible recoil energy range comes from the fact that the dark matter particle needs to lose a certain amount of energy such that it can get bound to the Sun. The asymptotic energy of the dark matter particle is

$$E_{\text{asym}} = \frac{1}{2} m_\chi v^2, \tag{C.1}$$

and its energy at distance r to the Sun's center is

$$E(r) = \frac{1}{2} m_\chi w(r)^2, \tag{C.2}$$

where $w(r) = v^2 + v_{\text{esc}}(r)^2$. Dark matter particles with an energy at the scattering position r up to $E_{u.l.} = \frac{1}{2} m_\chi v_{\text{esc}}^2$ can be bound to the Sun. In the special case of $v = 0$, $E_{u.l.}$ coincides with Eq. (C.2), *i.e.* no energy transfer is required to get captured. For plot type (3) this means the lower recoil energy limit in the left panel is 0. For the middle and right panel, we consider $v = 200$ and 400 km/s, respectively, *i.e.* taking Eq. (C.1) into account, we expect the lower recoil energy limit to be larger in the middle than in the left, and largest in the right panel.

The upper limit on the possible recoil energies $E^{\max}$ is of kinematic nature. Applying energy and momentum conservation, we obtain

$$E^{\max} = \frac{1}{2}\beta m_\chi w(r)^2, \tag{C.3}$$

with

$$\beta = \frac{2m_a m_\chi}{(m_a + m_\chi)^2}. \tag{C.4}$$

Note that the dark matter particles can only be captured after a single scattering if $E^{\max} > E_{\text{asym}}$. We see in the related plots that this is sometimes not fulfilled anymore for high asymptotic velocities.

Operator $\hat{\mathcal{O}}_1$

The only interaction that is sensitive to the M-response, and velocity and momentum independent is the one caused by $\hat{\mathcal{O}}_1$, the widely known standard spin-independent interaction.

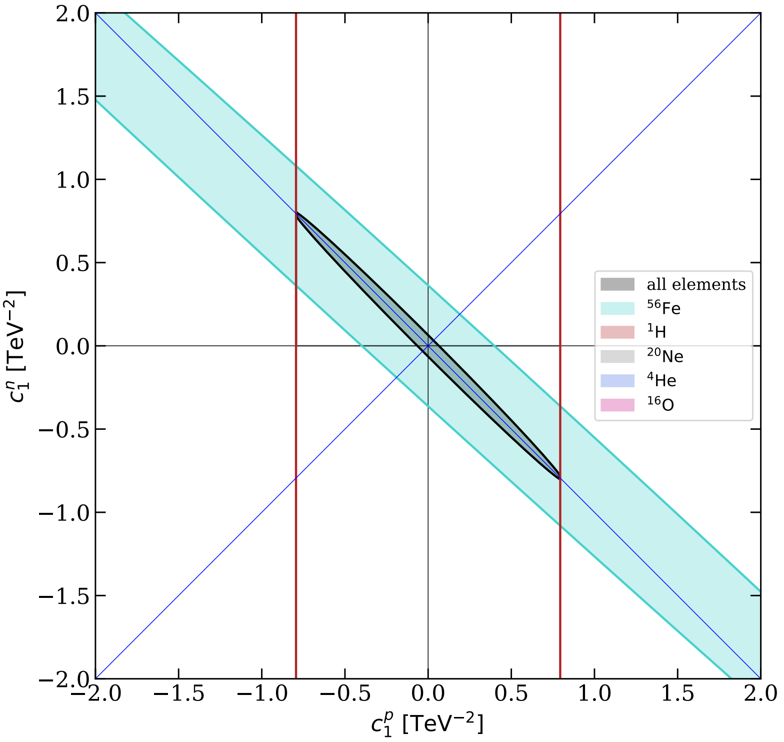

Figure C.1: Allowed parameter space spanned by c_1^p and c_1^n for all elements (black) and for the most important nuclei ^{1}H, ^{56}Fe, ^{16}O, ^{20}Ne and ^{4}He (see legend) for $m_\chi = 1$ TeV.

Using Eq. (3.34), one can very well forecast the eccentricity of the allowed parameter spaces for each kind of nucleus in Fig. C.1, where we show the allowed parameter space for the five most important elements contributing in $\hat{\mathcal{O}}_1$-interactions, which are ^{1}H, ^{4}He ^{16}O, ^{20}Ne, and ^{56}Fe for $m_\chi = 1\,$TeV. While the slope of ^{1}H is infinite, which means that the strip is aligned with the c_1^n-axis, the isoscalar elements ^{4}He ^{16}O and ^{20}Ne have the slope -1 and their corresponding strips are aligned with the c_1^1-axis. The absolute of the slope of the allowed parameter space for ^{56}Fe is slightly smaller than the one

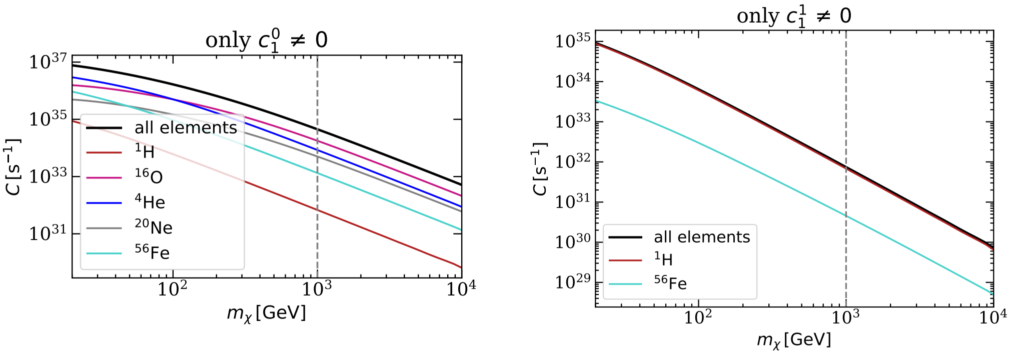

Figure C.2: Dark matter capture rate C versus mass m_χ for all elements (black) and the most important elements (see legend), assuming $c_1^\tau = 1$. *Left panel*: Only c_1^0 is non-zero, *right panel*: Only c_1^1 is non-zero. The dashed vertical line indicates the dark matter mass (1 TeV) assumed in the corresponding plots of type (1).

for isoscalar elements. For this reason, its orientation is similar to the one of isoscalar elements, though slightly rotated counter-clockwise. As mentioned in the previous part, the M-response favors elements with a high nuclear mass number A, such as ^{56}Fe. However the most constraining element for the neutron component is ^{16}O and for the proton component it is ^{1}H. This can be explained by the huge amount of ^{16}O and especially ^{1}H in the Sun, compared to ^{56}Fe.

The importance of the different elements in the whole mass range between 20 GeV and 10 TeV can be seen in Fig. C.2. For $m_\chi \lesssim 100$ GeV the relevance of the elements changes, such that the strongest constraint on the neutron component no longer comes from ^{16}O, but from the lighter element ^{4}He.

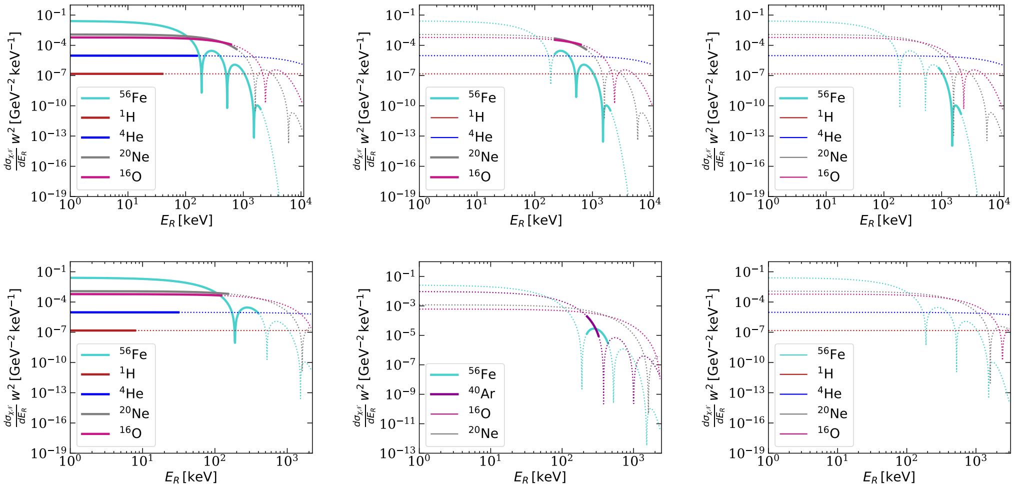

Figure C.3: Differential dark matter-nucleon cross-section $d\sigma_{\chi\mathcal{N}}/dE_R$ × squared dark matter velocity w^2 against recoil energy E_R for operator 1, m_χ = 1 TeV and the most important elements (see legend). *Upper panels* (*lower panels*): Scattering point in the center (on the surface) of the Sun, *left panels* (*middle panels*) [*right panels*]: Asymptotic dark matter velocity $u = 0$ (200) [400] km/s. *Solid* (*dashed*): Possible (Impossible) range of recoil energies.

Operator $\hat{\mathcal{O}}_3$

The relevant responses for operator $\hat{\mathcal{O}}_3$ are Φ'' with q^4-suppression, and Σ' with q^2- and $\left(\mathbf{v}_T^\perp\right)^2$-suppression. As we see in section A, the Φ-response prefers heavy elements with orbits that are not fully occupied. The heaviest elements contained in the Sun (see Tab. C.1) do all fulfill this requirement. However, only ^{56}Fe is present in the Sun at a sufficient amount to significantly contribute to constrain the allowed c_3^p-c_3^n-parameter space as we show in Fig. C.4. Further we can see that an important contribution comes from the isoscalar elements ^{28}Si and ^{32}S. While it is clear that these bands are aligned with the isovector axis due to their isoscalarness, it might be counter-intuitive that ^{28}Si is more constraining than ^{32}S from the Φ''-response point of view, since it is lighter and only has fully occupied orbits. However, this can be explained by the higher amount of ^{28}Si contained in the Sun compared to ^{32}S. Number four of the most important elements is ^{40}Ar which does not anymore take part in constraining the allowed parameter space considering all elements.

In Fig. C.5, we again show the capture rate for the mass range between 20

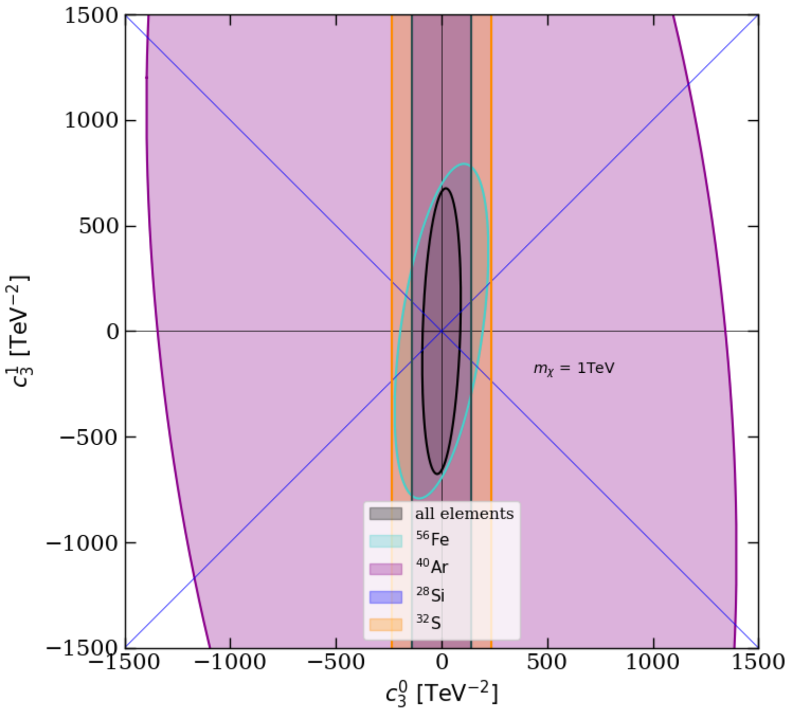

Figure C.4: Allowed parameter space spanned by c_3^0 and c_3^1 for all elements (black) and for the most important nuclei ^{56}Fe, ^{40}Ar, ^{28}Si and ^{32}S (see legend).

GeV and 10 TeV. As we also show in Fig. C.4 the most important elements are ^{28}Si and ^{56}Fe, this is confirmed by the corresponding plot for the capture rate for $m_\chi \lesssim 110\,\text{GeV}$, ^{56}Fe alone constrains the parameter space.

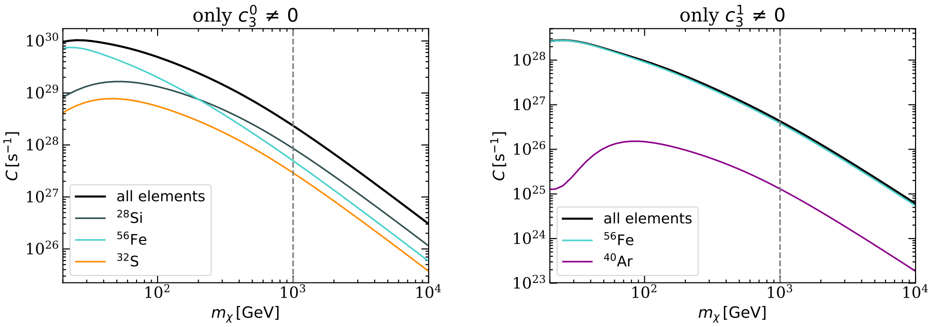

Figure C.5: Dark matter capture rate C versus mass m_χ for all elements (black) and the most important elements (see legend), assuming $c_3^\tau = 1$. *Left panel*: Only c_3^0 is non-zero, *right panel*: Only c_3^1 is non-zero. The dashed vertical line indicates the dark matter mass (1 TeV) assumed in the corresponding ellipse plot.

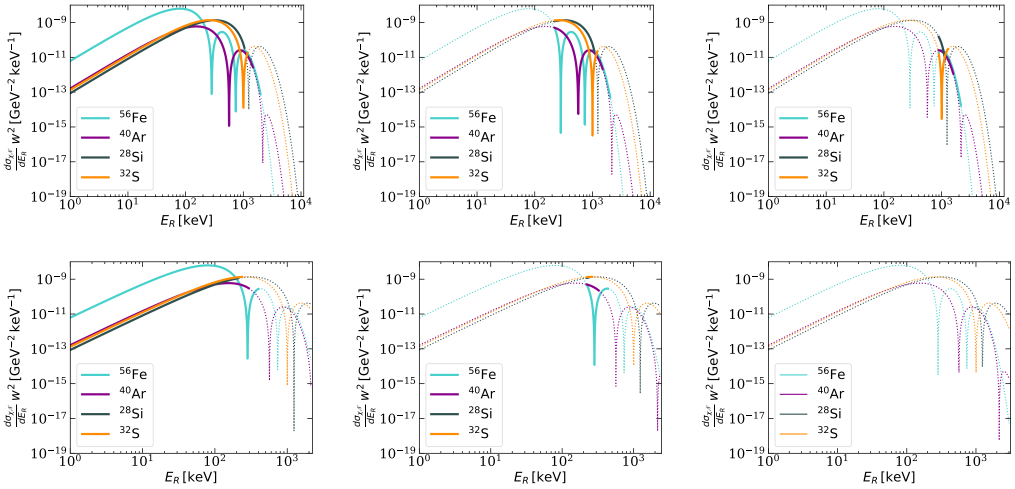

Figure C.6: Differential dark matter-nucleon cross-section $d\sigma_{\chi\mathscr{N}}/dE_R$ × squared dark matter velocity w^2 against recoil energy E_R for operator 3 and the most important elements (see legend). *Upper panels* (*lower panels*): Scattering point in the center (on the surface) of the Sun, *left panels* (*middle panels*) [*right panels*]: Asymptotic dark matter velocity $u = 0$ (200) [400] km/s. *Solid* (*dashed*): Possible (Impossible) range of recoil energies.

Operator $\hat{\mathcal{O}}_4$

Similar to operator $\hat{\mathcal{O}}_1$, operator $\hat{\mathcal{O}}_4$ describes a special case among the 14 effective operators: A linear combination of the corresponding responses Σ'' and

Σ' results is the widely known standard spin-dependent interaction. Also this operator does neither depend on the velocity nor on the momentum transfer. As already described in section A the two Σ-responses are sensitive to unpaired protons or neutrons. As we show in Fig. C.7, the four most important elements fulfilling this requirement are ^{1}H, ^{14}N, ^{3}He and ^{27}Al for $m_\chi = 1$ TeV. The different alignments can be understood quite easily: The ^{1}H-strip and the allowed parameter space for ^{27}Al are aligned with the c_4^n axis, since they have one unpaired proton and can therefore not at all or at most badly constrain c_4^n, whereas the allowed parameter space for ^{3}He is aligned with the c_4^p-axis, since it has one unpaired neutron and can therefore badly constrain c_4^p. The fourth element, ^{14}N, is quite special, since it has one unpaired proton and one unpaired neutron, and it is isoscalar. The latter property causes the alignment with the isovector axis. The most constraining element for the proton component is ^{1}H due to its alignment and higher abundance in the Sun compared to ^{27}Al. The strongest constraint for the neutron component comes from ^{14}N, which is slightly more abundant in the Sun than ^{3}He.

Although the capture rates for the dark matter mass range between 20 GeV and 10 TeV in Fig. C.8 show that the sizes of the ellipses would change for different masses compared to $m_\chi = 1$ TeV, the two most constraining elements however will remain ^{1}H and ^{14}N.

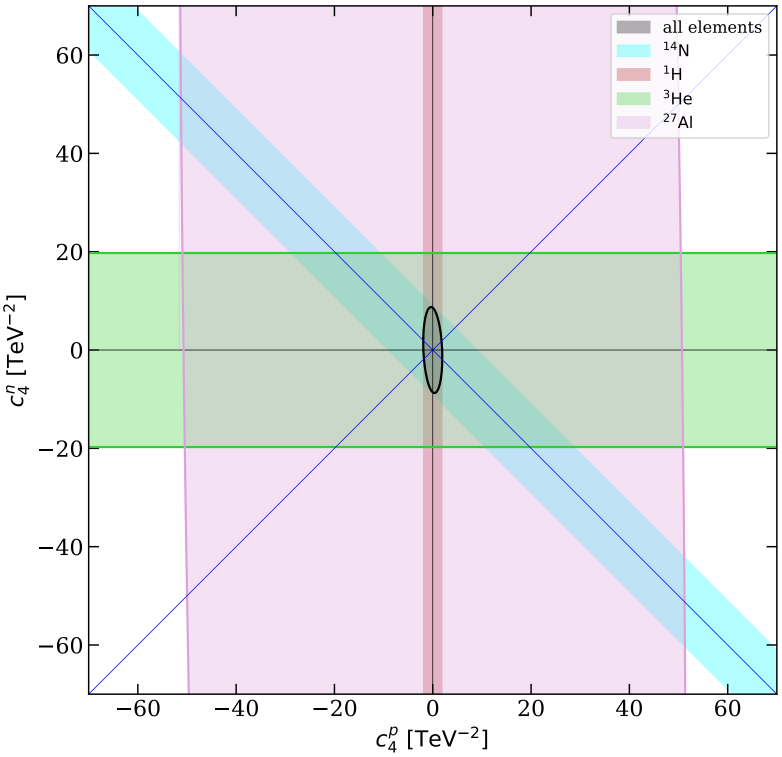

Figure C.7: Allowed parameter space spanned by c_4^p and c_4^n for all elements (black) and for the most important nuclei ^{1}H, ^{14}N, ^{3}He and ^{27}Al (see legend) for $m_\chi = 1$ TeV.

Operator $\hat{\mathcal{O}}_5$

Contributing responses to interactions involving operator $\hat{\mathcal{O}}_5$ are the $\varDelta$-response suppressed by q^4 and the M-response suppressed by q^2 and $\left(\mathbf{v}_T^\perp\right)^2$. The four most abundant elements in the Sun fulfilling the $\varDelta$-response requirement of having a non-s-shell unpaired proton or neutron are ^{14}N, which has even an unpaired proton and an unpaired neutron, ^{27}Al, ^{13}C and ^{23}Na, having an unpaired proton. In Fig. C.10 we confirm that ^{14}N and ^{27}Al are indeed the two elements constraining the black ellipse. ^{23}Na appears as important contribution as well. According to the forecast, also ^{13}C should be present in the figure. The reason why it is not is that the form factors for ^{13}C are not provided in [144] and therefore it was not possible for us to generate the allowed parameter

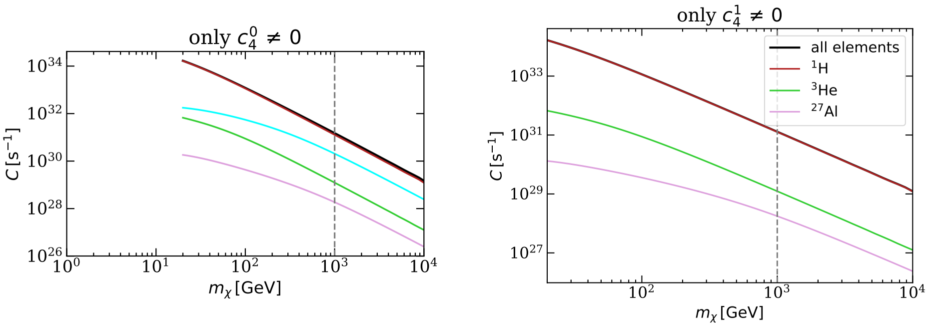

Figure C.8: Dark matter capture rate C versus mass m_χ for all elements (black) and the most important elements (see legend), assuming $c_4^\tau = 1$. *Left panel*: Only c_4^0 is non-zero, *right panel*: Only c_4^1 is non-zero. The dashed vertical line indicates the dark matter mass (1 TeV) assumed in the corresponding ellipse plot.

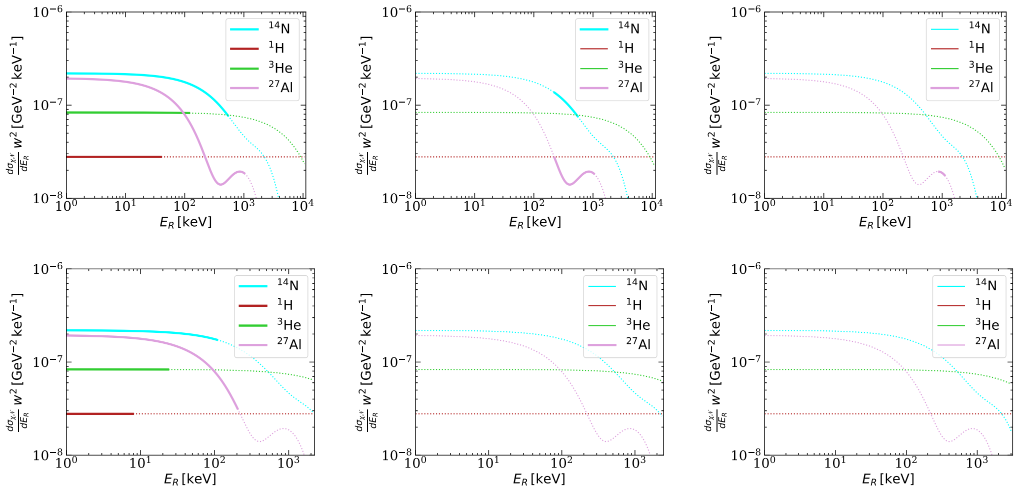

Figure C.9: Differential dark matter-nucleon cross-section $d\sigma_{\chi\mathcal{N}}/dE_R \times$ squared dark matter velocity w^2 against recoil energy E_R for operator 4 and the most important elements (see legend). *Upper panels* (*lower panels*): Scattering point in the center (on the surface) of the Sun, *left panels* (*middle panels*) [*right panels*]: Asymptotic dark matter velocity $u = 0$ (200) [400] km/s. *Solid* (*dashed*): Possible (Impossible) range of recoil energies.

space for ^{13}C.

Due to the velocity and momentum suppression, the M-response does not significantly contribute compared to the Δ-response, which can also be seen in Fig. C.10.

The plots for the capture rates for $m_\chi = 1$ TeV in Fig. C.11 fit the results of Fig. C.10. We also see that the order of the relevant nuclei remains unchanged considering different dark matter masses.

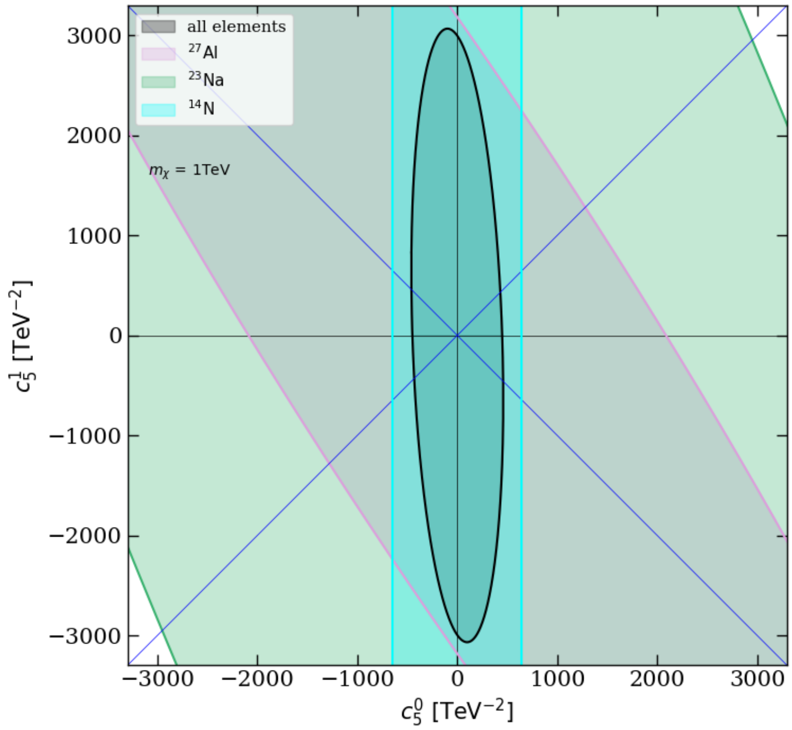

Figure C.10: Allowed parameter space spanned by c_5^0 and c_5^1 for all elements (black) and for the most important nuclei ^{27}Al, ^{23}Na and ^{14}N (see legend).

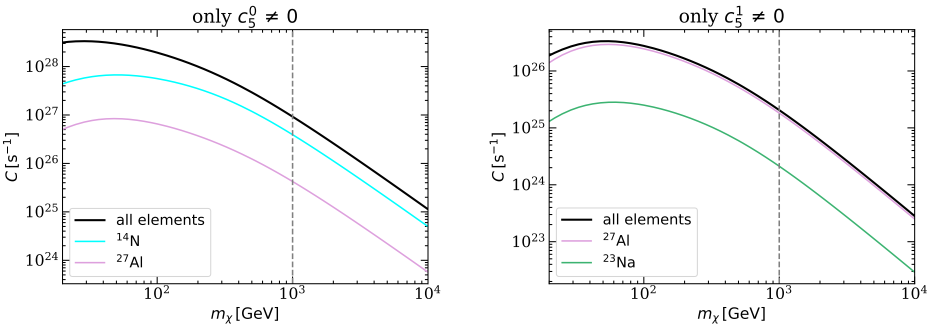

Figure C.11: Dark matter capture rate C versus mass m_χ for all elements (black) and the most important elements (see legend), assuming $c_5^\tau = 1$. *Left panel*: Only c_5^0 is non-zero, *right panel*: Only c_5^1 is non-zero. The dashed vertical line indicates the dark matter mass (1 TeV) assumed in the corresponding ellipse plot.

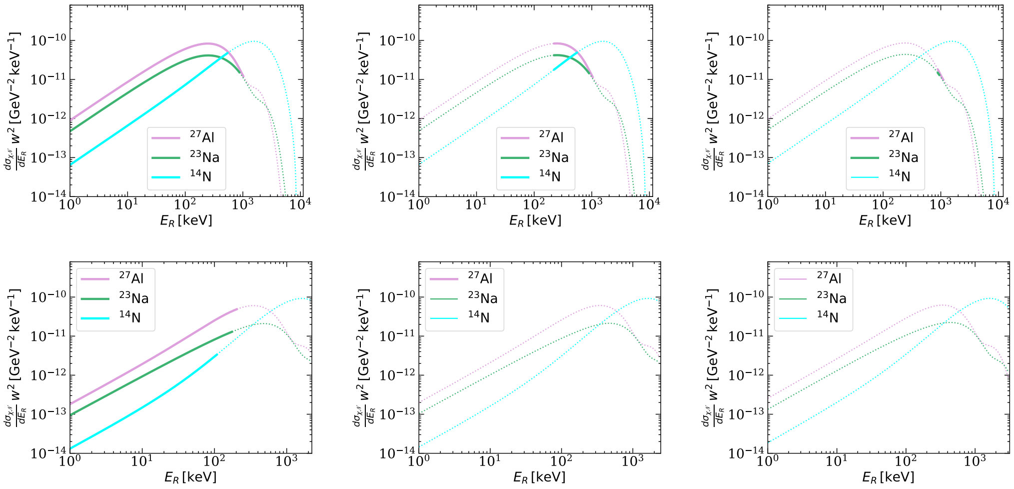

Figure C.12: Differential dark matter-nucleon cross-section $d\sigma_{\chi\mathcal{N}}/dE_R$ × squared dark matter velocity w^2 against recoil energy E_R for operator 5 and the most important elements (see legend). *Upper panels* (*lower panels*): Scattering point in the center (on the surface) of the Sun, *left panels* (*middle panels*) [*right panels*]: Asymptotic dark matter velocity $u = 0$ (200) [400] km/s. *Solid* (*dashed*): Possible (Impossible) range of recoil energies.

Operator $\hat{\mathcal{O}}_6$

The only relevant response for operator $\hat{\mathcal{O}}_6$ is Σ'' which is q^4-dependent and velocity independent. Therefore, dark matter would only couple to elements with unpaired protons and/or neutrons. For this operator and dark matter mass the most constraining elements are ^{14}N, ^{27}Al and ^{23}Na, where the two former constrain the black parameter space, which we show in Fig. C.13. Although ^{1}H fulfills the Σ''-requirements and is contained in the Sun with a high amount, it is not important for operator $\hat{\mathcal{O}}_6$ and $m_\chi = 1$ TeV. This can be understood by looking at Fig. C.14: The high amount of ^{1}H cannot compensate its small mass in this case.

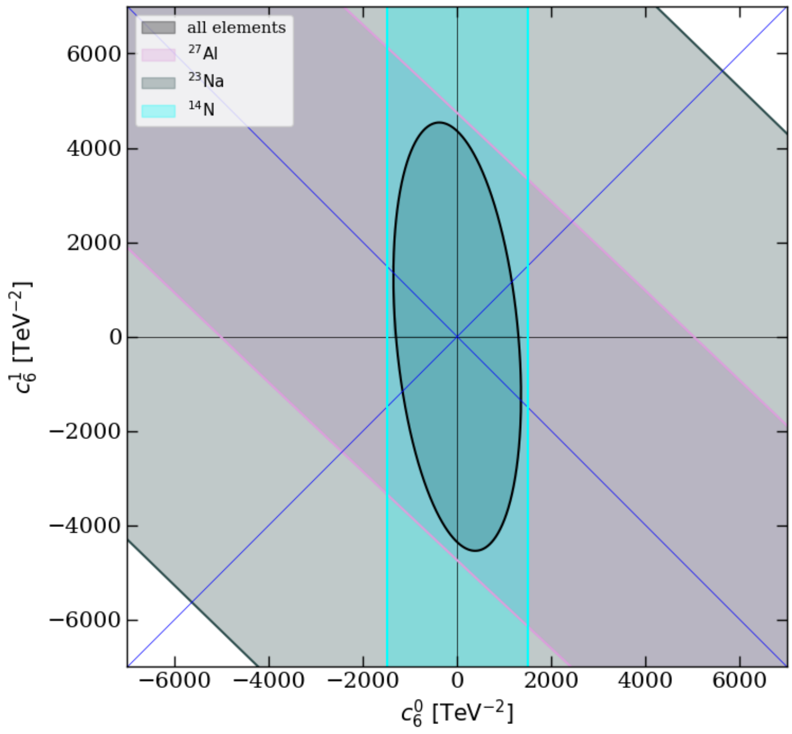

Figure C.13: Allowed parameter space spanned by c_6^0 and c_6^1 for all elements (black) and for the most important nuclei ^{27}Al, ^{23}Na and ^{14}N (see legend).

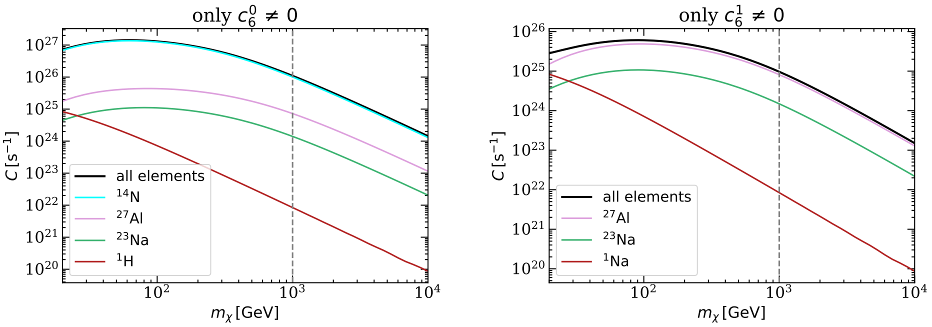

Figure C.14: Dark matter capture rate C versus mass m_χ for all elements (black) and the most important elements (see legend), assuming $c_6^\tau = 1$. *Left panel*: Only c_6^0 is non-zero, *right panel*: Only c_6^1 is non-zero. The dashed vertical line indicates the dark matter mass (1 TeV) assumed in the corresponding ellipse plot.

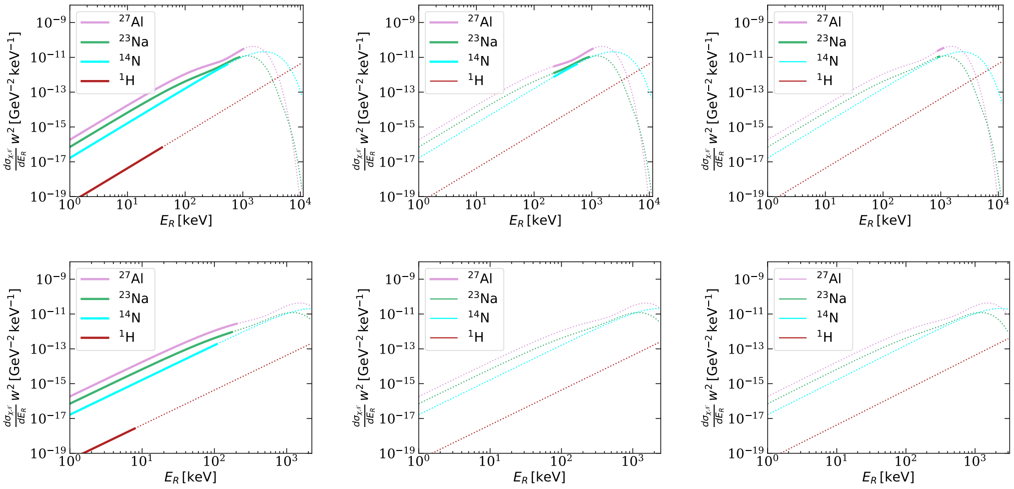

Figure C.15: Differential dark matter-nucleon cross-section $d\sigma_{\chi\mathcal{N}}/dE_R$ × squared dark matter velocity w^2 against recoil energy E_R for operator 6 and the most important elements (see legend). *Upper panels* (*lower panels*): Scattering point in the center (on the surface) of the Sun, *left panels* (*middle panels*) [*right panels*]: Asymptotic dark matter velocity $u = 0$ (200) [400] km/s. *Solid* (*dashed*): Possible (Impossible) range of recoil energies.

Operator $\hat{\mathcal{O}}_7$

The only response contributing to interactions with operator $\hat{\mathcal{O}}_7$ is Σ' with $\left(\mathbf{v}_T^\perp\right)^2$-suppression. Similar to operator $\hat{\mathcal{O}}_4$, it is momentum independent and sensitive to the nuclear spin, *i.e.* elements with unpaired protons or neutrons. Therefore, the most important elements for operator $\hat{\mathcal{O}}_7$ are also ^{1}H, ^{14}N and ^{3}He, which we show in Fig. C.16. Like for operator $\hat{\mathcal{O}}_4$ the black parameter space is constrained by ^{1}H and ^{14}N.

In Fig. C.17 we show that the order of importance of the considered contributing elements does not change for different masses.

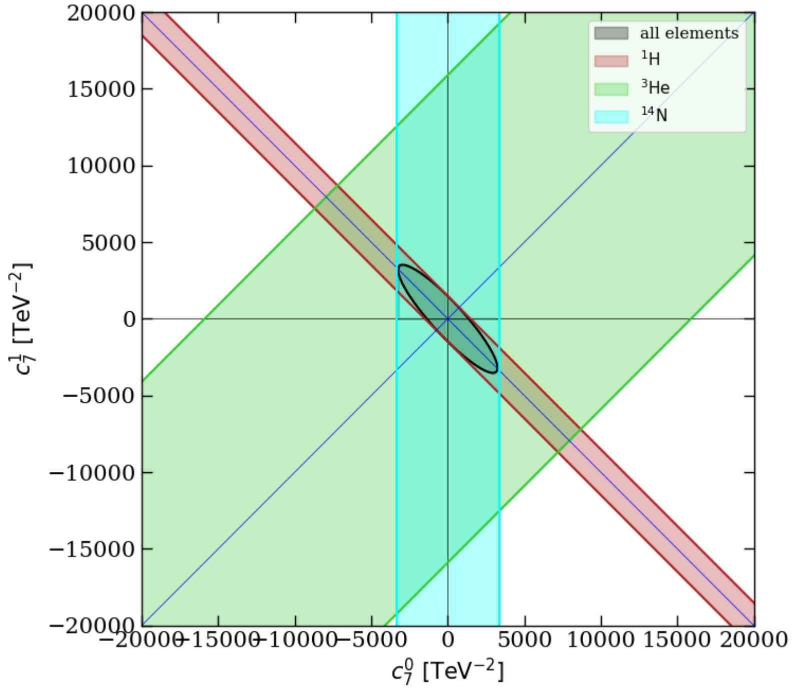

Figure C.16: Allowed parameter space spanned by c_7^0 and c_7^1 for all elements (black) and for the most important nuclei ^{1}H, ^{3}He and ^{14}N (see legend).

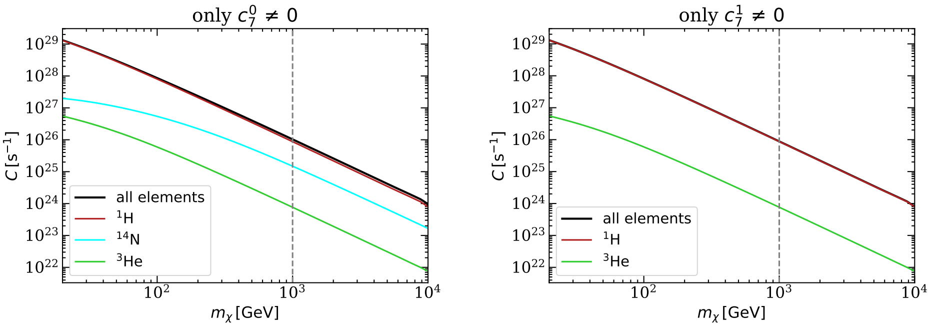

Figure C.17: Dark matter capture rate C versus mass m_χ for all elements (black) and the most important elements (see legend), assuming $c_7^\tau = 1$. *Left panel*: Only c_7^0 is non-zero, *right panel*: Only c_7^1 is non-zero. The dashed vertical line indicates the dark matter mass (1 TeV) assumed in the corresponding ellipse plot.

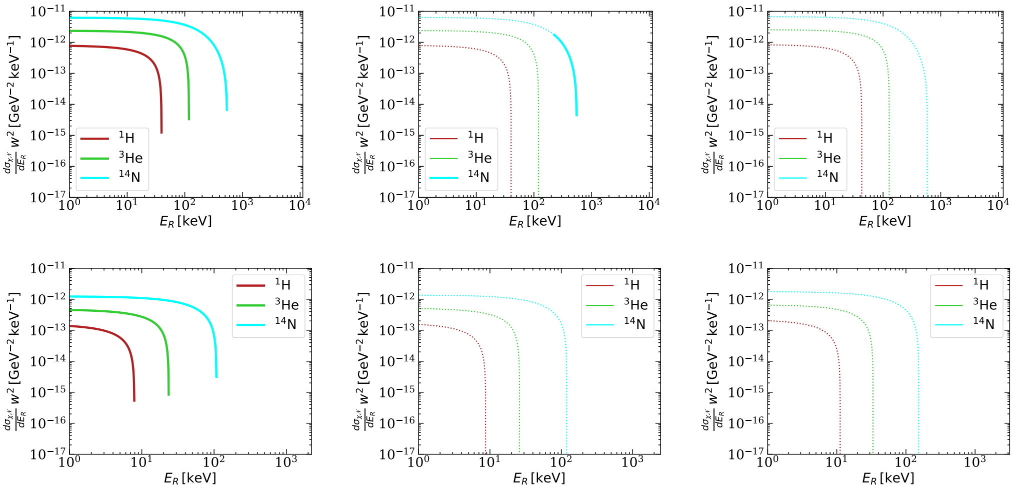

Figure C.18: Differential dark matter-nucleon cross-section $d\sigma_{\chi\mathcal{N}}/dE_R \times$ squared dark matter velocity w^2 against recoil energy E_R for operator 7 and the most important elements (see legend). *Upper panels* (*lower panels*): Scattering point in the center (on the surface) of the Sun, *left panels* (*middle panels*) [*right panels*]: Asymptotic dark matter velocity $u = 0$ (200) [400] km/s. *Solid* (*dashed*): Possible (Impossible) range of recoil energies.

Operator $\hat{\mathcal{O}}_8$

Similar to operator $\hat{\mathcal{O}}_5$, $\hat{\mathcal{O}}_8$ is sensitive to the Δ- and M-response, though having a q^2- (Δ) and $\left(\mathbf{v}_T^\perp\right)^2$- ($M$) suppression instead. The most abundant elements fulfilling the Δ-response requirement of having an unpaired proton or neutron in a non-s-shell are ^{14}N, ^{27}Al and ^{23}Na. This is confirmed by Fig. C.19. The black parameter space is constrained by ^{14}N and ^{27}Al.

Since the M-response is not momentum suppressed, it also leaves its imprints on the ellipse plot. Having the right balance between being a heavy element and making up a large fraction of the particles contained in the Sun, also ^{16}O appears in Fig. C.19.

In Fig. C.20 we show in the left panel that for smaller dark matter masses than ≈ 110 GeV, ^{16}O is more dominant than ^{14}N, whereas the order of the most dominating elements in the right panel remains unchanged.

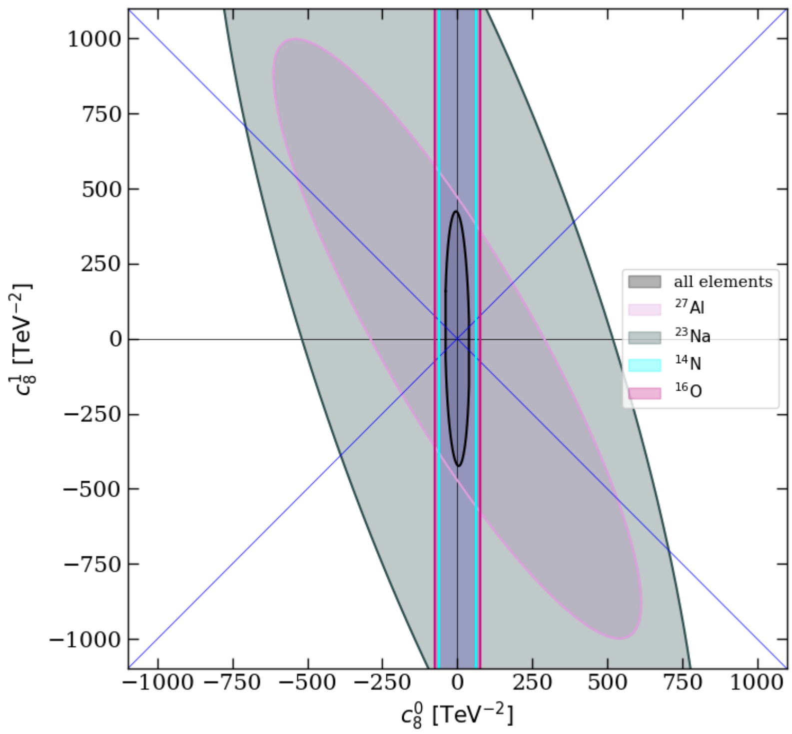

Figure C.19: Allowed parameter space spanned by c_8^0 and c_8^1 for all elements (black) and for the most important nuclei ^{14}N, ^{16}O, ^{27}Al and ^{23}Na (see legend).

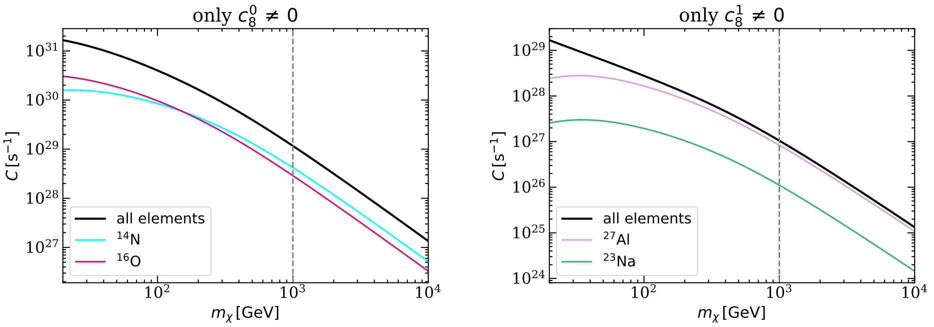

Figure C.20: Dark matter capture rate C versus mass m_χ for all elements (black) and the most important elements (see legend), assuming $c_8^\tau = 1$. *Left panel*: Only c_8^0 is non-zero, *right panel*: Only c_8^1 is non-zero. The dashed vertical line indicates the dark matter mass (1 TeV) assumed in the corresponding ellipse plot.

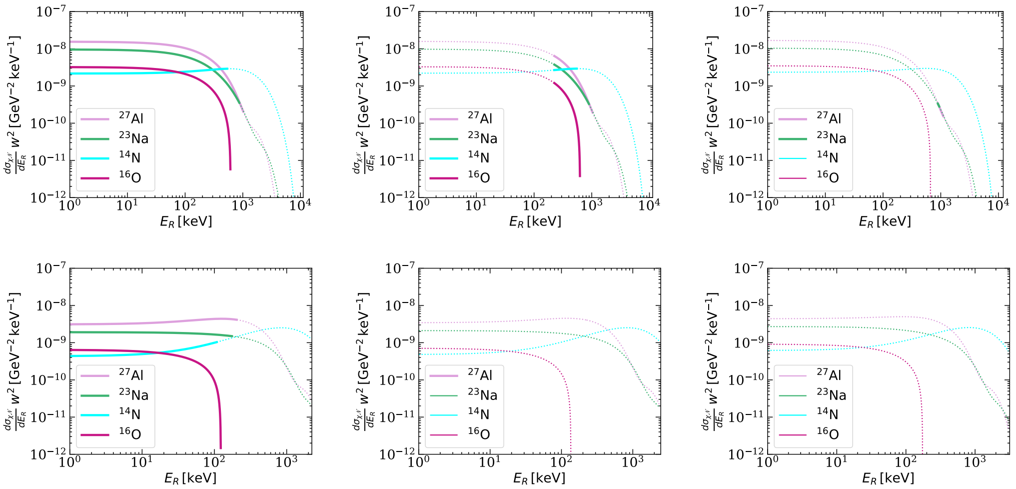

Figure C.21: Differential dark matter-nucleon cross-section $d\sigma_{\chi\mathcal{N}}/dE_R$ × squared dark matter velocity w^2 against recoil energy E_R for operator 8 and the most important elements (see legend). *Upper panels* (*lower panels*): Scattering point in the center (on the surface) of the Sun, *left panels* (*middle panels*) [*right panels*]: Asymptotic dark matter velocity $u = 0$ (200) [400] km/s. *Solid* (*dashed*): Possible (Impossible) range of recoil energies.

Operator $\hat{\mathcal{O}}_9$

The Σ'-response is the only response contributing to interactions that involve operator $\hat{\mathcal{O}}_9$. It is q^2-suppressed. On the one hand, elements with unpaired protons or neutrons are favored. On the other hand, the fraction of the elements needs to be balanced by their mass, due to the moderate momentum dependence. The most constraining elements are therefore ^{1}H, ^{27}Al and ^{14}N, where ^{1}H and ^{14}N constrain the black parameter space. For other possible candidates that fulfill the requirement of having an unpaired proton or neutron, such as ^{3}He or ^{23}Na are either too light or rarely present in the Sun (or both) to contribute significantly in interactions with $\hat{\mathcal{O}}_9$ as we show in Fig. C.22.

We show in Fig. C.23 that for very small dark matter masses (below 30 GeV) ^{1}H becomes slightly more dominant than ^{14}N, which can be explained by its smaller mass.

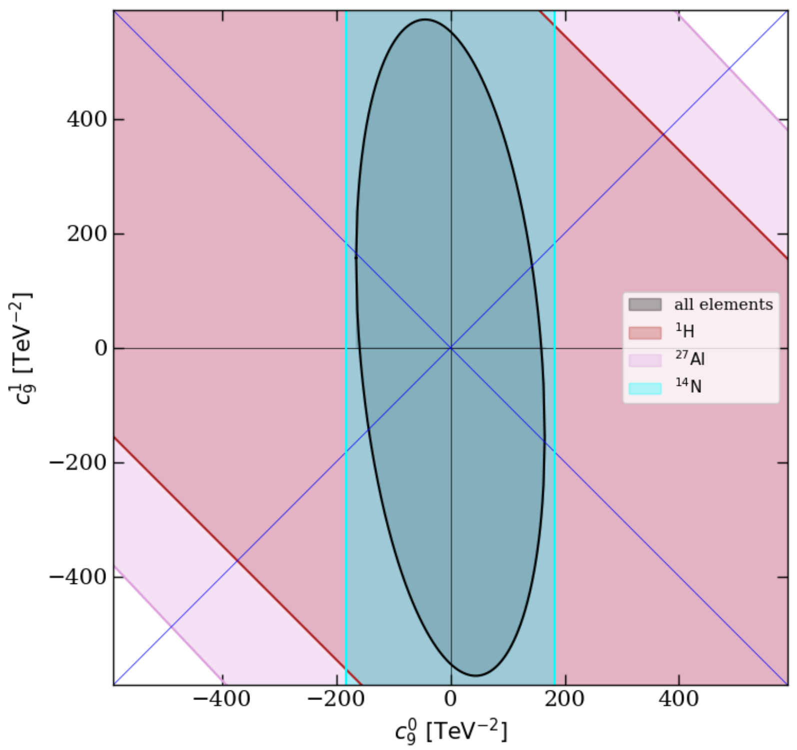

Figure C.22: Allowed parameer space spanned by c_9^0 and c_9^1 for all elements (black) and for the most important nuclei ^{1}H, ^{27}Al and ^{14}N (see legend).

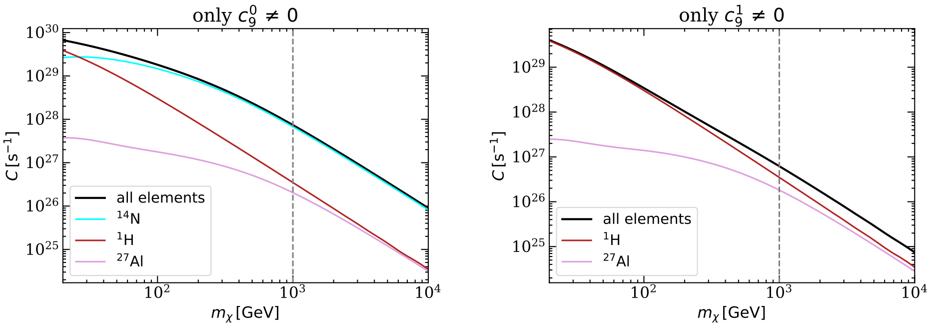

Figure C.23: Dark matter capture rate C versus mass m_χ for all elements (black) and the most important elements (see legend), assuming $c_9^\tau = 1$. *Left panel*: Only c_9^0 is non-zero, *right panel*: Only c_9^1 is non-zero. The dashed vertical line indicates the dark matter mass (1 TeV) assumed in the corresponding ellipse plot.

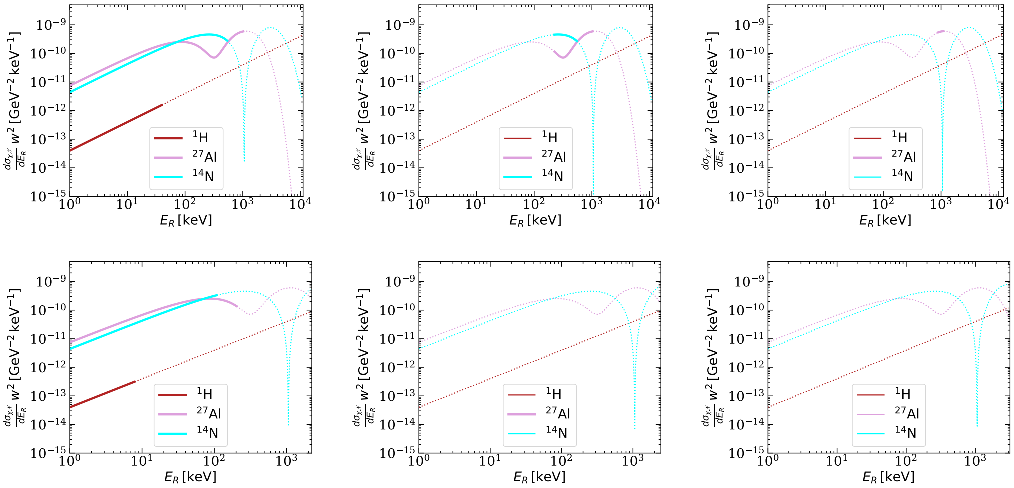

Figure C.24: Differential dark matter-nucleon cross-section $d\sigma_{\chi\mathcal{N}}/dE_R \times$ squared dark matter velocity w^2 against recoil energy E_R for operator 9 and the most important elements (see legend). *Upper panels* (*lower panels*): Scattering point in the center (on the surface) of the Sun, *left panels* (*middle panels*) [*right panels*]: Asymptotic dark matter velocity $u = 0$ (200) [400] km/s. *Solid* (*dashed*): Possible (Impossible) range of recoil energies.

Operator $\hat{\mathcal{O}}_{10}$

Since the only contributing response in interactions with $\hat{\mathcal{O}}_{10}$ is the Σ''-response, which favors elements with an unpaired proton or neutron, and since the momentum is suppressed by q^2, the resulting Fig. C.25 is very similar to Fig. C.22 for operator $\hat{\mathcal{O}}_9$. Requiring an element with unpaired proton or neutron and the optimum balance between target mass and abundance, the outcome is again that ^{1}H, ^{27}Al and ^{14}N are the most dominant elements for that dark matter mass of 1 TeV.

We show in Fig. C.26 that while ^{14}N remains the dominant element in the whole dark matter mass range for the isoscalar component, ^{27}Al becomes less important than ^{1}H for the isovector component for $m_\chi \lesssim 600$ GeV, making ^{1}H the most constraining element for the lower mass range.

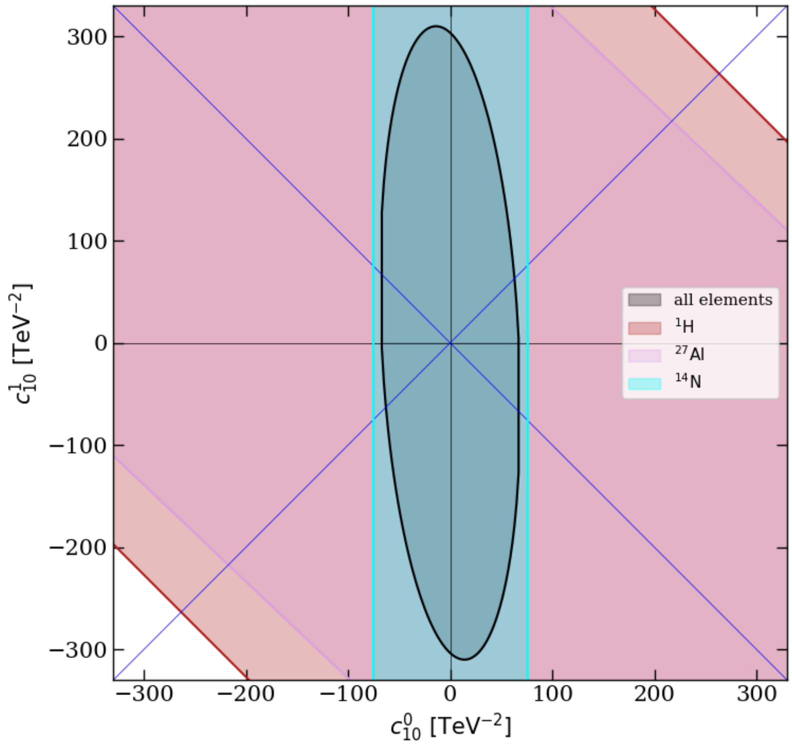

Figure C.25: Allowed parameter space spanned by c^0_{10} and c^1_{10} for all elements (black) and for the most important nuclei ^{1}H, ^{27}Al and ^{14}N (see legend).

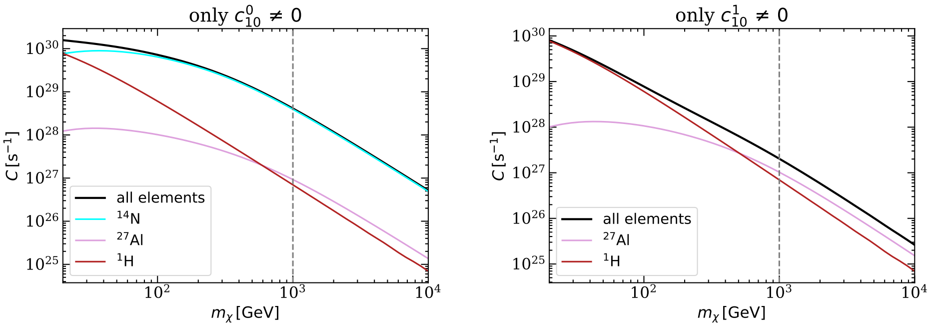

Figure C.26: Dark matter capture rate C versus mass m_χ for all elements (black) and the most important elements (see legend), assuming $c^\tau_{10} = 1$. *Left panel*: Only c^0_{10} is non-zero, *right panel*: Only c^1_{10} is non-zero. The dashed vertical line indicates the dark matter mass (1 TeV) assumed in the corresponding ellipse plot.

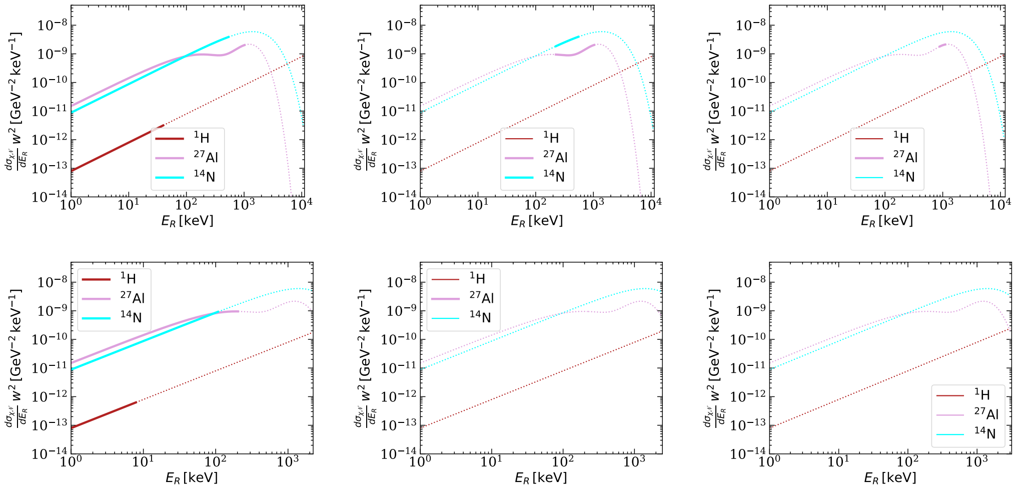

Figure C.27: Differential dark matter-nucleon cross-section $d\sigma_{\chi\mathcal{N}}/dE_R \times$ squared dark matter velocity w^2 against recoil energy E_R for operator 10 and the most important elements (see legend). *Upper panels* (*lower panels*): Scattering point in the center (on the surface) of the Sun, *left panels* (*middle panels*) [*right panels*]: Asymptotic dark matter velocity $u = 0$ (200) [400] km/s. *Solid* (*dashed*): Possible (Impossible) range of recoil energies.

Operator $\hat{\mathcal{O}}_{11}$

Interactions involving operator $\hat{\mathcal{O}}_{11}$ are sensitive to the M-response with q^2-suppression. Similar as for operator $\hat{\mathcal{O}}_1$, the optimum balance between target mass and abundance is required to give an important contribution to the dark matter-nucleus interaction. Since however the interaction involving operator $\hat{\mathcal{O}}_{11}$ are moderately momentum suppressed, the optimum balance is shifted more towards higher masses compared to the one for operator $\hat{\mathcal{O}}_1$. As we show in Fig. C.28 ^{1}H, which is one of the most constraining elements for operator $\hat{\mathcal{O}}_1$, is not visible; although its abundance in the Sun is huge, the mass is too small to contribute significantly to constrain the black parameter space. The most important elements are instead ^{56}Fe, ^{40}Ar, ^{16}O and ^{20}Ne, where ^{16}O and ^{56}Fe constrain the black parameter space.

While we show in Fig. C.29 that the order of the important elements is the same for the isovector component, ^{56}Fe is getting more important than ^{20}Ne for $m_\chi \lesssim 40$ GeV for the isoscalar component.

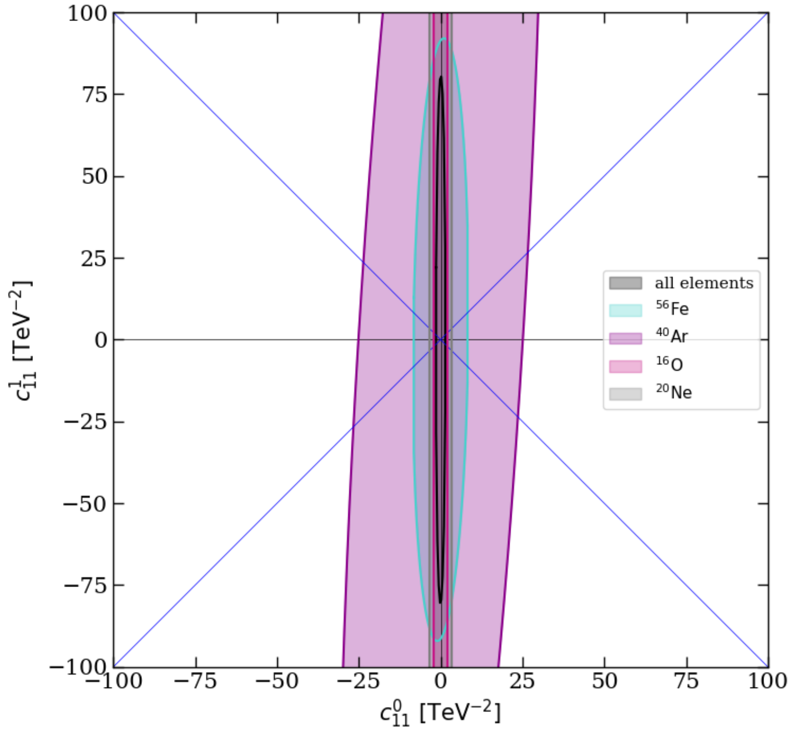

Figure C.28: Allowed parameter space spanned by c^0_{11} and c^1_{11} for all elements (black) and for the most important nuclei ^{56}Fe, ^{40}Ar, ^{16}O and ^{20}Ne (see legend).

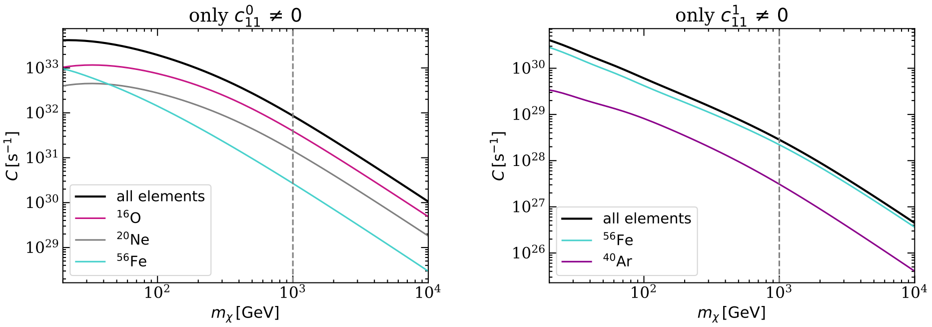

Figure C.29: Dark matter capture rate C versus mass m_χ for all elements (black) and the most important elements (see legend), assuming $c_{11}^\tau = 1$. *Left panel*: Only c_{11}^0 is non-zero, *right panel*: Only c_{11}^1 is non-zero. The dashed vertical line indicates the dark matter mass (1 TeV) assumed in the corresponding ellipse plot.

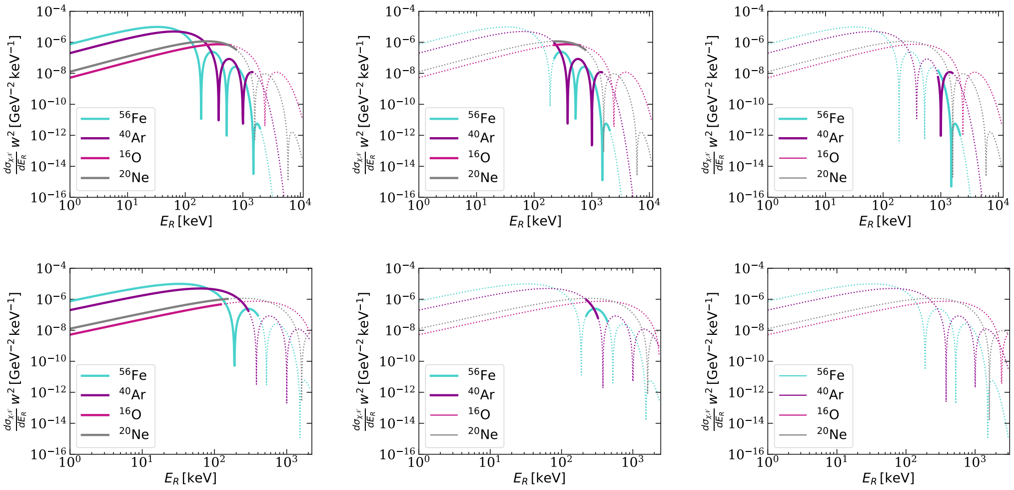

Figure C.30: Differential dark matter-nucleon cross-section $d\sigma_{\chi\mathcal{N}}/dE_R \times$ squared dark matter velocity w^2 against recoil energy E_R for operator 11 and the most important elements (see legend). *Upper panels* (*lower panels*): Scattering point in the center (on the surface) of the Sun, *left panels* (*middle panels*) [*right panels*]: Asymptotic dark matter velocity $u = 0$ (200) [400] km/s. *Solid* (*dashed*): Possible (Impossible) range of recoil energies.

Operator $\hat{\mathcal{O}}_{12}$

The relevant responses for operator $\hat{\mathcal{O}}_{12}$ are Φ'' and $\tilde{\Phi}'$, both with q^2-suppression, and Σ'' and Σ', both with $\left(\mathbf{v}_T^\perp\right)^2$-suppression. The most important elements are ^{56}Fe, ^{27}Al, ^{28}Si and ^{32}S. In Fig. C.31, we show that ^{28}Si and ^{56}Fe constrain the black parameter space. From Fig. C.32 we learn that ^{56}Fe and ^{28}Si are the most constraining elements in the whole mass range.

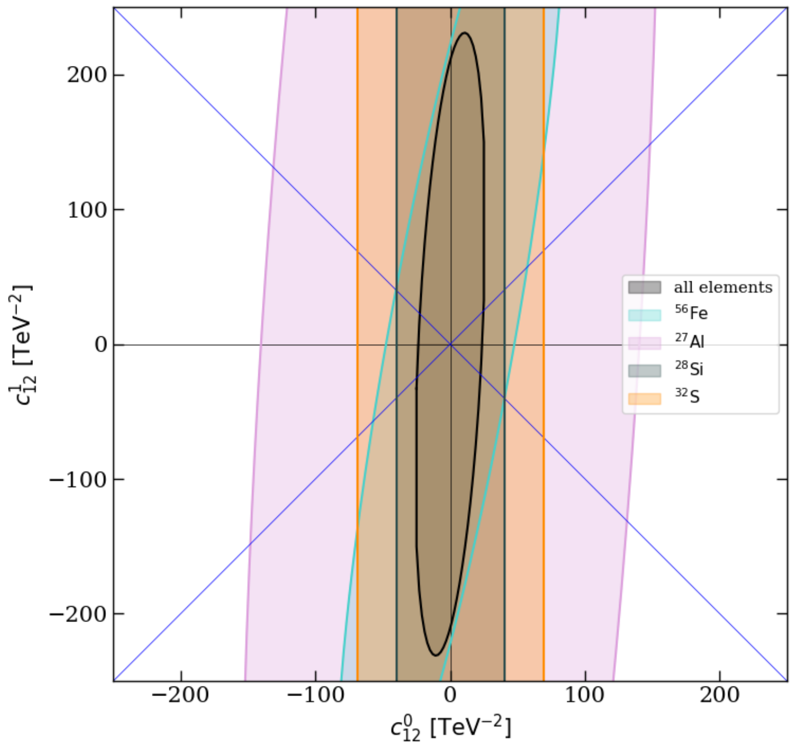

Figure C.31: Allowed parameter space spanned by c^0_{12} and c^1_{12} for all elements (black) and for the most important nuclei ^{56}Fe, ^{27}Al, ^{28}Si and ^{32}S (see legend).

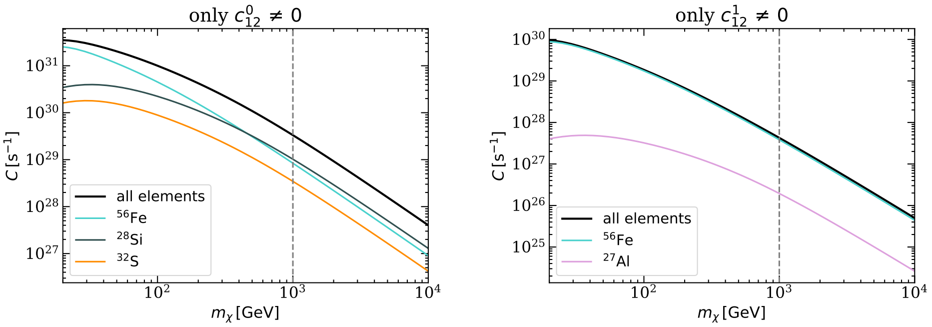

Figure C.32: Dark matter capture rate C versus mass m_χ for all elements (black) and the most important elements (see legend), assuming $c^\tau_{12} = 1$. *Left panel*: Only c^0_{12} is non-zero, *right panel*: Only c^1_{12} is non-zero. The dashed vertical line indicates the dark matter mass (1 TeV) assumed in the corresponding ellipse plot.

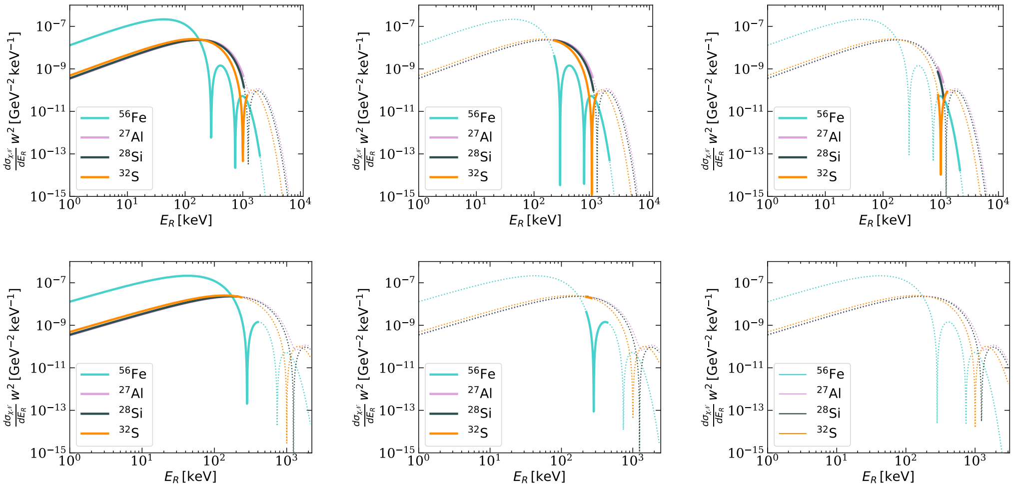

Figure C.33: Differential dark matter-nucleon cross-section $d\sigma_{\chi\mathcal{N}}/dE_R$ × squared dark matter velocity w^2 against recoil energy E_R for operator 12 and the most important elements (see legend). *Upper panels* (*lower panels*): Scattering point in the center (on the surface) of the Sun, *left panels* (*middle panels*) [*right panels*]: Asymptotic dark matter velocity $u = 0$ (200) [400] km/s. *Solid* (*dashed*): Possible (Impossible) range of recoil energies.

Operator $\hat{\mathcal{O}}_{13}$

The contributing responses in interactions with operator $\hat{\mathcal{O}}_{13}$ are $\tilde{\Phi}'$ with q^4-suppression and Σ'' with q^2- and $\left(\mathbf{v}_T^\perp\right)^2$-suppression. The only elements that can constrain interactions induced by the $\tilde{\Phi}'$ response are ^{27}Al, ^{23}Na and ^{14}N. Due to their abundance, ^{27}Al and ^{14}N constrain the black parameter space. Due to the isoscalarness of ^{14}N it cannot constrain the isovector contribution for which the most important element is ^{27}Al, whereas for the isoscalar contribution it is ^{14}N, as we see in Fig. C.35.

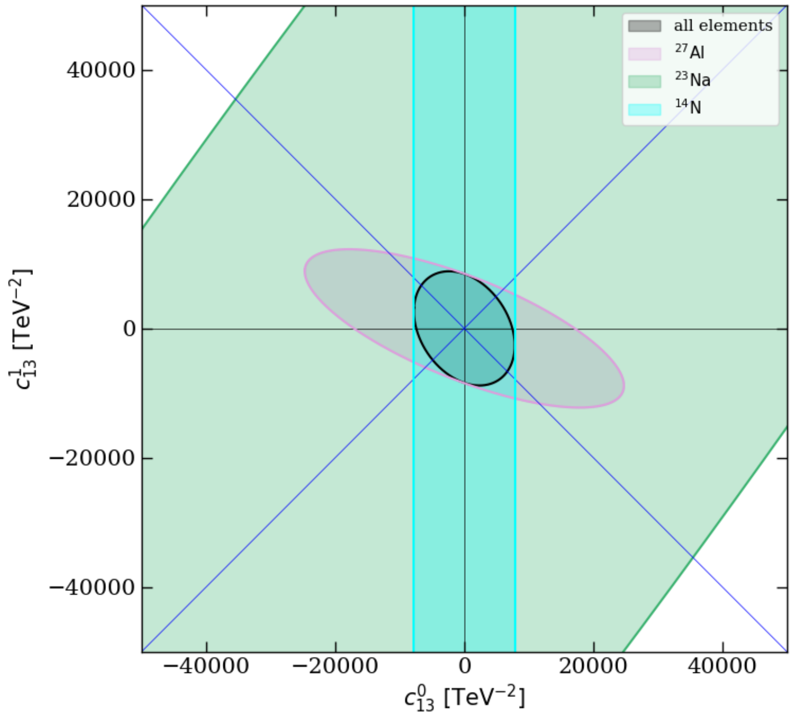

Figure C.34: Allowed parameter space spanned by c^0_{13} and c^1_{13} for all elements (black) and for the most important nuclei ^{27}Al, ^{23}Na and ^{14}N (see legend).

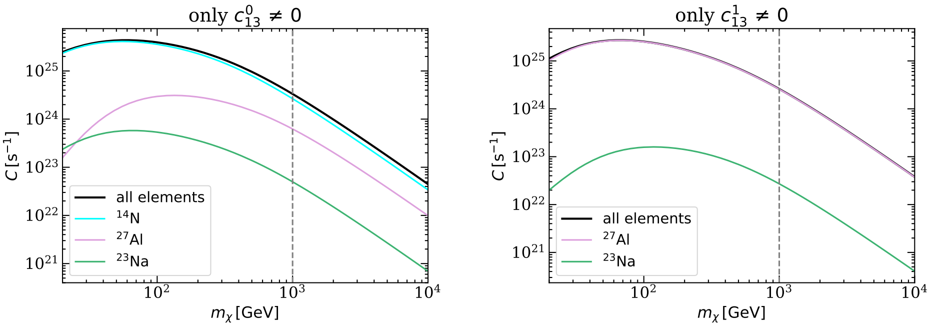

Figure C.35: Dark matter capture rate C versus mass m_χ for all elements (black) and the most important elements (see legend), assuming $c^\tau_{13} = 1$. *Left panel*: Only c^0_{13} is non-zero, *right panel*: Only c^1_{13} is non-zero. The dashed vertical line indicates the dark matter mass (1 TeV) assumed in the corresponding ellipse plot.

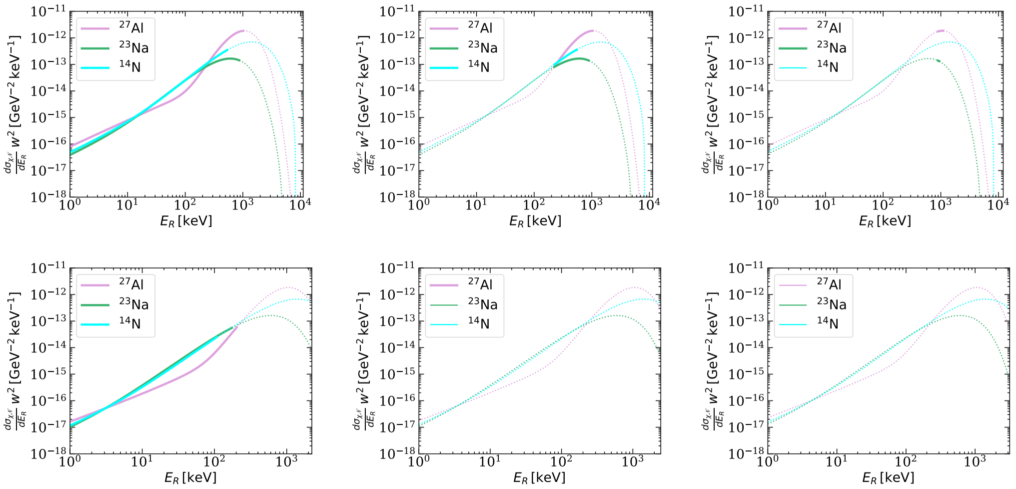

Figure C.36: Differential dark matter-nucleon cross-section $d\sigma_{\chi\mathcal{N}}/dE_R$ × squared dark matter velocity w^2 against recoil energy E_R for operator 13 and the most important elements (see legend). *Upper panels* (*lower panels*): Scattering point in the center (on the surface) of the Sun, *left panels* (*middle panels*) [*right panels*]: Asymptotic dark matter velocity $u = 0$ (200) [400] km/s. *Solid* (*dashed*): Possible (Impossible) range of recoil energies.

Operator $\hat{\mathcal{O}}_{14}$

The Σ'-response with q^2- and $\left(\mathbf{v}_T^\perp\right)^2$-suppression is the only relevant response for interactions involving $\hat{\mathcal{O}}_{14}$, *i.e.* elements with unpaired protons or neutrons are favored. The most important elements for this operator are ^{1}H, ^{14}N, ^{27}Al and ^{3}He where the ^{1}H and ^{14}N are the dominant elements that constrain the black parameter space, which we show in Fig. C.37.

In Fig. C.38 we show the importance of the considered elements for the whole mass range. We see that for the isoscalar and isovector component for lighter dark matter ($m_\chi \lesssim 80$ GeV) the importance of ^{27}Al and ^{3}He is swapped, which is caused by the smaller dark matter mass.

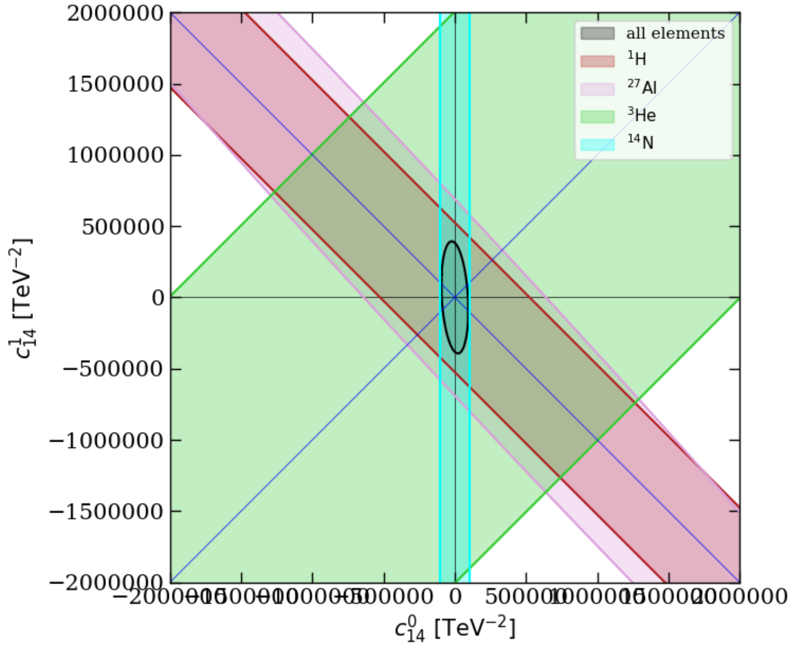

Figure C.37: Allowed parameter space spanned by c^0_{14} and c^1_{14} for all elements (black) and for the most important nuclei ^{1}H, ^{27}Al and ^{14}N (see legend).

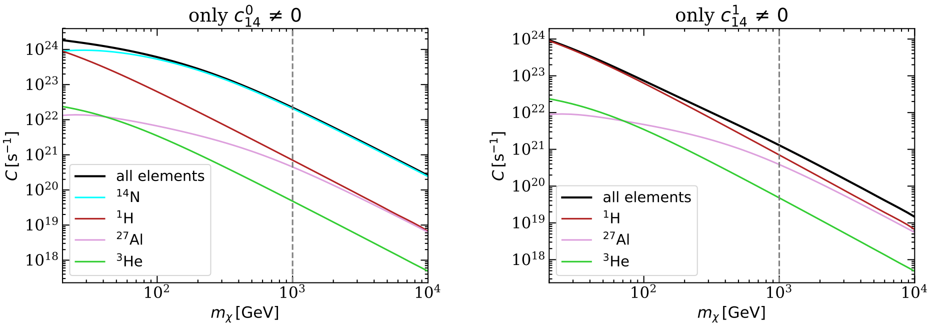

Figure C.38: Dark matter capture rate C versus mass m_χ for all elements (black) and the most important elements (see legend), assuming $c_{14}^\tau = 1$. *Left panel*: Only c_{14}^0 is non-zero, *right panel*: Only c_{14}^1 is non-zero. The dashed vertical line indicates the dark matter mass (1 TeV) assumed in the corresponding ellipse plot.

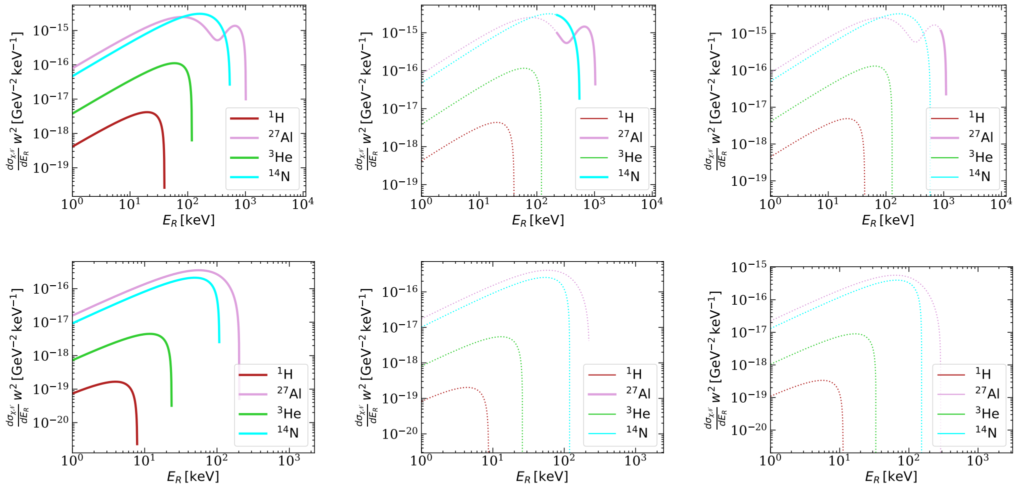

Figure C.39: Differential dark matter-nucleon cross-section $d\sigma_{\chi\mathcal{N}}/dE_R \times$ squared dark matter velocity w^2 against recoil energy E_R for operator 14 and the most important elements (see legend). *Upper panels* (*lower panels*): Scattering point in the center (on the surface) of the Sun, *left panels* (*middle panels*) [*right panels*]: Asymptotic dark matter velocity $u = 0$ (200) [400] km/s. *Solid* (*dashed*): Possible (Impossible) range of recoil energies.

Operator $\hat{\mathcal{O}}_{15}$

Interactions involving operator $\hat{\mathcal{O}}_{15}$ are induced by the responses Φ'' with q^6-suppression and Σ' with q^4- and $\left(\mathbf{v}_T^\perp\right)^2$-suppression. Favoring heavy elements with orbits of large angular momentum which are not fully occupied, the most important elements here are ^{56}Fe, ^{58}Ni, ^{28}Si and ^{32}S, where ^{56}Fe and ^{28}Si constrain the black parameter space.

Regarding the capture rate in Fig. C.41, ^{56}Fe and ^{28}Si are the most constraining elements in the whole mass range.

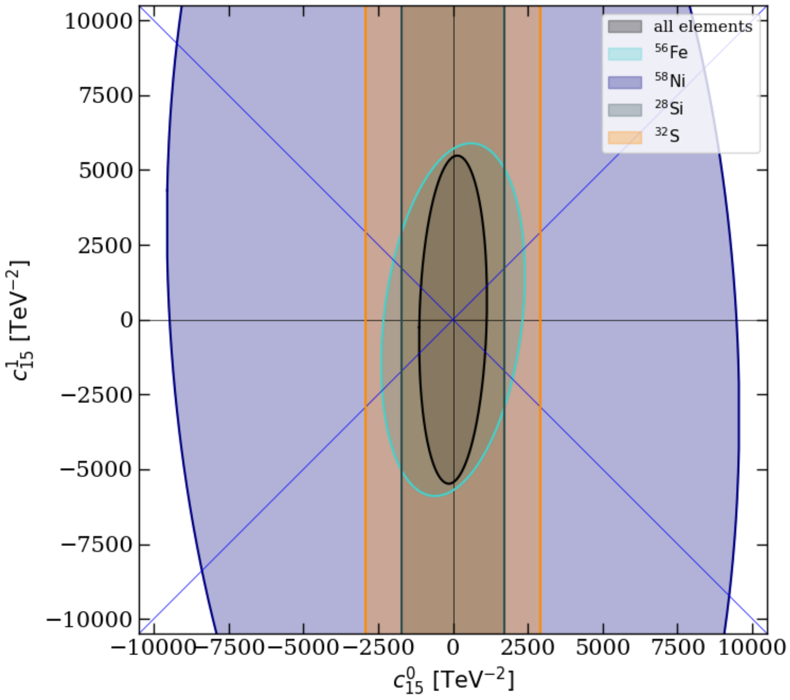

Figure C.40: Allowed parameter space spanned by c^0_{15} and c^1_{15} for all elements (black) and for the most important nuclei ^{56}Fe, ^{58}Ni, ^{28}Si and ^{32}S (see legend).

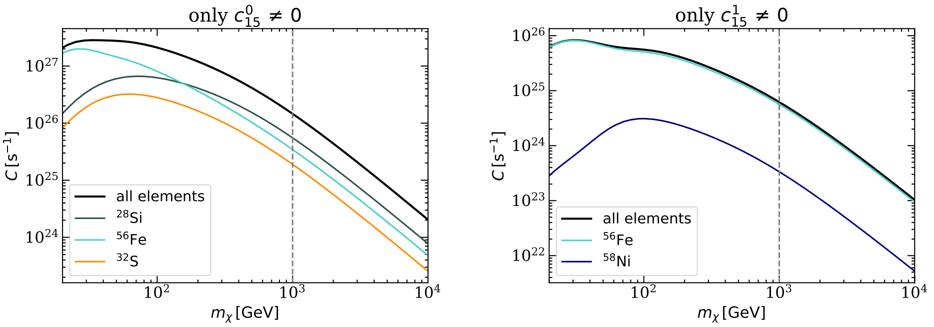

Figure C.41: Dark matter capture rate C versus mass m_χ for all elements (black) and the most important elements (see legend), assuming $c^\tau_{15} = 1$. *Left panel*: Only c^0_{15} is non-zero, *right panel*: Only c^1_{15} is non-zero. The dashed vertical line indicates the dark matter mass (1 TeV) assumed in the corresponding ellipse plot.

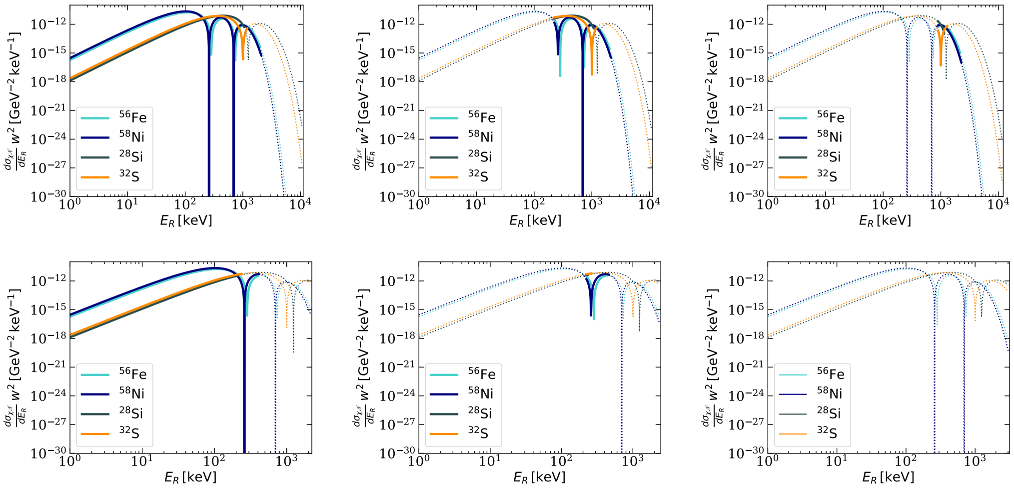

Figure C.42: Differential dark matter-nucleon cross-section $d\sigma_{\chi\mathcal{N}}/dE_R \times$ squared dark matter velocity w^2 against recoil energy E_R for operator 15 and the most important elements (see legend). *Upper panels* (*lower panels*): Scattering point in the center (on the surface) of the Sun, *left panels* (*middle panels*) [*right panels*]: Asymptotic dark matter velocity $u = 0$ (200) [400] km/s. *Solid* (*dashed*): Possible (Impossible) range of recoil energies.

D

Propagation of numerical errors

During the calculation of the $\mathbb{N}$-matrix errors might occur, *e.g.* from the numerical algorithms of integration, from the limited precision in the calculation of the nuclear response functions, from the modelling of the nuclear effects, from the dark matter velocity distribution et cetera. Therefore it is crucial to keep track of the propagation of numerical errors to make sure that the $\mathbb{N}$-matrix does not significantly suffer from those.

Let us assume that the true $\mathbb{N}$-matrix, $\mathbb{N}_{\text{true}}$, equals the $\mathbb{N}$-matrix that we obtain from numerical calculations, $\mathbb{N}_{\text{num}}$, plus a small value that defines the difference between $\mathbb{N}_{\text{true}}$ and $\mathbb{N}_{\text{num}}$, $\delta\mathbb{N}$. The elements of the perturbation are of the form $(\delta\mathbb{N})_{ij} = \epsilon a_{ij} \left(\mathbb{N}_{\text{true}}\right)_{ij}$, where $\epsilon \ll 1$ and the $\mathcal{O}(0.1)$-parameters a_{ij} keep in view the possible dependence of the relative errors on the matrix element. The relation of the elements of the true matrix and the numerical matrix is then given by

$$\left(\mathbb{N}_{\text{true}}\right)_{ij} = \frac{\left(\mathbb{N}_{\text{num}}\right)_{ij}}{1 + \epsilon a_{ij}} \simeq \left(\mathbb{N}_{\text{num}}\right)_{ij} \left(1 - \epsilon a_{ij}\right). \tag{D.1}$$

Using Eq. (4.10), we see that that numerical upper limit, $\left(c_\alpha^{\max}\right)_{\text{num}}$, and the true upper limit, $\left(c_\alpha^{\max}\right)_{\text{true}}$, on the coupling strength are related as

$$\left(c_\alpha^{\max}\right)_{\text{num}} = \left(c_\alpha^{\max}\right)_{\text{true}} \sqrt{\frac{\left(\mathbb{N}^{-1}_{\text{num}}\right)_{\alpha\alpha}}{\left(\mathbb{N}^{-1}_{\text{true}}\right)_{\alpha\alpha}}}. \tag{D.2}$$

At first order perturbation

$$\mathbb{N}^{-1}_{\text{num}} \simeq \mathbb{N}^{-1}_{\text{true}} - \mathbb{N}^{-1}_{\text{true}} \delta\mathbb{N} \mathbb{N}^{-1}_{\text{true}}, \tag{D.3}$$

and Eq. (D.2) then writes

$$(c_\alpha^{\max})_{\text{num}} \simeq (c_\alpha^{\max})_{\text{true}} \left[1 - \frac{1}{2} \frac{\Sigma_{\beta\gamma} \left(\mathbb{N}_{\text{true}}^{-1}\right)_{\alpha\beta} (\delta\mathbb{N})_{\beta\gamma} \left(\mathbb{N}_{\text{true}}^{-1}\right)_{\gamma\alpha}}{\left(\mathbb{N}_{\text{true}}^{-1}\right)_{\alpha\alpha}}\right]. \tag{D.4}$$

In order to rewrite Eq. (D.4), we use the definition of the inverse of a matrix in terms of its adjugate and determinant, $\mathbb{N}^{-1} = \text{adj}(\mathbb{N})/\det(\mathbb{N})$, and Eq. (D.1), which leads to

$$(c_\alpha^{\max})_{\text{num}} \simeq (c_\alpha^{\max})_{\text{true}} \left[1 - \frac{1}{2} \frac{\epsilon}{\det(\mathbb{N}_{\text{true}})} \frac{\Sigma_{\beta\gamma} \left(\mathbb{N}_{\text{true}}^{-1}\right)_{\alpha\beta} (\delta\mathbb{N})_{\beta\gamma} \left(\mathbb{N}_{\text{true}}^{-1}\right)_{\gamma\alpha}}{\left(\mathbb{N}_{\text{true}}^{-1}\right)_{\alpha\alpha}}\right]. \tag{D.5}$$

In most cases, the true and numerically obtained value for $c_\alpha^{\max}$ coincide very well, since then $\epsilon \ll 1$ controls the perturbation term and makes it negligible. In some cases, however, namely if $\det(\mathbb{N}_{\text{true}})$ is very small compared to the entries of $\mathbb{N}_{\text{true}}$ and $\text{adj}(\mathbb{N}_{\text{true}})$, the correction is not negligible anymore and for a few cases, the presented perturbative approach might fail completely. In the latter cases, we cannot trust our results for $c_\alpha^{\max}$, as the numerically obtained values can be quite different to the true ones. If the diagonal entries of $\mathbb{N}_{\text{true}}^{-1}$ contain negative numbers, the values are even imaginary. These problems occur for very hierarchical eigenvalues of $\mathbb{N}_{\text{true}}$, *i.e.* when the allowed parameter space is very elongated.

To give an example, we consider $\mathbb{N}$ to be a 2×2 matrix, which is the case when having only one operator at a time, but interference among the isoscalar and isovector (or proton and neutron) component. Here, Eq. (D.5) specifically reads

$$(c_\alpha^{\max})_{\text{num}} \simeq (c_\alpha^{\max})_{\text{true}} \left[1 - \frac{\epsilon}{2} \left(a_{\alpha\alpha} + (a_{11} + a_{22} - 2a_{12})\right) \frac{(\mathbb{N}_{\text{true}})_{12}^2}{\det\left(\mathbb{N}_{\text{true}}\right)}\right], \tag{D.6}$$

for $c_1 = c_i^n$ and $c_2 = c_i^p$. From this we find that the results can be trusted if

$$\epsilon \ll \left(\frac{(\mathbb{N}_{\text{true}})_{12}^2}{\det\left(\mathbb{N}_{\text{true}}\right)}\right)^{-1}, \tag{D.7}$$

which is more restrictive than $\epsilon \ll 1$.

To illustrate the influence of the error on the results, we calculated the PICO-60 upper limits for c_4^p and c_4^n, for different values of ϵ $\left(\mathcal{O}\left(10^{-5}\right), \mathcal{O}\left(10^{-4}\right), \mathcal{O}\left(10^{-3}\right) \text{ and } \mathcal{O}\left(10^{-2}\right)\right)$ and random values for a_{ij}. We show the results in Fig. D.1.

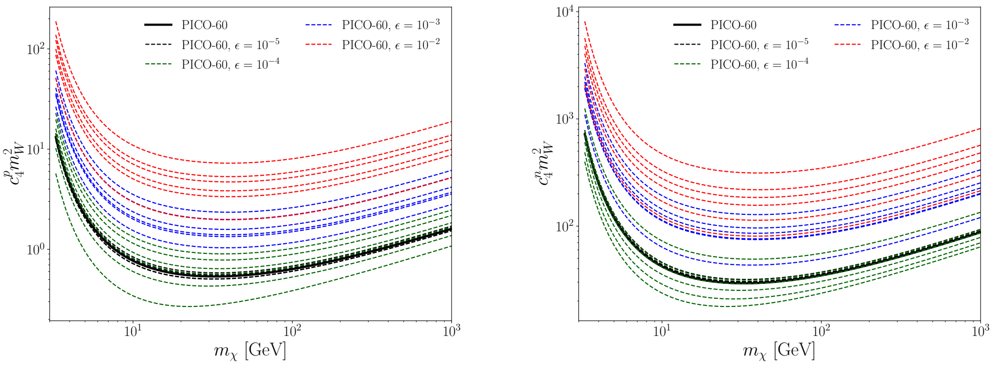

Figure D.1: PICO-60 upper limits on the dark matter-proton (neutron) coupling strength in the left (right) panel for operator $\mathcal{O}_4$ taking interference among the isoscalar and isovector component into account, with a relative error of the order $\epsilon = 10^{-5}$, 10^{-4}, 10^{-3} and 10^{-2} for random values of a_{ij}.

It turns out that if the numerical calculation precision of the elements in the matrix $\mathbb{N}_{\text{PICO}-60}$ is better than 1‰, the obtained limits differ from the true limit by a factor of the order 1. If it is worse than 1‰, the obtained limit can be different from the true limit by more than one order of magnitude.

E

Experiments

E.1 XENON1T

XENON is an underground experiment located at the Italian Gran Sasso National Laboratory with the goal to detect dark matter particles by their recoils off nuclei in the detector material consisting of liquid xenon [24]. XENON1T in particular is a follow-up phase of its predecessors XENON10 and XENON100.

The setup

The detector with a fiducial volume of ~ 2 tons consists of 3.2 tons of liquid (on the bottom) and gaseous (on top) xenon surrounded by a water tank that has the purpose to filter out muons [11]. The xenon is used by a dual phase time projection chamber. In both phases each, the gaseous and liquid one, an array of photomultiplier tubes is installed with the aim to detect scintillation and electroluminescence light produced by charged particles that interact in the detector. Further, an electric field sufficiently large and strong is created in the gaseous xenon phase in order to filter out the electrons from the liquid phase. If an incoming particle interacts with the detector material, it creates scintillation and ionization. The former is promptly detected by the photomultipliers which is denoted as S1 signal, whereas the electron is filtered out by the electric field, avoiding the recombination with the produced ion and enabling a strong enough acceleration of the electron such that it produces scintillation light which is also detected by the photomultipliers. This is denoted signal S2. Due to the uniform drift velocity of the electrons in liquid xenon, the measurement of the time delay between S1 and S1 and by checking the amount of photons seen by each photomultiplier, a 3D position determination is possible.

Dark matter searches

The release of the first results by XENON1T was in 2017 after collecting data for 34 days. Although the collaboration could not detect the WIMP, the release had a big impact as the resulting exclusion limits on the WIMP-nucleon cross-section exceeded the ones from the LUX experiment, which were considered the best limits before [24]. In 2018, the collaboration published limits after the collection of data for 278.8 days, setting a new record for the strongest limit on the spin-independent WIMP-nucleon cross-section [124]. In 2020, an excess of electron recoils in XENON1T was reported with a statistical significance of 3.5σ [156]. Several explanations for this excess have been discussed, such as the existence solar axions or axion-like particles [157, 158], an unexpected large magnetic moment for neutrinos [156], the impurity of the detector caused by tritium [159] or the existence of chameleons, which are dark energy particle candidates [160].

For this work, we use data that was released in 2018 with 7.36 expected background events and 14 observed events [24].

E.2 PICO60

Such as XENON1T, PICO-60 is searching for recoils off nuclei of unknown origin in an underground detector which would be direct evidence for the existence of dark matter. It is located at SNOLAB in Canada.

The setup

PICO-60 follows the principle of a bubble chamber detector. It makes use of small droplets of superheated liquid distributed in a gel matrix. If a traversing particle scatters of detector material and transfers energy to a droplet, this droplet goes through a phase transition and finally becomes a gas bubble. The parallely induced acoustic shock wave is detected by the piezo-electric sensors.

Dark matter searches

The first run of PICO-60 started in 2013 with an active volume of 25 liters, however, using only half of it. As detector material CF_3I has been used [25]. After the first run, the experiment was refurbished; the maximum capacity of the active volume was increased to 53 liters and the new choice of the detector material fell on C_3F_8. The second run started in 2016 and ended one year later [161]. The data was collected in two bins. For the first bin we take 1 expected background event and 3 observed events, for the second bin 0 expected background and observed events [161].

E.3 IceCube

The IceCube Neutrino Observatory is a neutrino telescope located close to the Amundsen-Scott South Pole Station in the ice of Antarctica.

The setup

Its size measures more than one cubic kilometer. IceCube is made of 5,160 spherical optical sensors, the so-called Digital Optical Modules (DOMs), each equipped with a photomultiplier tube and a single-board data acquisition computer which has the task to send the collected digital data to the surface. Using a hot water drill, 86 boreholes (often denoted as “strings”) were created in the ice, each filled with 60 DOMs. The horizontal separation of the DOMs is 125 meters, the vertical separation is 17 meters. It has a neutrino energy threshold of $\sim 100\,\mathrm{GeV}$. The sub-detector DeepCore at the center of this configuration is made of eight of these strings, which are arranged more compact compared to the rest: the horizontal spacing is only 70 meters and the vertical spacing is 7 meters. This causes a lowering of the threshold down to $\sim 10\,\mathrm{GeV}$.

On the surface of the ice 81 stations are located which carry the name IceTop. The equipment of each station consists of two DOMs pointing downwards. IceTop has the task to serve as a veto and calibration detector for IceCube.

Dark matter searches

Apart from searches for point sources of high-energy neutrinos, gamma-ray bursts coincident with neutrinos, neutrino oscillations, galactic supernovae and sterile neutrinos, another experimental goal is the indirect search of dark matter particles, for example by the analysis of solar neutrinos that might originate in dark matter annihilation processes. The neutrinos cannot be detected directly, however, they leave imprints, due to the production of electrically charged secondary particles when they interact with the ice surrounding the strings. In the ice these secondary particles travel faster than light leading to the emission of Cherenkov light, which is collected by the sensors. They additionally digitize the signal and provide a time stamp for each. After that, the information is sent to the surface, where it is converted from the DOMs into light patterns which sheds light on direction and energy of the neutrinos.

In this work, we use the 2016-data release, in which the Sun was the object of dark matter searches from May 2011 to May 2013. The data states that there were 926 (427) observed events for IceCube (DeepCore), while expecting 931 (414) background events [13].

Bibliography

[1] Anja Brenner, Alejandro Ibarra, and Andreas Rappelt. Conservative constraints on the effective theory of dark matter-nucleon interactions from icecube: the impact of operator interference. *Journal of Cosmology and Astroparticle Physics*, 2021(07):012, 2021.

[2] A Brenner, G Herrera, A Ibarra, S Kang, A Rappelt, S Scopel, and G Tomar. Impact of operator interference in dark matter direct detection experiments. 2021.

[3] Anja Brenner, Gonzalo Herrera, Alejandro Ibarra, Sunghyun Kang, Andreas Rappelt, Stefano Scopel, and Gaurav Tomar. The impact of operator interference and target complementarity in dark matter direct detection experiments. In *Journal of Physics: Conference Series*, volume 2156, page 012069. IOP Publishing, 2021.

[4] Anja Brenner, Gonzalo Herrera, Alejandro Ibarra, Sunghyun Kang, Stefano Scopel, and Gaurav Tomar. Complementarity of experiments in probing the non-relativistic effective theory of dark matter-nucleon interactions. *arXiv preprint arXiv:2203.04210*, 2022.

[5] Jan H Oort. The force exerted by the stellar system in the direction perpendicular to the galactic plane and some related problems. *Bulletin of the Astronomical Institutes of the Netherlands*, 6:249, 1932.

[6] Fritz Zwicky. On the masses of nebulae and of clusters of nebulae. *The Astrophysical Journal*, 86:217, 1937.

[7] Horace W Babcock. The rotation of the andromeda nebula. *Lick Observatory Bulletin*, 19:41–51, 1939.

[8] HC Van de Hulst, E Raimond, and H Van Woerden. Rotation and density distribution of the andromeda nebula derived from observations of the 21-cm line. *Bulletin of the Astronomical Institutes of the Netherlands*, 14:1, 1957.

[9] M Schmidt. The distribution of mass in m 31. *Bulletin of the Astronomical Institutes of the Netherlands*, 14:17, 1957.

[10] Richard Massey, Thomas Kitching, and Johan Richard. The dark matter of gravitational lensing. *Reports on Progress in Physics*, 73(8):086901, 2010.

[11] Elena Aprile, J Aalbers, F Agostini, M Alfonsi, FD Amaro, M Anthony, B Antunes, F Arneodo, M Balata, P Barrow, et al. The xenon1t dark matter experiment. *The European Physical Journal C*, 77(12):1–23, 2017.

[12] C Amole, M Ardid, David M Asner, D Baxter, E Behnke, P Bhattacharjee, H Borsodi, Manuel Bou-Cabo, SJ Brice, D Broemmelsiek, et al. Dark matter search results from the pico-60 cf 3 i bubble chamber. *Physical Review D*, 93(5):052014, 2016.

[13] MG Aartsen, M Ackermann, J Adams, JA Aguilar, M Ahlers, M Ahrens, D Altmann, K Andeen, T Anderson, I Ansseau, et al. Search for annihilating dark matter in the sun with 3 years of icecube data. *The European Physical Journal C*, 77(3):1–12, 2017.

[14] Jonathan L Feng, Jason Kumar, Danny Marfatia, and David Sanford. Isospin-violating dark matter. *Physics Letters B*, 703(2):124–127, 2011.

[15] Vincenzo Cirigliano, Michael L Graesser, and Grigory Ovanesyan. Wimp-nucleus scattering in chiral effective theory. *Journal of High Energy Physics*, 2012(10):1–22, 2012.

[16] Vincenzo Cirigliano, Michael L Graesser, Grigory Ovanesyan, and Ian M Shoemaker. Shining lux on isospin-violating dark matter beyond leading order. *Physics Letters B*, 739:293–301, 2014.

[17] Yu Gao, Jason Kumar, and Danny Marfatia. Isospin-violating dark matter in the sun. *Physics Letters B*, 704(5):534–540, 2011.

[18] Xin Gao, Zhaofeng Kang, and Tianjun Li. Origins of the isospin violation of dark matter interactions. *Journal of Cosmology and Astroparticle Physics*, 2013(01):021, 2013.

[19] Mads T Frandsen, Felix Kahlhoefer, Subir Sarkar, and Kai Schmidt-Hoberg. Direct detection of dark matter in models with a light z'. *Journal of High Energy Physics*, 2011(9):1–17, 2011.

[20] Koichi Hamaguchi, Seng Pei Liew, Takeo Moroi, and Yasuhiro Yamamoto. Isospin-violating dark matter with colored mediators. *Journal of High Energy Physics*, 2014(5):1–21, 2014.

[21] Genevieve Bélanger, Andreas Goudelis, Jong-Chul Park, and Alexander Pukhov. Isospin-violating dark matter from a double portal. *Journal of Cosmology and Astroparticle Physics*, 2014(02):020, 2014.

[22] Aleksandra Drozd, Bohdan Grzadkowski, John F Gunion, and Yun Jiang. Isospin-violating dark-matter-nucleon scattering via two-higgs-doublet-model portals. *Journal of Cosmology and Astroparticle Physics*, 2016(10):040, 2016.

[23] Víctor Martín Lozano, Miguel Peiró, and Pablo Soler. Isospin violating dark matter in stückelberg portal scenarios. *Journal of High Energy Physics*, 2015(4):1–29, 2015.

[24] Elena Aprile, J Aalbers, F Agostini, M Alfonsi, FD Amaro, M Anthony, F Arneodo, P Barrow, L Baudis, Boris Bauermeister, et al. First dark matter search results from the xenon1t experiment. *Physical review letters*, 119(18):181301, 2017.

[25] C Amole, M Ardid, David M Asner, D Baxter, E Behnke, P Bhattacharjee, H Borsodi, Manuel Bou-Cabo, SJ Brice, D Broemmelsiek, et al. Dark matter search results from the pico-60 cf 3 i bubble chamber. *Physical Review D*, 93(5):052014, 2016.

[26] Chanpreet Amole, M Ardid, IJ Arnquist, DM Asner, D Baxter, E Behnke, M Bressler, B Broerman, G Cao, CJ Chen, et al. Dark matter search results from the complete exposure of the pico-60 c 3 f 8 bubble chamber. *Physical Review D*, 100(2):022001, 2019.

[27] Paolo Salucci, Fabrizio Nesti, Gianfranco Gentile, and C Frigerio Martins. The dark matter density at the sun's location. *Astronomy & Astrophysics*, 523:A83, 2010.

[28] Riccardo Catena and Piero Ullio. A novel determination of the local dark matter density. *Journal of Cosmology and Astroparticle Physics*, 2010(08):004, 2010.

[29] Markus Weber and Wim de Boer. Determination of the local dark matter density in our galaxy. *Astronomy & Astrophysics*, 509:A25, 2010.

[30] Fabio Iocco, Miguel Pato, Gianfranco Bertone, and Philippe Jetzer. Dark matter distribution in the milky way: microlensing and dynamical constraints. *Journal of Cosmology and Astroparticle Physics*, 2011(11):029, 2011.

[31] Paul J McMillan. Mass models of the milky way. *Monthly Notices of the Royal Astronomical Society*, 414(3):2446–2457, 2011.

[32] Miguel Pato, Fabio Iocco, and Gianfranco Bertone. Dynamical constraints on the dark matter distribution in the milky way. *Journal of Cosmology and Astroparticle Physics*, 2015(12):001, 2015.

[33] Yang Huang, X-W Liu, H-B Yuan, M-S Xiang, H-W Zhang, B-Q Chen, J-J Ren, Chun Wang, Yong Zhang, Y-H Hou, et al. The milky way's rotation curve out to 100 kpc and its constraint on the galactic mass distribution. *Monthly Notices of the Royal Astronomical Society*, 463(3):2623–2639, 2016.

[34] Paul J McMillan. The mass distribution and gravitational potential of the milky way. *Monthly Notices of the Royal Astronomical Society*, page stw2759, 2016.

[35] C Moni Bidin, Giovanni Carraro, RA Méndez, and R Smith. Kinematical and chemical vertical structure of the galactic thick disk. ii. a lack of dark matter in the solar neighborhood. *The Astrophysical Journal*, 751(1):30, 2012.

[36] Jo Bovy and Scott Tremaine. On the local dark matter density. *The Astrophysical Journal*, 756(1):89, 2012.

[37] Silvia Garbari, Chao Liu, Justin I Read, and George Lake. A new determination of the local dark matter density from the kinematics of k dwarfs. *Monthly Notices of the Royal Astronomical Society*, 425(2):1445–1458, 2012.

[38] Martin C Smith, S Hannah Whiteoak, and NW Evans. Slicing and dicing the milky way disk in the sloan digital sky survey. *The Astrophysical Journal*, 746(2):181, 2012.

[39] Lan Zhang, Hans-Walter Rix, Glenn van de Ven, Jo Bovy, Chao Liu, and Gang Zhao. The gravitational potential near the sun from segue k-dwarf kinematics. *The Astrophysical Journal*, 772(2):108, 2013.

[40] Olivier Bienayme, Benoit Famaey, Arnaud Siebert, Ken C Freeman, Brad K Gibson, G Gilmore, Eva K Grebel, Joss Bland-Hawthorn, Georges Kordopatis, Ulisse Munari, et al. Weighing the local dark matter with rave red clump stars. *Astronomy & Astrophysics*, 571:A92, 2014.

[41] Christopher F McKee, Antonio Parravano, and David J Hollenbach. Stars, gas, and dark matter in the solar neighborhood. *The Astrophysical Journal*, 814(1):13, 2015.

[42] Qiran Xia, Chao Liu, Shude Mao, Yingyi Song, Lan Zhang, RJ Long, Yong Zhang, Yonghui Hou, Yuefei Wang, and Yue Wu. Determining the local dark matter density with lamost data. *Monthly Notices of the Royal Astronomical Society*, 458(4):3839–3850, 2016.

[43] Sofia Sivertsson, Hamish Silverwood, Justin I Read, Gianfranco Bertone, and Pascal Steger. The localdark matter density from sdss-segue g-dwarfs. *Monthly Notices of the Royal Astronomical Society*, 478(2):1677–1693, 2018.

[44] Pijushpani Bhattacharjee, Soumini Chaudhury, Susmita Kundu, and Subhabrata Majumdar. Deriving the velocity distribution of galactic dark matter particles from the rotation curve data. *Physical Review D*, 87(8):083525, 2013.

[45] Mattia Fornasa and Anne M Green. Self-consistent phase-space distribution function for the anisotropic dark matter halo of the milky way. *Physical Review D*, 89(6):063531, 2014.

[46] Nassim Bozorgnia, Riccardo Catena, and Thomas Schwetz. Anisotropic dark matter distribution functions and impact on wimp direct detection. *Journal of Cosmology and Astroparticle Physics*, 2013(12):050, 2013.

[47] Sayan Mandal, Subhabrata Majumdar, Vikram Rentala, and Ritoban Basu Thakur. Observationally inferred dark matter phase-space distribution and direct detection experiments. *Physical Review D*, 100(2):023002, 2019.

[48] KG Begeman, AH Broeils, and RH Sanders. Extended rotation curves of spiral galaxies: Dark haloes and modified dynamics. *Monthly Notices of the Royal Astronomical Society*, 249(3):523–537, 1991.

[49] John Daintith, Derek Gjertsen, John Clark, Elzabeth Martin, Anne Stibbs, Fran Alexander, Johnathan Law, Peter Lewis, Mark Salad, Elizabeth Tootil, et al. Oxford dictionary of scientists. *Oxford Dictionary of Scientists*, 1999.

[50] LMJS Volders. Neutral hydrogen in m 33 and m 101. *Bulletin of the Astronomical Institutes of the Netherlands*, 14:323, 1959.

[51] Vera C Rubin and W Kent Ford Jr. Rotation of the andromeda nebula from a spectroscopic survey of emission regions. *The Astrophysical Journal*, 159:379, 1970.

[52] Vera C Rubin, W Kent Ford Jr, and Norbert Thonnard. Extended rotation curves of high-luminosity spiral galaxies. iv-systematic dynamical properties, sa through sc. *The Astrophysical Journal*, 225:L107–L111, 1978.

[53] Vera C Rubin. Dark matter in spiral galaxies. *Scientific American*, 248(6):96–109, 1983.

[54] Giuseppina Battaglia, Amina Helmi, Heather Morrison, Paul Harding, Edward W Olszewski, Mario Mateo, Kenneth C Freeman, John Norris, and Stephen A Shectman. The radial velocity dispersion profile

of the galactic halo: constraining the density profile of the dark halo of the milky way. *Monthly Notices of the Royal Astronomical Society*, 364(2):433–442, 2005.

[55] Prajwal Raj Kafle, Sanjib Sharma, Geraint F Lewis, and Joss Bland-Hawthorn. On the shoulders of giants: properties of the stellar halo and the milky way mass distribution. *The Astrophysical Journal*, 794(1):59, 2014.

[56] Maxim Markevitch, AH Gonzalez, D Clowe, A Vikhlinin, L David, W Forman, C Jones, S Murray, and W Tucker. Direct constraints on the dark matter self - interaction cross - section from the merging cluster 1e0657-56. *Arxiv preprint astro-ph/0309303*.

[57] Douglas Clowe, Maruša Bradač, Anthony H Gonzalez, Maxim Markevitch, Scott W Randall, Christine Jones, and Dennis Zaritsky. A direct empirical proof of the existence of dark matter. *The Astrophysical Journal*, 648(2):L109, 2006.

[58] Chandra X ray Observatory. 1e 0657-56 with scale bar.

[59] CL Bennett, RS Hill, G Hinshaw, D Larson, KM Smith, J Dunkley, B Gold, M Halpern, N Jarosik, A Kogut, et al. Seven-year wilkinson microwave anisotropy probe (wmap*) observations: Are there cosmic microwave background anomalies? *The Astrophysical journal supplement series*, 192(2):17, 2011.

[60] Peter AR Ade, N Aghanim, M Arnaud, Mark Ashdown, J Aumont, C Baccigalupi, AJ Banday, RB Barreiro, JG Bartlett, N Bartolo, et al. Planck 2015 results-xiii. cosmological parameters. *Astronomy & Astrophysics*, 594:A13, 2016.

[61] Arno A Penzias and Robert Woodrow Wilson. A measurement of excess antenna temperature at 4080 mc/s. *The Astrophysical Journal*, 142:419–421, 1965.

[62] Robert H Dicke, P James E Peebles, Peter G Roll, and David T Wilkinson. Cosmic black-body radiation. *The Astrophysical Journal*, 142:414–419, 1965.

[63] George F Smoot, Charles L Bennett, A Kogut, EL Wright, J Aymon, NW Boggess, ES Cheng, G De Amici, S Gulkis, MG Hauser, et al. Structure in the cobe differential microwave radiometer first-year maps. *The Astrophysical Journal*, 396:L1–L5, 1992.

[64] Rainer K Sachs and Arthur M Wolfe. Perturbations of a cosmological model and angular variations of the microwave background. *The Astrophysical Journal*, 147:73, 1967.

[65] Edward L Wright, Stephan S Meyer, Charles L Bennett, Nancy W Boggess, ES Cheng, Michael G Hauser, A Kogut, C Lineweaver, John C Mather, George F Smoot, et al. Interpretation of the cosmic microwave background radiation anisotropy detected by the cobe differential microwave radiometer. *The Astrophysical Journal*, 396:L13–L18, 1992.

[66] Department of Astronomy and Astrophysics at the University of Chicago. Radiation pressure and gravity.

[67] Max Tegmark, Angelica de Oliveira-Costa, and Andrew JS Hamilton. High resolution foreground cleaned cmb map from wmap. *Physical Review D*, 68(12):123523, 2003.

[68] GE Addison, Y Huang, DJ Watts, CL Bennett, M Halpern, G Hinshaw, and JL Weiland. Quantifying discordance in the 2015 planck cmb spectrum. *The Astrophysical Journal*, 818(2):132, 2016.

[69] Dominik J Schwarz, Craig J Copi, Dragan Huterer, and Glenn D Starkman. Cmb anomalies after planck. *Classical and Quantum Gravity*, 33(18):184001, 2016.

[70] ESA and the Planck Collaboration. Planck cmb.

[71] Eiichiro Komatsu, J Dunkley, MR Nolta, CL Bennett, B Gold, G Hinshaw, N Jarosik, D Larson, M Limon, L Page, et al. Five-year wilkinson microwave anisotropy probe* observations: cosmological interpretation. *The Astrophysical Journal Supplement Series*, 180(2):330, 2009.

[72] Katherine Freese. Status of dark matter in the universe. In *The Fourteenth Marcel Grossmann Meeting On Recent Developments in Theoretical and Experimental General Relativity, Astrophysics, and Relativistic*

Field Theories: Proceedings of the MG14 Meeting on General Relativity, University of Rome "La Sapienza", Italy, 12–18 July 2015, pages 325–355. World Scientific, 2018.

[73] Nabila Aghanim, Yashar Akrami, Mark Ashdown, J Aumont, C Baccigalupi, M Ballardini, AJ Banday, RB Barreiro, N Bartolo, S Basak, et al. Planck 2018 results-vi. cosmological parameters. *Astronomy & Astrophysics*, 641:A6, 2020.

[74] Kris Sigurdson, Michael Doran, Andriy Kurylov, Robert R Caldwell, and Marc Kamionkowski. Dark-matter electric and magnetic dipole moments. *Physical Review D*, 70(8):083501, 2004.

[75] JL Basdevant, R Mochkovitch, J Rich, Michel Spiro, and A Vidal-Madjar. Is there room for changed dark matter? *Physics Letters B*, 234(3):395–398, 1990.

[76] Andrea Caputo, Laura Sberna, Miguel Frias, Diego Blas, Paolo Pani, Lijing Shao, and Wenming Yan. Constraints on millicharged dark matter and axionlike particles from timing of radio waves. *Physical Review D*, 100(6):063515, 2019.

[77] Amin Aboubrahim, Pran Nath, and Zhu-Yao Wang. A cosmologically consistent millicharged dark matter solution to the edges anomaly of possible string theory origin. *Journal of High Energy Physics*, 2021(12):1–30, 2021.

[78] David Harvey, Richard Massey, Thomas Kitching, Andy Taylor, and Eric Tittley. The nongravitational interactions of dark matter in colliding galaxy clusters. *Science*, 347(6229):1462–1465, 2015.

[79] Scott W Randall, Maxim Markevitch, Douglas Clowe, Anthony H Gonzalez, and Marusa Bradač. Constraints on the self-interaction cross section of dark matter from numerical simulations of the merging galaxy cluster 1e 0657–56. *The Astrophysical Journal*, 679(2):1173, 2008.

[80] PJE Peebles. Large scale background temperature and mass fluctuations due to scale invariant primeval perturbations, 1982.

[81] J Richard Bond, Alexander S Szalay, and Michael S Turner. Formation of galaxies in a gravitino-dominated universe. *Physical Review Letters*, 48(23):1636, 1982.

[82] George R Blumenthal, Heinz Pagels, and Joel R Primack. Galaxy formation by dissipationless particles heavier than neutrinos. *Nature*, 299(5878):37–38, 1982.

[83] George R Blumenthal, SM Faber, Joel R Primack, and Martin J Rees. Formation of galaxies and large-scale structure with cold dark matter. *nature*, 311(5986):517–525, 1984.

[84] Marc Davis, George Efstathiou, Carlos S Frenk, and Simon DM White. The evolution of large-scale structure in a universe dominated by cold dark matter. *The Astrophysical Journal*, 292:371–394, 1985.

[85] Beth A Reid, Will J Percival, Daniel J Eisenstein, Licia Verde, David N Spergel, Ramin A Skibba, Neta A Bahcall, Tamas Budavari, Joshua A Frieman, Masataka Fukugita, et al. Cosmological constraints from the clustering of the sloan digital sky survey dr7 luminous red galaxies. *Monthly Notices of the Royal Astronomical Society*, 404(1):60–85, 2010.

[86] Gary Steigman and Michael S Turner. Cosmological constraints on the properties of weakly interacting massive particles. *Nuclear Physics B*, 253:375–386, 1985.

[87] Leszek Roszkowski, Enrico Maria Sessolo, and Sebastian Trojanowski. Wimp dark matter candidates and searches—current status and future prospects. *Reports on Progress in Physics*, 81(6):066201, 2018.

[88] Edward W Kolb and Michael S Turner. *The early universe*. CRC press, 2018.

[89] Gary Steigman, Basudeb Dasgupta, and John F Beacom. Precise relic wimp abundance and its impact on searches for dark matter annihilation. *Physical Review D*, 86(2):023506, 2012.

[90] Stephen P Martin. A supersymmetry primer. In *Perspectives on supersymmetry II*, pages 1–153. World Scientific, 2010.

[91] Howard E Haber and Laurel Stephenson Haskins. Supersymmetric theory and models. In *Anticipating the Next Discoveries in Particle Physics: TASI 2016 Proceedings of 2016 Theoretical Advanced Study Institute in Elementary Particle Physics*, pages 355–499. World Scientific, 2018.

[92] Geraldine Servant and Tim MP Tait. Is the lightest kaluza–klein particle a viable dark matter candidate? *Nuclear Physics B*, 650(1-2):391–419, 2003.

[93] JD Lewin and PF Smith. Review of mathematics, numerical factors, and corrections for dark matter experiments based on elastic nuclear recoil. *Astroparticle Physics*, 6(1):87–112, 1996.

[94] Til Piffl, Cecilia Scannapieco, James Binney, Matthias Steinmetz, R-D Scholz, Mary EK Williams, Roelof S De Jong, Georges Kordopatis, Gal Matijevič, Olivier Bienayme, et al. The rave survey: the galactic escape speed and the mass of the milky way. *Astronomy & Astrophysics*, 562:A91, 2014.

[95] Martin C Smith, Gregory R Ruchti, Amina Helmi, Rosemary FG Wyse, Jon P Fulbright, Kenneth C Freeman, Julio F Navarro, George M Seabroke, Matthias Steinmetz, Mary Williams, et al. The rave survey: constraining the local galactic escape speed. *Monthly Notices of the Royal Astronomical Society*, 379(2):755–772, 2007.

[96] XX Xue, HW Rix, G Zhao, P Re Fiorentin, T Naab, M Steinmetz, FC Van den Bosch, TC Beers, YS Lee, EF Bell, et al. The milky way's circular velocity curve to 60 kpc and an estimate of the dark matter halo mass from the kinematics of˜ 2400 sdss blue horizontal-branch stars. *The Astrophysical Journal*, 684(2):1143, 2008.

[97] Paul J McMillan and James J Binney. The uncertainty in galactic parameters. *Monthly Notices of the Royal Astronomical Society*, 402(2):934–940, 2010.

[98] Jo Bovy, David W Hogg, and Hans-Walter Rix. Galactic masers and the milky way circular velocity. *The Astrophysical Journal*, 704(2):1704, 2009.

[99] Anne M Green. Astrophysical uncertainties on direct detection experiments. *Modern Physics Letters A*, 27(03):1230004, 2012.

[100] Frank J Kerr and Donald Lynden-Bell. Review of galactic constants. *Monthly Notices of the Royal Astronomical Society*, 221(4):1023–1038, 1986.

[101] A Archer, M Cahill-Rowley, R Cotta, S Digel, A Drlica-Wagner, F Ferrer, S Funk, J Hewett, J Holder, B Humensky, et al. Indirect dark matter detection cf2 working group summary. *arXiv preprint arXiv:1310.7040*, 2013.

[102] Lisa Goodenough and Dan Hooper. Possible evidence for dark matter annihilation in the inner milky way from the fermi gamma ray space telescope. *arXiv preprint arXiv:0910.2998*, 2009.

[103] Aldo Morselli. Constraints on wimp annihilation for contracted dark matter in the inner galaxy with gamma-rays. *Science with the New Generation of High Energy Gamma-ray Experiments*, page 28, 2015.

[104] RL Golden, S Horan, BG Mauger, GD Badhwar, JL Lacy, SA Stephens, RR Daniel, and JE Zipse. Evidence for the existence of cosmic-ray antiprotons. *Physical Review Letters*, 43(16):1196, 1979.

[105] Collaboration Ams, AMS Collaboration, et al. Antiproton flux, antiproton-to-proton flux ratio, and properties of elementary particle fluxes in primary cosmic rays measured with the alpha magnetic spectrometer on the international space station. *Physical review letters*, 117(9):091103–091103, 2016.

[106] Joseph Silk and Mark Srednicki. Cosmic-ray antiprotons as a probe of a photino-dominated universe. *Physical Review Letters*, 53(6):624, 1984.

[107] Fiorenza Donato, Nicolao Fornengo, and Pierre Salati. Antideuterons as a signature of supersymmetric dark matter. *Physical Review D*, 62(4):043003, 2000.

[108] M Ajello, WB Atwood, Magnus Axelsson, R Bagagli, M Bagni, L Baldini, D Bastieri, F Bellardi, R Bellazzini, E Bissaldi, et al. Fermi large area

telescope performance after 10 years of operation. *The Astrophysical Journal Supplement Series*, 256(1):12, 2021.

[109] Rolf Kappl and Martin Wolfgang Winkler. The cosmic ray antiproton background for ams-02. *Journal of Cosmology and Astroparticle Physics*, 2014(09):051, 2014.

[110] Julio F Navarro, Carlos S Frenk, and Simon DM White. A universal density profile from hierarchical clustering. *The Astrophysical Journal*, 490(2):493, 1997.

[111] Julio F Navarro, Eric Hayashi, Chris Power, AR Jenkins, Carlos S Frenk, Simon DM White, Volker Springel, Joachim Stadel, and Thomas R Quinn. The inner structure of λcdm haloes–iii. universality and asymptotic slopes. *Monthly Notices of the Royal Astronomical Society*, 349(3):1039–1051, 2004.

[112] Francesc Ferrer and Daniel R Hunter. The impact of the phase-space density on the indirect detection of dark matter. *Journal of Cosmology and Astroparticle Physics*, 2013(09):005, 2013.

[113] Andreas Burkert. The structure of dark matter halos in dwarf galaxies. *The Astrophysical Journal*, 447(1):L25, 1995.

[114] Matthew G Walker and Jorge Penarrubia. A method for measuring (slopes of) the mass profiles of dwarf spheroidal galaxies. *The Astrophysical Journal*, 742(1):20, 2011.

[115] NC Amorisco, A Agnello, and NW Evans. The core size of the fornax dwarf spheroidal. *Monthly Notices of the Royal Astronomical Society: Letters*, 429(1):L89–L93, 2013.

[116] R Abbasi, M Ackermann, J Adams, JA Aguilar, M Ahlers, M Ahrens, C Alispach, AA Alves Jr, NM Amin, R An, et al. The icecube collaboration–contributions to the 37th international cosmic ray conference (icrc2021). *arXiv preprint arXiv:2107.06966*, 2021.

[117] Andrew Gould. Weakly interacting massive particle distribution in and evaporation from the sun. *The Astrophysical Journal*, 321:560–570, 1987.

[118] Giorgio Busoni, Andrea De Simone, and Wei-Chih Huang. On the minimum dark matter mass testable by neutrinos from the sun. *Journal of Cosmology and Astroparticle Physics*, 2013(07):010, 2013.

[119] Zheng-Liang Liang, Yue-Liang Wu, Zi-Qing Yang, and Yu-Feng Zhou. On the evaporation of solar dark matter: spin-independent effective operators. *Journal of Cosmology and Astroparticle Physics*, 2016(09):018, 2016.

[120] Raghuveer Garani and Sergio Palomares-Ruiz. Dark matter in the sun: scattering off electrons vs nucleons. *Journal of Cosmology and Astroparticle Physics*, 2017(05):007, 2017.

[121] Giorgio Busoni, Andrea De Simone, Pat Scott, and Aaron C Vincent. Evaporation and scattering of momentum-and velocity-dependent dark matter in the sun. *Journal of Cosmology and Astroparticle Physics*, 2017(10):037, 2017.

[122] Kim Griest and David Seckel. Cosmic asymmetry, neutrinos and the sun. *Nuclear Physics B*, 283:681–705, 1987.

[123] Gerard Jungman, Marc Kamionkowski, and Kim Griest. Supersymmetric dark matter. *Physics Reports*, 267(5-6):195–373, 1996.

[124] XENON Collaboration, E Aprile, J Aalbers, F Agostini, M Alfonsi, L Althueser, FD Amaro, M Anthony, F Arneodo, L Baudis, et al. Dark matter search results from a one ton-year exposure of xenon1t. *Physical Review Letters*, 121(11):111302, 2018.

[125] Andrew Gould. Resonant enhancements in weakly interacting massive particle capture by the earth. *The Astrophysical Journal*, 321:571–585, 1987.

[126] William H Press and David N Spergel. Capture by the sun of a galactic population of weakly interacting, massive particles. *The Astrophysical Journal*, 296:679–684, 1985.

[127] Joseph Silk, Keith Olive, and Mark Srednicki. The photino, the sun, and high-energy neutrinos. *Physical Review Letters*, 55(2):257, 1985.

[128] TK Gaisser, Gary Steigman, and S Tilav. Limits on cold-dark-matter candidates from deep underground detectors. *Physical Review D*, 34(8):2206, 1986.

[129] Mark Srednicki, Keith A Olive, and Joseph Silk. High-energy neutrinos from the sun and cold dark matter. *Nuclear Physics B*, 279(3-4):804–823, 1987.

[130] Andrew Gould. Cosmological density of wimps from solar and terrestrial annihilations. *The Astrophysical Journal*, 388:338–344, 1992.

[131] Lyndon Evans and Philip Bryant. Lhc machine. *Journal of instrumentation*, 3(08):S08001, 2008.

[132] Pran Nath, Brent Nelson, Hooman Davoudiasl, Bhaskar Dutta, Daniel Feldman, Zuowei Liu, Tao Han, Paul Langacker, Rabi Mohapatra, Jose Valle, et al. The hunt for new physics at the large hadron collider. *Nuclear Physics B-Proceedings Supplements*, 200:185–417, 2010.

[133] Georges Aad, E Abat, J Abdallah, AA Abdelalim, Abdelmalek Abdesselam, BA Abi, M Abolins, H Abramowicz, E Acerbi, BS Acharya, et al. The atlas experiment at the cern large hadron collider. *Journal of instrumentation*, 3(S08003), 2008.

[134] Roman Adolphi et al. The cms experiment at the cern lhc. *Jinst*, 803:S08004, 2008.

[135] A Augusto Alves Jr, LM Andrade Filho, AF Barbosa, I Bediaga, G Cernicchiaro, G Guerrer, HP Lima Jr, AA Machado, J Magnin, F Marujo, et al. The lhcb detector at the lhc. *Journal of instrumentation*, 3(08):S08005, 2008.

[136] Herbi Dreiner, Daniel Schmeier, and Jamie Tattersall. Contact interactions probe effective dark-matter models at the lhc. *EPL (Europhysics Letters)*, 102(5):51001, 2013.

[137] Martin Hoferichter, Philipp Klos, Javier Menéndez, and Achim Schwenk. Improved limits for higgs-portal dark matter from lhc searches. *Physical Review Letters*, 119(18):181803, 2017.

[138] Otilia Ducu, Lucien Heurtier, and Julien Maurer. Lhc signatures of a z' mediator between dark matter and the su (3) sector. *Journal of High Energy Physics*, 2016(3):1–17, 2016.

[139] Howard Baer, Vernon Barger, Dibyashree Sengupta, Shadman Salam, and Kuver Sinha. Status of weak scale supersymmetry after lhc run 2 and ton-scale noble liquid wimp searches. *The European Physical Journal Special Topics*, 229(21):3085–3141, 2020.

[140] Nicolò Trevisani. Collider searches for dark matter (atlas+ cms). *Universe*, 4(11):131, 2018.

[141] JiJi Fan, Matthew Reece, and Lian-Tao Wang. Non-relativistic effective theory of dark matter direct detection. *Journal of Cosmology and Astroparticle Physics*, 2010(11):042, 2010.

[142] A Liam Fitzpatrick, Wick Haxton, Emanuel Katz, Nicholas Lubbers, and Yiming Xu. The effective field theory of dark matter direct detection. *Journal of Cosmology and Astroparticle Physics*, 2013(02):004, 2013.

[143] Nikhil Anand, A Liam Fitzpatrick, and WC Haxton. Model-independent wimp scattering responses and event rates: A mathematica package for experimental analysis. *arXiv preprint arXiv:1308.6288*, 2013.

[144] Riccardo Catena and Bodo Schwabe. Form factors for dark matter capture by the sun in effective theories. *Journal of Cosmology and Astroparticle Physics*, 2015(04):042, 2015.

[145] Riccardo Catena, Alejandro Ibarra, and Sebastian Wild. Dama confronts null searches in the effective theory of dark matter-nucleon interactions. *Journal of Cosmology and Astroparticle Physics*, 2016(05):039, 2016.

[146] Riccardo Catena, Alejandro Ibarra, Andreas Rappelt, and Sebastian Wild. Halo-independent comparison of direct detection experiments in the effective theory of dark matter-nucleon interactions. *Journal of Cosmology and Astroparticle Physics*, 2018(07):028, 2018.

[147] Marco Cirelli, Eugenio Del Nobile, and Paolo Panci. Tools for model-independent bounds in direct dark matter searches. *Journal of Cosmology and Astroparticle Physics*, 2013(10):019, 2013.

[148] Kingman Cheung, Yue-Lin S Tsai, Po-Yan Tseng, Tzu-Chiang Yuan, and A Zee. Global study of the simplest scalar phantom dark matter model. *Journal of Cosmology and Astroparticle Physics*, 2012(10):042, 2012.

[149] Zuowei Liu, Yushan Su, Yue-Lin Sming Tsai, Bingrong Yu, and Qiang Yuan. A combined analysis of pandax, lux, and xenon1t experiments within the framework of dark matter effective theory. *Journal of High Energy Physics*, 2017(11):1–28, 2017.

[150] Francesc Ferrer, Alejandro Ibarra, and Sebastian Wild. A novel approach to derive halo-independent limits on dark matter properties. *Journal of Cosmology and Astroparticle Physics*, 2015(09):052, 2015.

[151] Koun Choi, Carsten Rott, and Yoshitaka Itow. Impact of the dark matter velocity distribution on capture rates in the sun. *Journal of Cosmology and Astroparticle Physics*, 2014(05):049, 2014.

[152] Matthias Danninger and Carsten Rott. Solar wimps unravelled: Experiments, astrophysical uncertainties, and interactive tools. *Physics of the Dark Universe*, 5:35–44, 2014.

[153] Alejandro Ibarra, Bradley J Kavanagh, and Andreas Rappelt. Bracketing the impact of astrophysical uncertainties on local dark matter searches. *Journal of Cosmology and Astroparticle Physics*, 2018(12):018, 2018.

[154] Samuel S Wilks. The large-sample distribution of the likelihood ratio for testing composite hypotheses. *The annals of mathematical statistics*, 9(1):60–62, 1938.

[155] Aldo M Serenelli, Sarbani Basu, Jason W Ferguson, and Martin Asplund. New solar composition: the problem with solar models revisited. *The Astrophysical Journal Letters*, 705(2):L123, 2009.

[156] Elena Aprile, Jelle Aalbers, Fa Agostini, M Alfonsi, L Althueser, FD Amaro, Vasile C Antochi, E Angelino, JR Angevaare, F Arneodo, et al. Excess electronic recoil events in xenon1t. *Physical Review D*, 102(7):072004, 2020.

[157] Christina Gao, Jia Liu, Lian-Tao Wang, Xiao-Ping Wang, Wei Xue, and Yi-Ming Zhong. Reexamining the solar axion explanation for the xenon1t excess. *Physical Review Letters*, 125(13):131806, 2020.

[158] Peter Athron, Csaba Balázs, Ankit Beniwal, J Eliel Camargo-Molina, Andrew Fowlie, Tomás E Gonzalo, Sebastian Hoof, Felix Kahlhoefer, David JE Marsh, Markus Tobias Prim, et al. Global fits of axion-like particles to xenon1t and astrophysical data. *Journal of High Energy Physics*, 2021(5):1–40, 2021.

[159] Alan E Robinson. Xenon1t observes tritium. *arXiv preprint arXiv:2006.13278*, 2020.

[160] Sunny Vagnozzi, Luca Visinelli, Philippe Brax, Anne-Christine Davis, and Jeremy Sakstein. Direct detection of dark energy: The xenon1t excess and future prospects. *Physical Review D*, 104(6):063023, 2021.

[161] PICO collaboration et al. Dark matter search results from the pico-60 c3 f8 bubble chamber. *Physical review letters*, 118(25):251301, 2017.